3D PRINTED BLOOD VESSELS FOR TRANSLATIONAL MEDICINE

A Dissertation

by

KARLI AYN GOLD

Submitted to the Office of Graduate and Professional Studies of
Texas A&M University
in partial fulfillment of the requirements for the degree of

DOCTOR OF PHILOSOPHY

Chair of Committee,	Akhilesh K. Gaharwar
Co-Chair of Committee,	Abhishek Jain
Committee Members,	Melissa Grunlan
	Cynthia J. Meininger
Head of Department,	Michael J. McShane

May 2020

Major Subject: Biomedical Engineering

ABSTRACT

Vascular diseases, such as atherosclerosis and thrombosis, are the leading cause of morbidity and mortality worldwide. Despite major advancements to develop therapeutic interventions, the pathophysiology as it applies to humans is largely unclear and treatments limited. Thus, there is a critical need to increase our understanding of vascular physiology and assess emerging interventions in order to accelerate therapeutic development. Here, we designed a three-dimensional (3D) bioprinted vascular tissue platform that recapitulates both the multicellular constituents and tissue architecture innate to human vessels. Specifically, we introduced a new class of nanoengineered, hydrogel-based bioinks to fabricate anatomically accurate (10 mm diameter, 1 cm long), multicellular vessels with high printability, structural stability, and cytocompatibility. This approach permits for long-term co-culture of vascular smooth muscle cells (VSMCs) and endothelial cells (ECs), providing the opportunity to model vessel function and pathophysiology. To validate the ability of this platform to accurately reflect and model the onset of vascular thromboinflammation, 3D printed vessels were treated with the cytokine tumor necrosis factor-α (TNF-α), disrupting vascular EC barrier function. In the presence of a confluent lumen without TNF-α stimulation, no clotting was observed upon blood perfusion. However in cytokine-treated vessels, a dose-dependent response in clotting formation was observed. Furthermore, a significantly altered clotting phenomena was observed in EC-VSMC co-cultures relative to independent cell culture, suggesting

cellular cross-talk and communication within the 3D printed model. Overall, these studies demonstrate the ability of 3D bioprinted vessels to recapitulate human *in vivo* pathophysiology, thus illustrating the essential coupling between biology, engineering, and material science, impacting preclinical research studies.

ACKNOWLEDGEMENTS

I would like to thank my dissertation advisors, Dr. Akhilesh Gaharwar and Dr. Abhishek Jain. It has been an extremely valuable experience to be co-advised by both of you and I am forever grateful for the researcher you shaped me into today. Additionally, I would like to thank my committee members: Dr. Melissa Grunlan and Dr. Cynthia Meininger, for evaluating my research and methodologies as well as supporting me throughout the course of this research.

Additionally, I would like to thank my lab members, colleagues, as well as the department faculty and staff for making my time at Texas A&M a memorable experience. I would not have been able to complete this research without their indispensable support, help, and encouragement throughout this process.

Furthermore, thank you to Dr. Cosgriff-Hernandez and her lab, particularly Dr. Nick Sears, Dr. Stacy Cereceres, Dr. Michael Whitely, Taneidra Walker Buie, and Prachi Dhavalikar. I am so thankful for their mentorship and training during my first year in the Texas A&M biomedical engineering program.

Finally, I would like to extend a special form of gratitude to my family, specifically my parents, siblings, and future fiancé for their continuous encouragement, patience, and love

throughout this process. Since the very beginning, my family has always pushed me to thrive at whatever I put my mind to and supported me in any goal I set for myself. Without their love, support, and continuous encouragement I would not have been on the path of success.

CONTRIBUTORS AND FUNDING SOURCES

This work was supervised by a dissertation committee consisting of Professors Akhilesh K. Gaharwar (co-advisor), Abhishek Jain (co-advisor), Melissa Grunlan of the Department of Biomedical Engineering and Cynthia Meininger of the Department of Medical Physiology.

The data analysis for Chapter 2 was conducted in part by Navaneeth K.R. Pandian, of Dr. Jain's Laboratory, providing ANSYS modeling of the bioink within the printing extruder. Dr. Jorge Palma, of Dr. Javier Jo's Laboratory in the Department of Biomedical Engineering, aided us when conducting optical coherence tomography (OCT) of clotted constructs. Additionally, confocal imaging was conducted under the guidance of Dr. Roula Mouneimne of the Imaging Analysis Laboratory within Texas A&M's Veterinary Medicine and Biomedical Sciences program. Furthermore, Brandon K. Walther, an M.D/Ph.D. student in both Dr. Guissepi-Eli's Laboratory (Texas A&M Biomedical Engineering Department) and Dr. John Cooke's Laboratory (Houston Methodist) helped us perform real-time quantitative reverse transcription polymerase chain reaction (RTq-PCR). Lastly, Dr. Biswajit Saha, from Dr. Jain's Laboratory, aided in the completion of MAGPIX.

All other work conducted for the dissertation was completed by the student independently.

This graduate study was supported by a Doctoral Diversity Fellowship from Texas A&M University. In addition, this work was made possible in part by grants from the

National Institutes of Health (NIH DP2 EB026265) and National Science Foundation (NSF CBET 1705852). Its contents are solely the responsibility of the authors and do not necessarily represent the official views of the NIH or NSF.

NOMENCLATURE

3D	three-dimensional
VSMCs	vascular smooth muscle cells
ECs	endothelial cells
TNF- α	tumor necrosis factor-α
OCT	optical coherence tomography
RTq-PCR	real-time quantitative reverse transcription polymerase chain reaction
ECM	extracellular matrix
IL-8	interleukin-8
MCP-1	monocyte chemotactic protein-1
PDGF	platelet-derived growth factor
2D	two-dimensional
vWF	von Willebrand factor
LPS	lipopolysaccharide
PDMS	polydimethylsiloxane
Epi	epinephrine
CCH	carbachol
hiPSC	human-induced pluripotent stem cells
PAT	photoacoustic tomography
nSi	nanosilicates

GelMA	gelatin methacryloyl
PEGDA	poly (ethylene glycol) diacrylate
nECM	nanoengineered extracellular matrix
UV	ultraviolet
G’	storage modulus (Pa)
G”	loss modulus (Pa)
VE-Cadherin	vascular endothelial-cadherin
eNOS	endothelial nitric oxide synthase
α-SMA	α-smooth muscle actin
CNN1	calponin 1
TAGLN	transgelin
TCPS	tissue culture polystyrene
IL-1β	Interleukin 1β
IL-6	Interleukin 6

TABLE OF CONTENTS

Page

LIST OF FIGURES

Page

LIST OF TABLES

Page

1. INTRODUCTION*

1.1 Introduction to Emerging Trends in Multiscale Modeling of Vascular Pathophysiology: Organ-on-a-chip and 3D Printing

Vascular diseases, such as atherosclerosis, aneurysms, peripheral artery disease, and thrombosis, are the leading cause of morbidity and mortality worldwide, accounting for over 17 million deaths per year. (1) Despite major advancements to develop therapeutic interventions, the pathophysiology as it applies to humans is still largely unclear and treatments limited. If the status quo remains, the number of deaths is projected to reach epidemic proportions by 2030 (>23.6 million). (1) Thus, there is a crucial need to increase our understanding of vascular pathophysiology and assess emerging interventions to accelerate therapeutic development.

In order to model vascular pathophysiology and the influence of various factors (e.g. drug, toxins, biological agents), animal models and cell culture techniques are the current gold standard. The aim of these systems is to recapitulate the biological functions from the subcellular level to the whole organ and has contributed immensely to our current

---

* Reprinted with permission from "Gold K.A.; Gaharwar A.K.; Jain A. Emerging Trends in Multiscale Modeling of Vascular Pathophysiology: Organ-on-a-chip and 3D Printing. Biomaterials, vol. 196, pp. 2-17, 2019." Copyright 2019 Elsevier.

understanding of vascular diseases and potential treatments. However, animal models and cell culture techniques do not adequately mimic human *in vivo* microenvironments at these multilevel scales (**Figure 1-1A**). Moreover, these systems do not permit for dissectible analysis of cell signaling mechanisms, therefore limiting their translational potential. Consequently, there is an unmet need to introduce a more predictable vascular disease model. In order to accomplish this, modeling approaches that evaluate molecular, cellular, tissue, and organ level variables are required for a systematic and robust assessment of mechanisms and therapeutic interventions in blood vessels.

In this review, our focus is on recent advances in multiscale modeling of vascular pathophysiology. First, the need for modeling vascular physiology of healthy and diseased tissues will be briefly discussed, followed by a critical evaluation of animal models and *in vitro* culture systems. Then we will discuss the potential of organs-on-a-chip and three-dimensional (3D) printing as more predictive modalities, each having distinct advantages and limitations. For example, the organ-on-a-chip technology is able to form tissue-tissue interfaces and combine physiological flow conditions in a variety of disease and organ models. However, these systems often contain a rectangular cross-sectional area, compared to round blood vessels. Alternatively, 3D printing can produce anatomically accurate vascular anatomy, including bifurcations and curvatures of vascular networks. However, 3D printed constructs are often difficult to integrate optical imaging techniques due to their large size. Nevertheless, the unique aspects of organs-on-a-chip and 3D

printing techniques are making them increasingly popular tools to understand the pathophysiology and function of patient-specific vascular diseases (**Figure 1-1B**). This is supported by an increased number of publications over time pertaining to organ-on-a-chip and 3D printing vascular disease models (according to ISI Web of Science, July 2018) **(Figure 1-1C).** Due to recent advances in the field of biomaterials, microfabrication, and additive manufacturing, we predict that these emerging *in vitro* vascular disease models will advance basic science and serve as a translational platform to design novel therapeutics and repurpose existing drugs.

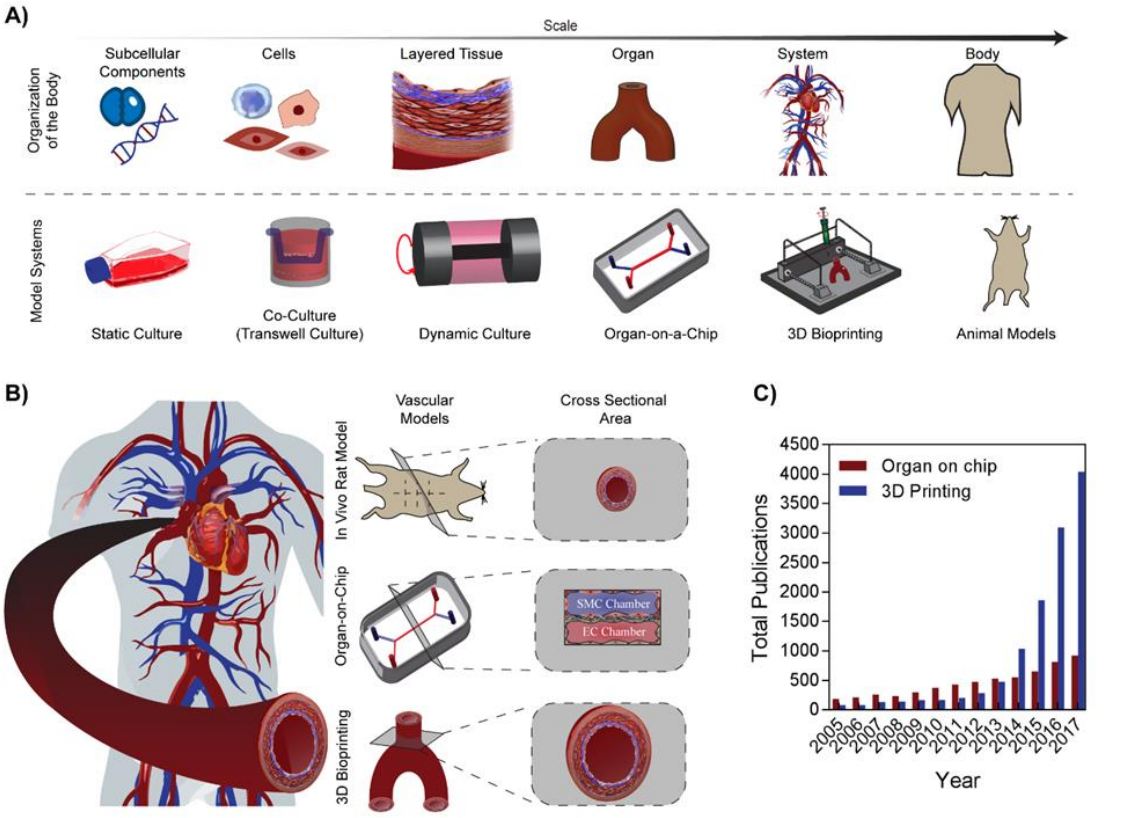

Figure 1- 1 Existing and emerging multiscale models of vascular diseases. A) Schematic illustrating the model systems used to replicate the organization of the body. As the scale increases from subcellular components to the whole body, the modeling modalities increase in complexity and decrease in the biochemical tools available to assess the model. B) The human vascular system can be modeled using the standard *in vivo* rodent model (smaller cross-sectional area), organ-on-chip technology (rectangular cross-sectional area), and 3D bioprinting (mimics the innate human vascular system). C) Number of publications related to "vascular models" over the past 12 years, with search keywords "3D Printing or Additive Manufacturing or 3D Bioprinting and Vascular Model" and "Organ-on-Chip or Microphysiological System or Tissue Chip and Vascular Model" according to ISI Web of Science (Data obtained in July 2018).

1.2 Need for Modeling Vascular Systems and Pathophysiology

The vascular system is the largest organ in the body, which controls the transport of fluid to and from tissues. The vessels within the circulatory system form a multilayered architecture composed of endothelial cells (ECs), vascular smooth muscle cells (VSMCs),

fibroblasts, and extracellular matrix (ECM). The innermost, or intima layer, contains a confluent layer of ECs that align with the direction of fluid flow. This layer serves as an active, selectively permeable barrier between the vessel wall and circulating fluids. (2) The tunica media, or middle layer, is predominately composed of VSMCs arranged circumferentially around the intima layer, providing structural stability and contractility to control blood flow. (2, 3) VSMCs deposit collagen bundles around interconnected layered elastin networks, accounting for a majority of arterial mechanical properties. (4) The combination of elastin and collagen provide non-linear elasticity to the vessel wall. (5, 6) The outer layer, or adventitia, is composed of fibroblasts and loose connective tissue, serving as an anchor for the vessel. (7) Together, this lamellar structure maintains several biological functions of the blood vessel, such as regulation, extravasation, or intravasation. (8)

Vascular diseases result from changes in both structure and function of the blood vessel. For example, arteries may undergo structural changes due to degenerative conditions, infection, or inflammation, causing disturbed blood flow. (9) This compromised flow results in an activated endothelium. (**Figure 1-2**) (10) For example, once the endothelium becomes activated in atherosclerosis, monocytes and leukocytes are recruited and inflammatory cytokines are secreted. (11) Prothrombotic mediators are also released, encouraging platelet activation and VSMC proliferation. (11, 12) Overall, these functional changes initiate geometrical modifications to the vessel, growing lesions that radially push towards the lumen, decreasing the vascular diameter, causing arterial hardening (6, 9, 10),

and recruiting collagen fibers within the medial layer to support the vessel wall. (13, 14) Therefore, the dynamic complexity associated with human vascular diseases, specifically the vascular wall, is extremely difficult to fully recapitulate. However, vascular disease modeling is essential to aid in the development of a cohesive understanding of disease progression and ultimately, find immediate interventions. A predictable and translatable model should include the cross-talk between essential cellular and tissue components, specifically ECs, VSMCs, ECM, and blood constituents. The components needed and models used sets the stage for the biological problem to be solved.

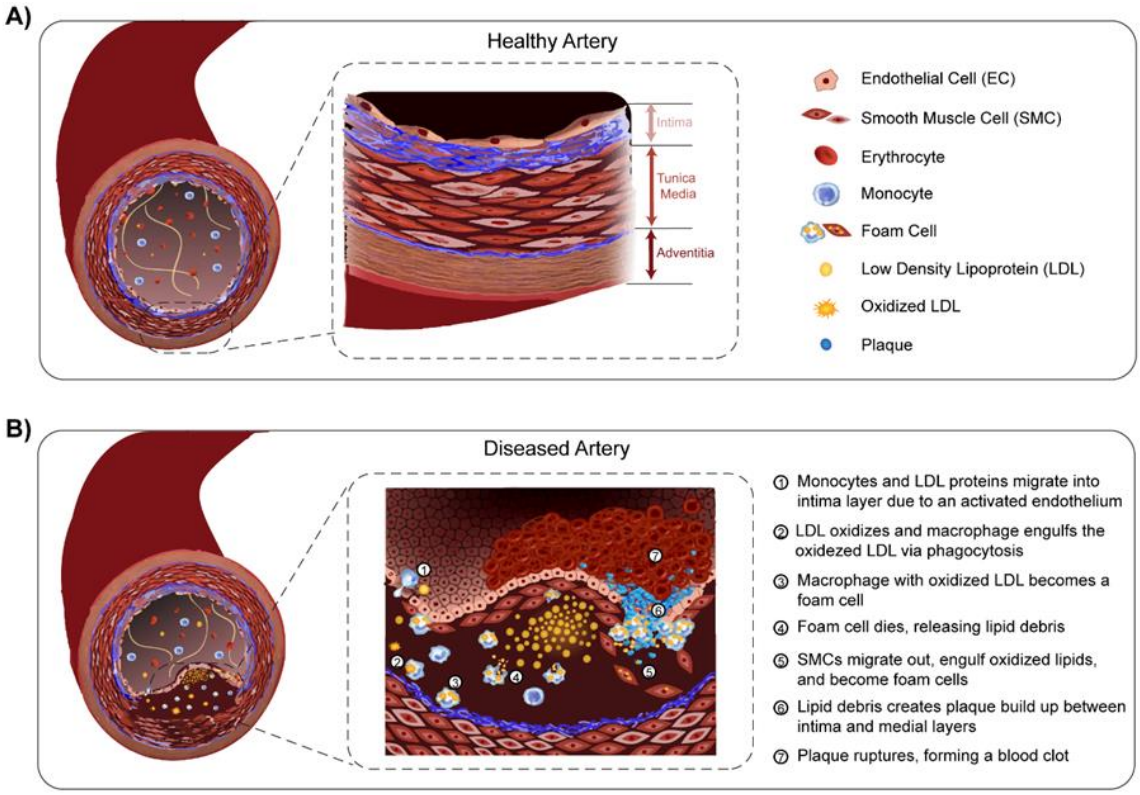

Figure 1- 2 Complex composition of an artery. A) Basic anatomy of a healthy, human arterial blood vessel, containing the intima, tunica media, and adventitia layer. B) Illustration of the complex pathophysiological development and progression of vascular disease causing a structural and functional change in arteries.

1.3 Animal Models

Animal models have been extensively used to develop of our current understanding of vascular diseases and treatment strategies. A major advantage of these systems is their ability to provide an integrated, multi-organ response to a diverse range of experimental variables (for example, environmental factors, diet, drugs and toxins). Specifically, these models contain multi-cellular and dynamic tissue environments, thus eliciting a whole-body response that can be measured and utilized to predict a human response to match the

pre-clinical stage of scientific discovery. For example, animal models have contributed immensely in the discovery of lipid-binding proteins, lipid-transfer proteins, cholesterol transporters, and enzymatic pathways in vascular disease genesis and progression. (15, 16) The mechanistic insight gained from animal models has aided in the development of interventions such as, tissue plasminogen activator to eliminate blood clots, several antiplatelet/anticoagulants to reduce the likelihood of blood clot formation, and ion-channel blockers to regulate muscle contraction/arrhythmias. (17-19)

While several animal species are utilized, rodent models are most frequently used due to ease of genetic manipulation, breeding, maintenance, cost, and time frame. (20, 21) Contemporary molecular and genetic manipulations, such as the creation of hypercholesterolemia apolipoprotein E gene and low-density lipoprotein receptor knockout has humanized mouse models, thus enabling the study of inhibitors on vascular diseases and atherosclerosis with higher precision. (19, 22) Nevertheless, rodents exhibit several characteristics that differ from humans, limiting their ability to model human physiology and innate disease development. For example, lesion disruption and lipoprotein content is not identical between humans and mice. (23) Vessel sizes, blood composition, and biophysical properties exhibited by rodents can be vastly different from humans, thus providing poor predictive value to disease outcomes. Given such large discrepancies between these two species, large animal studies are often required even if rodent models are used.

Large animal models (i.e. porcine, rabbits, baboons, non-human primates), being closer in anatomy and genetic composition to humans, are used in advanced preclinical trials to model complex signaling pathways of vascular diseases and drug responses. The large size of these animals provides an increased tissue availability for histological analysis and facilitates non-invasive measurements, such as measuring vascular hemodynamics. (24) In addition, these models provide a more accurate representation of human metabolism and vascular anatomy (heart size and coronary circulation). (22) Therefore, large animal models have, thus far, predominately contributed to the drug discovery process in vascular diseases. (23, 25) However, large animals cannot easily undergo genetic modifications, thus diminishing their translational potential. (26) Furthermore, it is extremely difficult to dissect specific signaling pathways and analyze tissue-tissue or cell-cell interactions independent of other environmental factors. To overcome the anatomical and physiological limitations of rodent and large animal models, non-human primates serve as ideal candidates, closely reflecting the innate biological processes within human vascular systems. Non-human primates (i.e. chimpanzees, baboons) are phylogenetically closest to humans, having analogous diet, metabolism, and development of vascular disease as they age. (27-29) However, use of non-human primates contain significant ethical restrictions and pose as a threat to maintaining biodiversity, therefore limiting their clinical practice. (27)

In summary, animal models are able to provide full cellular compositions and complexities observed in human blood vessels, making them an indispensable tool for vascular disease modeling. However, the results obtained from animal models can be difficult to extrapolate, interpret, and do not always relate to human pathophysiology, limiting the translation potential of these models. (**Table 1-1**) As a result, bioengineered *in vitro* approaches, containing human-derived living cells within relevant microenvironments complement animal models and perhaps, even remove their need in the future.

Table 1-1. Advantages and limitations of animal models of vascular diseases.

	Rodent Models	Large Animal Models	Non-human Primates
Advantages	+ Ease of genetic manipulation, breeding, costs and time frame	+ Close to human anatomy (i.e. hear size and coronary circulation) + Close to human genetic composition (i.e. lipoprotein metabolism, enzymatic activity, cholesterol distribution) + Circulating volumes reflect similar volumes to humans + Increased tissue availability + Facilitates in collection of non-invasive measurements	+ Phylogenetically closest to humans (i.e. analogous diet, metabolism) + Develop vascular disease with age + Close to human genetic composition (i.e. lipoprotein metabolism, enzymatic activity, cholesterol distribution) + Increased tissue availability + Facilitates in collection of non-invasive measurements
Limitations	– Compromised lesion development – Varied anatomy – Increased heart rate – Diverse lipoprotein ranges – No expression of cholesteryl ester transfer protein – Inability and infrequency of plaque rupture and thrombosis	– Restrictions on genetic manipulations to mimic human physiology – Difficult to extrapolate, interpret, and relate data to humans – Difficult to isolate relevant tissues/cells for experimental response – Inability and infrequency of plaque rupture and thrombosis	– Significant restrictions due to ethical concerns – Threat to maintain biodiversity – Require long-term experimentation

1.4 *In Vitro* Models

While animal models provide a top-down modeling approach, *in vitro* techniques offer a bottom-up approach to model complex pathophysiology of vascular disease. (30) As a result, *in vitro* models allow for the examination of specific cellular and molecular signaling events under defined chemical and mechanical conditions, thus making them an easily tunable system with reduced complexity. *In vitro* models can be static cultures of

cells or include complex dynamic conditions, mimicking the *in vivo* environment more closely. However, both approaches have advantages and limitations, specifically depending upon the purpose of the application.

1.4.1 Static *In Vitro* Culture Systems

Since endothelial cells (ECs) line the walls of all blood vessels and are central contributors to vascular function, most *in vitro* models analyze vascular diseases with EC monolayers. (31-39) Static well-plate systems with EC monoculture are simple to use and can be multiplexed. As a result, these systems have become the gold standard to understand endothelial biology (40), responses to internal or external environment changes (41-47), and for high throughput screening applications (17, 48).

Nevertheless, blood vessels are multicellular organs, containing external layers of VSMCs, fibroblasts, epithelial cells, and embedded ECM. Several cadherin and integrin interactions occur within this lamellar structure that regulate cell behavior. (7, 17, 49-52) For example, ECs within the intima layer interact with VSMCs in the media layer. This interaction controls the upregulation of inflammatory cytokine expression (i.e. interleukin-8, IL-8, and monocyte chemotactic protein-1, MCP-1) and platelet-derived growth factor (PDGF), while inhibiting collagen and fibroblast growth factors. (50) These cell-cell and cell-ECM interactions are critical for maintenance of proper blood vessel function. In order to achieve these EC-SMC cadherin interactions, various static co-culture systems have been utilized. (48, 53-55) Co-culturing ECs and SMCs have shown mutual physical

interactions that impact cell morphology, proliferation rate, and protein synthesis through the excretion of diffusible mediators. (48, 53, 55)

Despite frequent use, monoculture or co-culture well-plate systems cannot recapitulate the dynamic intercellular and organ-level signaling experienced by blood vessels. This is mainly due to changes from a natural 3D tissue environment to 2D tissue culture, where the cells become exposed to a significantly altered microenvironment (e.g. surface stiffness, biochemical composition, local cell density). (56) As a result, these static systems can also alter cell phenotype, thus reducing the predictive power of these systems. (14, 56) For example, SMCs lose contractile proteins upon culture, rendering them incapable to modulate vascular tone. (50) Furthermore, static cultures cannot incorporate shear-dependent cell and tissue responses. For example, when the lumen is subjected to pulsatile blood flow, ECs respond through shear-sensitive ligands and integrins communicating with other regions of the vessel that respond to these signals. ECs respond to changes in shear by secreting or metabolizing vasoactive substances, such as nitric oxide and/or endothelin-1, inhibiting or exciting SMC growth, vasoconstriction, or vasodilation. These perturbations are impossible to mimic in 2D culture assays and therefore, flow-based culture systems are required to undertake such investigations.

1.4.2 Dynamic *In Vitro* Culture Systems

In order to integrate mechanical forces into *in vitro* cell culture systems, parallel plate or two-dimensional perfusion flow chambers have been extensively used. (57, 58)

Traditional flow chambers are hollow conduits that provide a means to expose EC monolayers to fluidic forces on the millimeter scale, thus making it possible for the assessment of biophysical alterations involved in vascular disease. (59-61) However, due to the large volume of the conduit, these techniques consume large amounts of medium, bioactive factors, and cells. Moreover, these macroscale devices do not represent the micro-physiological environment of smaller blood vessels, such as arterioles or capillaries. Recently, advances in microfabrication techniques have enabled rapid manufacturing of micron-scale flow chambers, termed microfluidic devices. These devices provide a reproducible and low-consumption platform to more precisely control biological conditions and the dynamic fluid environment relevant to arterial blood vessels and vascular diseases. (62, 63) A salient feature of microfluidic devices is that they allow quantitative assessment of hematological and microvascular processes of vascular disease. For example, a broad range of velocities that exists in the vascular system - ranging from 0.3 m/s in the aorta to 0.1 μm/s in vascular branches at the capillary level (64) - can be applied within microfluidic devices, thus enabling assessment of diverse shear-dependent signaling within the endothelium. In addition, flow perfusion provides a mechanism to continuously transport and distribute soluble factors, permitting for long-term cell culture and providing a resource to model physical influences on cells (such as the rolling, decelerations, and arrests of blood-components with the endothelium). (65) Overall, microfluidic methods have been shown to study whole-cell responses, rather than individual mechano-receptors. (66, 67) A major advantage of this platform is its ability to include parenchymal cells and ECM, enabling for a method to model the complex

epithelial-endothelial-blood signaling that occurs in vascular diseases, thus functioning as organs-on-a-chip or micro-physiological systems.

1.5 Emerging Approaches

From existing animal models and *in vitro* systems, a major hurdle in vascular science and the drug discovery process is the inability of these techniques to reliably predict therapeutic targets and toxicities applicable to humans. As a result, major successes in pre-clinical trials have resulted in failures when translating to human clinical trials. A key reason for this problem is the inability of current modeling systems to recapitulate organ-level architectures and functions critical to the assessment of drugs, toxins and chemicals at a disease- and patient-specific level in humans. Therefore, there is a necessity for new disease models to emerge. With the advent of easy microfabrication methods, automated instrumentation, new biocompatible materials, stem cell differentiation to defined cell lineages, and molecular tools, microfluidic organ-on-a-chip devices and 3D printing have spurred new innovation and shown strong potential to address this unmet challenge. These emerging approaches provide a unique solution by increasing the translational potential of these platforms to model human physiology and decreasing the mechanistic complexity associated with the experimental outputs. For example, microfluidic organ-on-a-chip devices can provide biological insight into pathophysiology by providing direct access via microscopy, biosensors, and genomic screening. In contrast, 3D printing can be used to fabricate a patient specific vascular disease model by recapitulating the structural and functional aspects of native tissues.

1.5.1 Organ-On-A-Chip

Recently, a new class of microfluidic devices, known as organ-on-a-chip or micro-physiological systems, has emerged and shown to recapitulate 3D tissue architectures and physiological flow conditions in a variety of disease and organ models. These systems have recreated the microenvironment of lung, liver, gut, kidney, skin, intestine and many other organs (56, 68-73), where cadherin interactions, tissue-tissue communication, and mechanical stimulation of fluids can be controlled in a physiologically-relevant manner that is not currently possible with animal models or classic *in vitro* systems. Organ-on-a-chip is broadly defined as the minimum assembly of cells in a microenvironment that mimics an organ-level function of a human. Importantly, this platform can include the endothelium, complex blood flow (such as patterns observed in stenosis or aneurisms), and the inclusion of mechanical forces that govern endothelial activation. (**Figure 1-3A**) This offers enormous potential to model vascular disease mechanisms with higher specificity and accuracy not offered with conventional techniques. (**Table 1-2**)

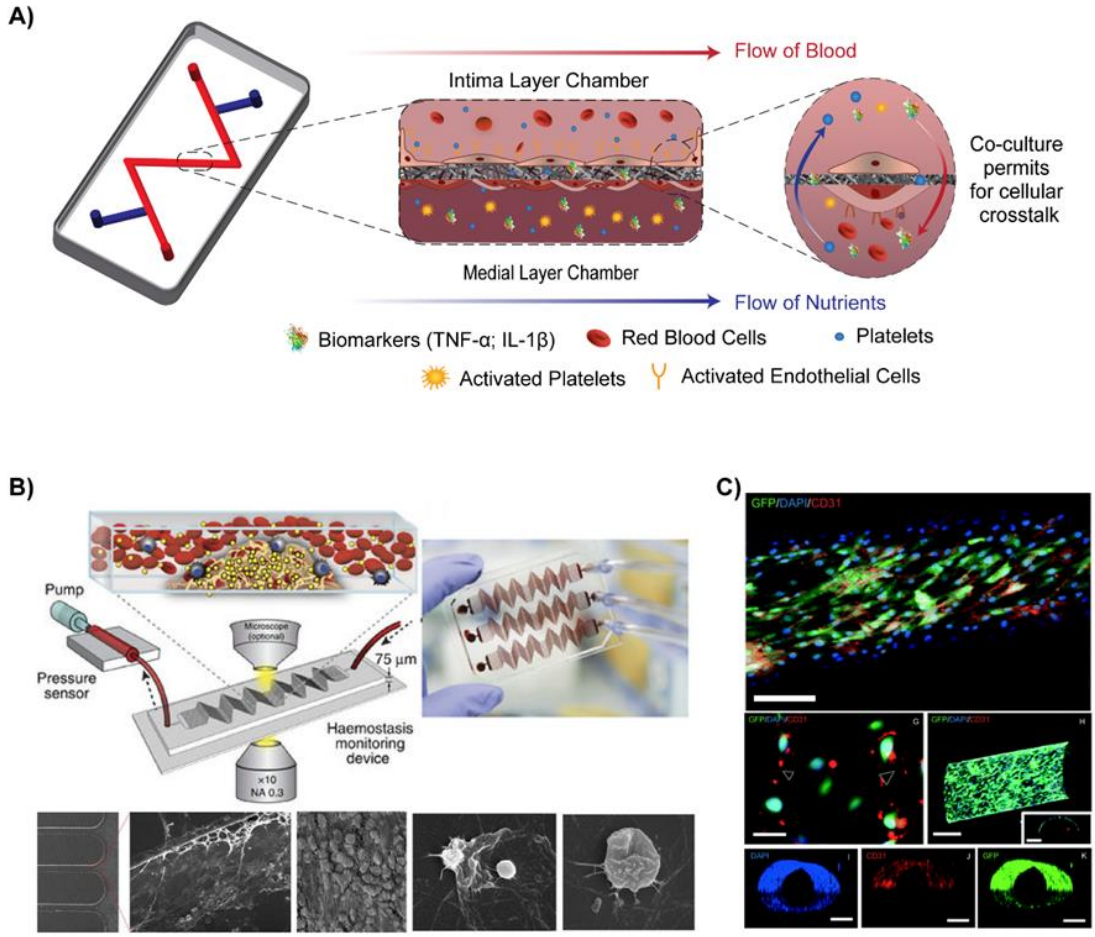

Figure 1- 3 Vascular organ-on-a-chip models. A) Illustration depicting the cellular communication and dynamic environment within a multi-chamber organ-on-a-chip. B) Schematic depicting a hemostasis organ-on-a-chip device, top left. Exposure of blood flow within the microfluidic channel permits for determination of clotting time and the high throughput potential of organ-on-a-chip devices. Scanning electron micrographs of blood clot formation within the device, bottom, illustrating fibrin networks with red blood cells (3 left images) and activated platelets (2 images at right) (72) © 2016 Nature Communications. C) Confocal image of GFP/DAPI/CD31 biomarkers from endothelial cell monolayer inside microchannel, depicting cellular interactions. (Top – Scale bar 250 µm; G – Scale bar 50 µm; H, I, J, and K – Scale bar 250 µm) (74) © 2014 Lab on Chip.

Table 1-2. Bioengineered vascular disease models using organ-on-a-chip technology.

Material	Cell Type(s)	Blood flow conditions	Experiment	Ref.
PDMS	Mouse olfactory harvested arterial segments	Perfusion inlet was subjected to 45 mmHg and the outlet at atmospheric pressure.	Artery segments were reversibly loaded onto device; verified cellular arrangement of artery in chip by staining SMC nuclei, actin, and voltage gated calcium channels; vessel constriction was reduced by 50% after incubating with calcium-blocker nifedipine	Yasotharan et al.(68)
PDMS coated with VWF/fibrinogen	HUVECs	Parallel microchannels with one-side stenosis of 20, 30, 40, 60, or 80 percent lumen reduction; human blood was perfused at 1,000 s^{-1} input wall shear rates	Stenotic chambers demonstrated enhanced platelet aggregation in 60 – 80% occlusion over a range of input wall shear rates; flow increases EC VWF secretion in stenotic outlet, causing platelet aggregation and post-stenotic thrombus formation	Westein et al.(75)
Gelatin-Agarose IPN	HUVECs, HDMVECs, HLMVECs	Physiologically relevant stiffness ~ 20 kPa (stiffness of healthy arteries between 1 and 35 kPa); Flow velocity in smallest channels set to ~2.8 mm s^{-1} (corresponding to a wall shear stress ~8.8 dynes cm^{-2})	Stiffer IPNs (~50 kPa) resulted in increased permeability compared to soft devices (~5 kPa); Extracellular haem (haemolytic by-product) induces delayed and reversible EC permeability (dose-dependent manner)	Qui et al.(76)
PDMS and collagen	hBMSCs, hFs, HUVECs, HASMCs	No profusion mentioned	Inflammatory factors (LPS, thrombin, and TNFα) compromises EC barrier function; Simultaneous inhibition of Rac1and activation of RhoA induced loss of HASMC exposure to HUVECs and reduced barrier function; CRISPR-mediated knockout of *N*-cadherin in HASMCs led to loss of barrier function and over expression in *N*-cadherin (validated in mouse)	Alimperti et al. (77)
PDMS coated with collagen	HUVECs	Perfused human citrated whole blood at a flow rate of 0.29 mL min^{-1}, yielding a shear rate of ~ 1,000 s^{-1}	SLA printed miniaturized vascular structures that closely mimic stenotic and healthy blood vessel architecture; 15 minutes of blood perfusion revealed induced thrombosis down-stream and at the stenotic regions whereas healthy geometries showed no platelet adhesion	Costa et al.(78)

Table 1-2. Continued.

Material	Cell Type(s)	Blood flow conditions	Experiment	Ref.
PDMS	Resistance arteries isolated from wile type CD1 mice or CD1 mice expressing Tie2-GFP transgene in ECs	Harvested arteries were fixed at periphery and subjected to external pressure of 45 mmHg above atmosphere (aligned artery); Disk of sapphire uniformly distributed heat generated by thermoelectric heater; Flow in channels between 0 – 4 mL h^{-1}	Developed a microfluidic platform to assess resistance artery structure and function; fully automated acquisition of up to ten does-response sequences of intact mouse mesenteric artery segments; Exposure of phenylephrine or acetylcholine yield dose-response relationship identical to human response	Günther et al.(79)
PDMS	HUVECs, HMVEC	Citrated human blood was perfused to obtain a wall shear rate of 750 sec^{-1} (~ 10 dynes cm^{-2} stress); for platelet-endothelial dynamics, higher wall shear rate was used (750 sec^{-1}; ~30 dynes cm^{-2} stress)	Performed quantitative analysis of organ-level contributions to inflammation-induced thrombosis; LPS endotoxin directly stimulates intravascular thrombosis by activated alveolar epithelium; analyzed inhibition of EC activation and thrombosis due to PAR=1 antagonist	Jain et al.(80)
Fibronectin crosslinked gelatin	iPSC, NRVMs	Bulk elastic modulus of ca 50 – 100 kPa; lower concentrations obtained modulus between 1 and 15 kPa	Micropatterned gelatin hydrogels using laser-etching to obtain surface grooves and pillar structures with a resolution of 15 μm; verified structural organization, contractile function, and long-term viability compared to manually patterned gelatin substrates	Janna et al.(81)
PDMS	HAECs and HASMCs	Vacuum side channels induce cyclic strain of 5 – 8% to mimic stretching and relaxation of the channels; flow in EC chamber produced a wall shear stress of 1 – 1.5 PA	Culture of SMCs and EC with a porous membrane separating the two chambers lead to prolonged viability of cells that exhibited physiological morphology and organization through cell-cell contact;	Engeland et al.(82)

Recent studies have shown that atherothrombotic processes and platelet aggregation can be modeled with the organ-on-a-chip platform. (70, 75, 83) In one study, a microfluidic device containing a parallel array of stenosed micro-vessels was able to form platelet and fibrin-rich blood clots downstream of stenosis, as observed *in vivo*. (72) This device was then applied to predict anticoagulant and antiplatelet drug responses in patients on extracorporeal devices. (**Figure 1-3B**) Another *in vitro* study, applying a similar geometry, validated that cell-secreted von Willebrand Factor (VWF) further exacerbates platelet recruitment and adhesion post-stenosis, similar to *in vivo* conditions. (31) Furthermore, another microfluidic study (vessel-on-a-chip) lined with living or chemically fixed human endothelium was demonstrated to modulate hemostasis and thrombosis under arterial flow, thus serving as a potential diagnostic lab-on-a-chip device. (70, 74) (**Figure 1-3C**) More recently, this vessel-on-a-chip system was able to predict toxicity of a drug compound that failed clinical trials, but did not produce the same vascular side effects in primate studies. (84) Also, this organ-on-a-chip platform has provided more mechanistic understanding of vascular biology. For example, a recent work with microfluidic channels showed that proteins RhoA, Rac1, and N-cadherin regulate vascular permeability and barrier function. (85) Furthermore, immune cell interactions have also been assessed in these systems, demonstrating the role of inflammatory cells, such as neutrophils and T-cells, in endothelial activation and consequent thrombosis formation. (86-88)

More complex diseases, such as cancer, infectious diseases, and genetic disorders (e.g., sickle cell disease), compromise the vascular system in patients and often instigate fatal

strokes. Tissue- and cell-level signaling may constitute feedback between multiple organs that regulate the vascular function. For example, in cancer tumor cells release inflammatory factors that result in vascular dysfunction. (38) Similarly, in pneumonia and other respiratory disorders, the alveolar epithelium may secrete factors that lead to platelet recruitment and thrombosis. (39) Organ-on-a-chip technology has been deployed to dissect tissue-tissue and drug-tissue interactions for systematic analysis of such vascular diseases. Recently, a model of lung thrombosis supported tissue-level functional design by showing co-culture of human primary alveolar and an endothelial lumen in adjacent microfluidic conduits, separated by thin, porous membrane. (26) After the introduction of lipopolysaccharide (LPS) in the epithelial channel followed by whole blood perfusion through this device, a thrombus formed within the luminal channel, accurately reflecting upon *in vivo* observations. Further, an endothelium-specific therapeutic effect of antithrombotic compounds was identified with this system, which was not observed with traditional animal models. These developments in vascular micro-physiological systems are highly promising and provide major opportunities to investigate biological function with microscopic techniques, measure variables using biosensors, and quantify outputs using analytical algorithms and genomic screenings.

However, there are still limitations in the current microfluidic designs that restrict the extent to which vascular disease pathophysiology can be reconstituted. Virtually most published literature on organ-on-a-chip technology is based on the use of polydimethylsiloxane (PDMS) for fabrication. The process of fabrication with PDMS,

called soft lithography, is simple and adoptable to most lab environments. With soft lithography, multi-chamber microfluidic devices separated by thin film membranes to support tissue co-cultures can be designed with high fidelity. PDMS is also biocompatible, transparent, and permeable to gases, making it very suitable for cell culture. However, a major drawback of PDMS is that the material adsorbs small hydrophobic molecules, therefore making it very difficult to assess pharmacokinetics of drugs and toxins. For example, if the drug is absorbed by the PDMS, then its net concentration is lower, and potential therapeutic effect or toxicity might be underestimated. Thermoplastic materials are potential alternatives that have been used to make microfluidic chips, but they often auto-fluoresce during imaging, do not permit for oxygen diffusion (making it harder for cells to survive for long durations) and can be very expensive for a high-throughput setting. Another potential limitation is that organ-on-a-chip models are subsets of the whole living organ. For example, the blood vessel-on-a-chip models published so far lack connective tissue containing fibroblasts between the epithelium and endothelium, which may regulate vascular homeostasis and pathogenesis. In addition, pericytes or SMCs may need to be integrated under the endothelium for a complete biological output from these models. This is not necessarily a drawback because with this approach, scientists can design the simplest model required to solve a biological problem and add additional cell types until the required combination is achieved for solving the problem of interest. For example, blood flow in arteries is pulsatile and would be a very interesting addition to vascular organ-on-a-chip technologies in the future. Yet, a major hurdle that still exists is the phenotype expressed by the cells used in these model systems. Specifically, cells

within these systems may not present the phenotype native to the local environment of the disease or patient anatomy, and therefore, standardization of cell-lines and growth protocols is necessary (30, 89, 90). In addition, given the planar and thin (<1 mm in thickness) cellular arrangement, modeling drug-tissue interactions may be inaccurate and require careful scaling up due to varied drug pharmacokinetics and pharmacodynamics (35, 56, 91-94). Also, organ-on-a-chip models may not always include the same cellular arrangements as observed *in vivo*. They are often designed as overlaying or side-by-side rectangular channels which make them unable to recapitulate the exact flow inside a cylindrical blood vessel. This may also alter endothelial function and affect the contractility-related mechanisms of cells. Finally, despite promising use of organ-on-a-chip, these models may not be appropriate to model the macroscale organ biology, for example, aorta or veins and therefore, different tools may be needed for such investigations.

1.5.2 3D Printing

Given vascular diseases often originate in blood vessels with complex geometries, additive manufacturing, such as 3D printing (including 3D bioprinting), offers a vital tool to recapitulate a diseased anatomy. 3D printing is a fabrication technique used to mimic the anatomical complexity of native tissues *via* a bottom-up approach by depositing polymeric or cell-laden hydrogel based inks in a layer-by-layer fashion. (95, 96) (**Figure 1-4A**) The use of 3D printing to fabricate intricate geometries, such as bifurcations and curvatures, provides a comprehensive understanding and functional evaluation of patient-specific

vascular disease symptoms. (97, 98) (**Table 1-3**) Recent advancements in 3D printing technology have resulted in the development of complex, anatomical structures, motivating its use in a variety of biomedical applications such as tissue modeling (99-101), pharmacological assessment of therapeutics (contractions of vascular wall in response to serotonin (102), endothelin-1 (102-104), prostaglandin $F_2\alpha$ (102), polyphenols from red wine (105, 106), and histamine (107)), and disease pathophysiology (neovascularization (108), EC permeability (109, 110), and hemodynamics (111, 112)).

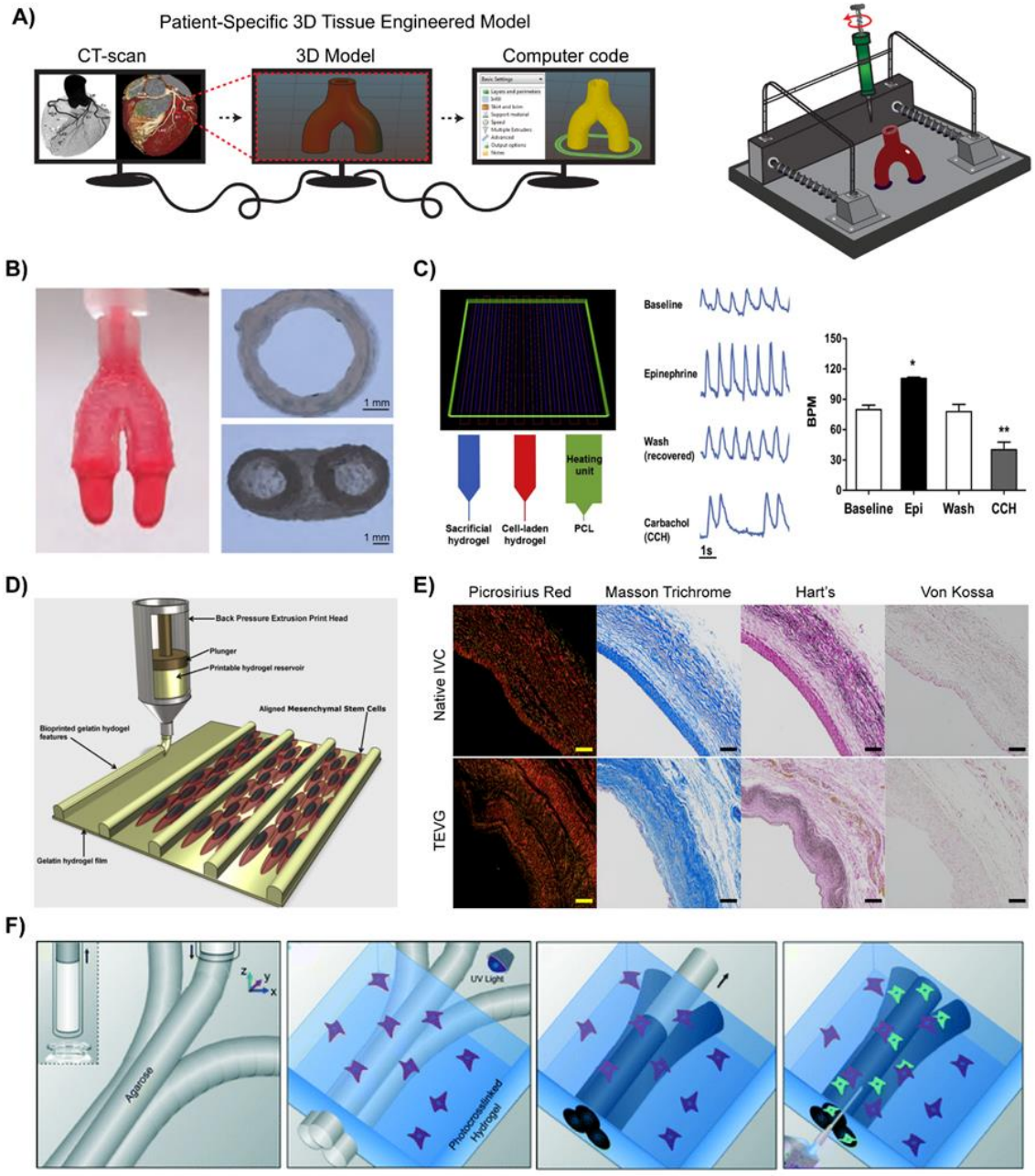

Figure 1- 4 Vascular 3D printed models. A) Schematic demonstrating the process of fabricating a patient-specific complex geometry using the layer-by-layer 3D printing process. B) A bioink utilizing Nanoengineered Ionic-Covalent Entanglements (NICE) improves the hydrogel's printability, producing stiff and elastomeric constructs that are physiologically relevant at modeling macroscale organ biology (113) © 2018 ACS Applied Materials & Interfaces. C) 3D printing of 3-component cardiac tissue to demonstrate the feasibility of modeling cardiac tissue drug response. The printed cardiac tissue increased in beating frequency (beats per minute; BPM) and amplitude, compared to the baseline, when exposed to epinephrine (Epi). However, once

removed, washed, established baseline, and then exposed to Carbachol (CCH), the opposite effect was noted (114) © 2018 Acta Biomaterialia. D) Schematic of the manufacturing process used to produce hydrogel printed microchannels that aid in cellular alignment, mimicking the arrangement observed *in vivo* (115) © 2018 Biofabrication. E) Collagen (Picrosirius Red and Masson Trichrome) and elastin (Hart) deposition of a native inferior vena cava (IVC) compared to a 3D printed tissue engineered vascular graft (TEVG) after 6 months. No signs of ectopic calcification were demonstrated (Von Kossa) (116) © 2017 The Journal of Thoracic and Cardiovascular Surgery. F) Graphic representation of the use of 3D printing to form microchannels *via* template micro-molding, permitting for the use of dynamic co-culture within a printed construct (74) © 2014 Lab on chip.

Table 1-3. Bioengineered vascular disease models using 3D printing technology.

Material	Cell Type(s)	Mechanical Conditions	Experimental Specifications	Ref.
GelMA for bulk material and Pluronic F-123 for sacrificial microchannels	HUVECs, hDFs	Reynolds number lower than 0.5 for flow rates between 0.6 and 3 mL h^{-1} (laminar flow); main velocities in main channel between 0.19 and 0.54 mm s^{-1}; burst pressure: ~ 0.16 ± 0.08 kPa; Compression moduli varied between0.8 kPa to 0.65 kPa	Sacrifical bioprinting produced hDF encapsulated in GelMA with microchannels (washed out pluronic) devices lined with a confluent layer of HUVECs; profusion of blood formed thrombi that was exposed to tissue plasmin activator and subsequent dissolution of non-fibrotic clots; hDF were able to migrate into the clot and deposited collagen over time	Zhang et al.(83)
Nanosilicates, GelMA, kappa-carrageenan	MC 3T3 Preosteoblasts	Addition of nanosilicates to the network induces a Herschel-Bulkley fluidic behavior, promoting a shear thinning profile with a power law index of 0.55	Utilized a ionic and covalent network stabilized by nanosilicates to produce high fidelity printed constructs; performed rheological modeling to determine optimal parameters for printing	Chimene et al.(113)
PEGDA, Alginate	PAVIC	Alginate was incorporated into bioink to increase precursor viscosity to permit for printing of high fidelity constructs; Lower weight percent of bioink had increased linear elasticity behavior, higher weight percent bioink exhibited nonlinear tensile stress-strain behavior	3D printing and photo-crosslinking technique to construct heterogeneous aortic valve to mimic the anatomic and axisymmetric geometries	Hockaday et al.(117)

Table 1-3. Continued.

Material	Cell Type(s)	Mechanical Conditions	Experimental Specifications	Ref.
Alginate, Collagen	Mouse fibroblasts, mouse SMCs, and HUVECs	Construct exhibited a linear stress-strain profile with an ultimate strength increases with increasing alginate concentration (0.049 MPa to 0.139 MPa); After 5 days of culture, the ultimate tensile strength decreased further to 0.105 MPa	3D printing of multi-level fluidic channels deposited in a layer fashion to replicate the hollow, lamellar vascular structure; demonstrated modeling potential using mechanical and chemical stimulation with a circulation flow system, an arterial surgery simulator, and cell co-culture	Gao et al.(118)
Bioink: Fibrin composites Sacrificial ink: Gelatin, glycerol, and hyaluronic acid	CM	Printed at 18C with a pneumatic pressure of 100 kPa and a speed of 100 mm/min; intrinsic force generated within printed construct was 1.5 mN	3D bioprinted organized and functional cardiac tissue; printed constructs elicited physiological responses to cardiac drugs to alter beating frequency and contractility forces	Wang et al.(114)
PGA-co-PLCL	Obtained through implantation	Burst pressure: 11,685 ± 11,506 mmHg (post-implant), 6,167 ± 5,627 mmHg (preoperative); Compliance: 4.0% ± 1.5% (preoperative), 2.3% ± 0.46% (post-implant)	Created a patient-specific nanofiber vascular graft combining electrospinning and 3D Printing; implanted in sheep, demonstrating no aneurysm formation or ectopic calcification; explanation revealed complete resorption of grafts, SMC organization, ECM deposition, endothelialization, and and similar mechanical properties to native vasculature	Fukunishi et al.(116)
PEGDA and GelMA	HUVECs, NIH/3T3 Fibroblasts	Viscous bioink (Reynolds number ~ 10 – 100) permits for smooth transitions between bioinks; Printing resolution ~ 20 – 30 μm	Stereolithography-based, multi-material bioprinting platform for heterogeneous hydrogel constructs; Constructs loaded with VEGF were assessed for its neovascularization potential	Amir et al.(108)
GelMA and agarose	HepG2/C3A cells (encapsulated); HUVECs (seeded)	Youngs modulus of GelMA ~ 12.1 ± 1.1 kPa; pore size of GelMA ~ 143.2 ± 6.4 μm; perfusion was conducted at 50 μL h^{-1}	Sacrificial bioprinting technique produced hollow microchannels; HUVEC layer delayed permeability of biomolecules and showed increased viability of HEPG2/C3A cells	Massa et al.(109)

A vital yet limiting component of the 3D printing design and implementation is the selection of materials, or bioinks. The materials used serve as an artificial ECM composed of natural, synthetic, or their combination to reproduce tissue microenvironments and permit for cellular functions observed in native ECM. Natural polymers encompass materials derived from natural sources, such as ECM constituents (e.g. collagen, elastin, and fibrin) or polysaccharide-based biomaterials (e.g. alginate, chitosan). (119-121) These materials often contain cell-adhesive domains, driving cell connection, migration, and proliferation. However, natural polymers often contain significant batch-to-batch variability as well as lack control over both the chemical and physical properties. To overcome the variability of natural polymers, synthetic polymers with desired chemical structures, mechanical integrity, and functionality can be used. (122, 123) Yet, synthetic materials lack biologically recognized domains, resulting in limited cell-matrix interactions. In order to enhance or obtain bioactivity, synthetic polymers are modified with cell-responsive structures, such as RGD-domains or natural polymers. Due to the inherent complexity of vascular tissue, combining both natural and synthetic polymers warrant for the fabrication of bioinks that can be finely tuned to obtain optimal material properties and enhanced bioactivity. (118, 124) The combination of both natural and synthetic polymers enables for precise manipulations to model tissue compositions, architectures, and microenvironments for either healthy or diseased conditions. (113, 117, 125) This permits for a dissectible analysis of physiological changes that occurs with geometry, disease progression, and aging. (118, 126)

In order to further recapitulate ECM properties of vascular tissues, such as conductivity, nanomaterials such as carbon nanotubes (127, 128), graphene oxide (129), and gold nanorods (130) can be integrated into polymeric networks. These nanomaterials can also be used to modify a material's printability to fabricate anatomically scaled tissue structures that model the macroscale organ biology. In a recent study, bifurcating vascular constructs were 3D printed into precise geometries. (113, 131) (**Figure 1-4B**) In this approach, bioink properties were optimized by controlling the interaction between nanoparticles and the polymeric network to obtain highly printable inks. (125, 131-134) Printability is a crucial property of bioinks that is defined by its ability to smoothly extrude into the intended architecture with high structural fidelity. These properties are governed by a material's rheological properties and crosslinking mechanisms. (135) Specifically, a bioink must first shear-thin, allowing for extrusion through a needle gauge, followed by rapid recoverability of the material's internal structure, permitting for shape retention into the deposited geometry. (125) A range of approaches have been developed to print custom scaffolds with enhanced fidelity, such as on-site curing of bioink (136, 137), printing into a support bath (138-141), or exposing ions or temperature changes to retain a deposited shape (113, 131).

Aside from print fidelity, bioink selection is crucial and can dictate cellular organization and functions. By modulating bioink properties, physical and chemical microenvironments of human vascular diseases can be replicated. (142) For example, recent studies have utilized 3D printing to design a cardiac patch by mimicking the

microenvironment to improve cardiomyocyte organization and maturity. (143, 144) (**Figure 1-4C**) This 3D printed model was able to produce physiological responses to adrenergic agonists (such as epinephrine; Epi - increases heartbeat frequency) and carbachol (CCH; decreases heartbeat frequency). (145) In a similar study, 3D printing was used to fabricate constructs with specific surface topography to control cellular adhesion and alignment. (114, 115) (**Figure 1-4D**) This approach is capable of mimicking some of the structural complexity observed with native vasculature. These proof-of-concept studies highlight the versatility of 3D bioprinting to mimic structural and functional complexity of vascular tissues.

Although printing design has been used to dictate cellular arrangement on printed scaffolds, construct topography, stiffness, and architecture also strongly impact the model's predictability, specifically regarding hemocompatibility. In healthy vasculature, blood does not clot due to a confluent layer of EC shielding the ECM from fluid contact. (146) The ECs prevent clotting through the release of biochemical cues to the blood, such as heparans, thrombomodulin, tissue plasminogen activator, and adhesion proteins to dictate vascular function. (147) However, when the lumen is disrupted or damaged, the underlying ECM elicits highly thrombogenic properties, triggering immediate platelet adhesion and thrombosis. (9, 148) Bioink properties can be tuned to prevent this clotting cascade and improve upon the ink's hemocompatibility. Specifically, sub-micrometer grooves on blood-contacting surfaces have been shown to decrease platelet adhesion and activation compared to smooth surfaces. (149-151) This is due to an increased surface area

and geometrical constraints for platelets to activate or adhere. In addition, increased matrix stiffness (~ 5-50 kPa) has been shown to significantly enhance platelet adhesion and spreading, *via* Rac 1 and actomyosin activity. (152-154) Aside from surface roughness and matrix stiffness, other strategies, such as the inclusion thrombin-resistant materials (155, 156) or chemical modifications of the construct's surface (157, 158) can greatly impact platelet interactions.

3D printing can also be combined with other fabrication techniques, such as solution blow spinning, photolithography, or self-assembly, to imitate more complex structural features of vascular tissues. For example, innate myocardium ECM consists of well-organized, anisotropic tissue architecture with conductive fibers. (159, 160) Electrospinning, an fabrication technique to obtain micro- and nano-fibers, can be used to mimic structural organization of myocardium ECM by providing topological clues for cell alignment and imparting directional properties. By combining electrospinning with 3D printing, a patient-specific vascular graft can be obtained, which is difficult to obtain from either technique alone. (116) (**Figure 1-4E**) The topological clues provided by electrospun fibers facilitate the formation of vascular tissue around the graft *in vivo* after 6 weeks. Interesting, the secreted ECM consists of predominantly collagen and elastin, similar to the native inferior vena cava. In addition, there was no observable calcification of the engineered graft. (116) This study indicates a strong potential to combine 3D printing with other fabrication techniques, such as electrospinning, to mimic the structural complexity of vascular anatomy. Aside from the combination of other fabrication techniques, 3D

printing has recently been used as a template for micro-molding. (74) (**Figure 1-4F**) Complex vascular microchannels can be printed out of a sacrificial bioink, such as agarose (74), gelatin (161), or Pluronics (119, 162, 163). After the printed microchannels solidify, cell-laden hydrogel precursor solutions can then be casted over the filament and photo-crosslinked. Subsequently, the sacrificial microchannel templates are removed from the surrounding crosslinked hydrogel. This fabrication technique enables the manufacturing of perfusable microchannels that permit for the co-culture of multiple cell types. The use of sacrificial material 3D printing provides a platform to create a fully perfusable microvascular network with different architectures and geometries.

Although 3D printed constructs are capable of mimicking the native structure of blood vessels and can model several aspects of vascular diseases, few significant hurdles still remain before this technology can be translated to preclinical trials or medical practice. Specifically, the lack of bioinks that truly mimic the mechanical and chemical properties of the ECM is a big limiting factor**.** For example, there is no bioink that provides an accurate representation of features observed in vascular diseases, such as calcified structures, mechanical and chemical variations within tissues, or differences in mechanical properties of vascular structures during dynamic or static states. (100) Moreover, biological arrangement of cells and tissues observed *in vivo* is challenging to control *in vitro*. Although use of electrospinning and other microfabrication technology along with 3D printing can be used to provide some control over cellular arrangement, this relies on cell's innate ability to self-organize. Overall, 3D printing is promising new approach to

mimic human vascular pathophysiology and has a strong potential to dissect tissue-tissue and drug-tissue interactions for systematic analysis of complex vascular diseases.

1.6 Future Prospects and Conclusions

Multiscale modeling of vascular pathophysiology can provide molecular and cellular insights to understand complex biochemical and biophysical mechanisms of the human vascular system. The current gold standard consists of animal *in vivo* models and *in vitro* cell culture, however significant limitations persist in both these approaches. Recent developments in fabrication techniques, such as organ-on-chip and 3D printing, provide a unique solution to mimic human vascular function, thereby increasing the translational potential to humans and decreasing the mechanistic complexity associated with the experimental outputs. However, these emerging approaches are still in proof-of-concept stage and need further optimization to potentially aid in a better understanding of vascular pathophysiology while providing valuable tools for pharmaceutical research and translational outcomes. In order to utilize the full potential of organs-on-a-chip and 3D printing, as well as recapitulate critical aspects of vascular disease development and progression with high precision, the cell sources have to be primary and/or stem-cell derived. Human induced pluripotent stem cells (hiPSC) differentiated into targeted cell-lineages is an exciting new approach that may become the gold standard cell-source in these modeling systems in the future.

Similarly, the physical properties of biomaterials need to be optimized in term of composition, stiffness, anisotropy, and permeability, all which impact vascular pathophysiology and disease development. (**Table 1-4**) In addition, the materials used to fabricate vascular tissues should be able to withstand long-term cell culture for the assessment of disease progression (e.g. from the observation of EC dysfunction to stenosis, and eventually a plaque rupture). Bioinks and scaffold materials that provide structure to organs-on-chips and 3D printed tissues can be enhanced with nanoparticles to improve upon the model's mechanical and biochemical functionality. Also, currently available fabrication techniques produce constructs that are not able to form vascular geometries with anatomical accuracy. Some printers, such as the nanobiological printers, are able to provide resolutions up to 5-20 μm, however it is not evident if these features can be translated to extrusion-based printers using biological relevant, cell-laden bioinks. (135) Considering these geometrical constraints, there is a need for a printer that is able to construct multi-material, hierarchical structures across multiple length scales to mimic native vasculature. This will enable the fabrication of heterogeneous tissue consisting of adventitia, media, and intima layers, all comprised of different cell-laden bioinks. (118, 164)

Table 1-4. Material properties of human vasculature and common vessel models.

Materials	Maximum Stress (MPa)	Maximum Strain	Elastic modulus (Mpa)	Notes	Ref.
Healthy coronary artery	1.44 ± 0.87	0.54 ± 0.25	1.48 ± 0.24	Average age 38.07 ± 8.58; Strain rate of 1 mm/min	(6)

Table 1-4. Continued.

Materials	Maximum Stress (MPa)	Maximum Strain	Elastic modulus (Mpa)	Notes	Ref.
Diseased coronary artery	2.08 ± 0.86	0.35 ± 0.11	3.77 ± 0.38	Average age 65.50 ± 10.33; Strain rate of 1 mm/min	(6)
Layer-specific mechanical properties of coronary arteries	Adventitia: 1.43 ± 0.604 (circumferential) 1.3 ± 0.692 (longitudinal) Media: 0.446 ± 0.194 (circumferential) 0.419 ± 0.188 (longitudinal) Intima: 0.394 ± 0.223 (circumferential) 0.391 ± 0.144 (longitudinal)	Adventitia: 1.66 ± 0.24 (circumferential) 1.87 ± 0.38 (longitudinal) Media: 1.81 ± 0.37 (circumferential) 1.74 ± 0.28 (longitudinal) Intima: 1.6 ± 0.29 (circumferential) 1.55 ± 0.40 (longitudinal)	n.m.	Average age: 71.5 ± 7.3 years old	(165)
Inferior vena cava	n.m.	n.m.	n.m.	Burst Pressure (mm Hg): 13,062 ± 6,847 Compliance: 2.4% ± 0.85%	(116)
Elastin/Collagen	0.5017 ± 0.3665	0.2855 ± 0.1210	Elastin: 0.49 ± 0.18 Collagen: 131 ± 64	Mongrel dogs aged 54.9 ± 8.8 months weighing at 20.4 ± 1.8 kg	(166)
PDMS	5.39 ± 1.23	144 ± 9.3			(167)
PDMS	n.m.	n.m.	0.005 – 1.72	Increasing elastic moduli demonstrates higher surface roughness; Strain ranged from 0 – 10 %	(168)
PDMS	n.m.	n.m.	2.04 ± 0.06 (10:1 PDMS:crosslinker) 0.42 ± 0.05 (30:1 PDMS:crosslinker)	0.1 N load with 0.01 mm displacement resolution; 10% strain applied to each sample at a rate of 0.25 mm s^{-1}	(169)

Table 1-4. Continued.

Materials	Maximum Stress (MPa)	Maximum Strain	Elastic modulus (Mpa)	Notes	Ref.
GelMA, κCA, & nSi (NICE)	0.3017 ± 0.021	70%	Tension: 0.495 ± 0.150 Compression: 0.0711 ± 0.0049	Demonstrated > 75% recovery after cyclic deformation	(113)
GelMA	n.m.	n.m.	0.0005 – 0.001	Strain rate of 0.2 mm min^{-1}	(83)
GelMA	n.m.	n.m.	0.0121 ± 0.0011	Tried to mimic vascularized liver (elastic modulus: 0.0055 ± 0.0016 Mpa)	(109)
Sodium Alginate	0.049 ± 0.005 (2 wt.%) to 0.184 ± 0.008 (4 wt.%)	1.53 ± 0.10 (2 wt.%) to 1.97 ± 0.009 (4 wt.%)		Ramp force with a slope of 0.5 N min^{-1}	(118)
PEGDA (700 MW:8000 MW)	n.m.	20 wt.% PEGDA 700: 0.50 ± 0.15 10 wt.% PEGDA 8000: 1.6 ± 0.1	0.0053 ± 0.0009 (20 wt.% PEGDA 700) to 0.0746 ± 0.0015 (10 wt.% PEGDA 8000)	Loaded quasi-statically at 0.02 mm s^{-1} until failure with strain rate of 0.005 s^{-1}	(117)
PGA and PLCL	n.m.	n.m.	n.m.	Burst Pressure (mmHg): 6,167 ± 5,627 (pre-operative) 13,062 ± 6,847 (6-months postoperative) Compliance: 4.0% ± 1.5% (preoperative) 2.3% ± 0.46% (postoperative)	(116)
PLLA and SPEU-PHD	90/10 Outer-layer with 50/50 Inner-layer PLLA/PHD: 2.07 ± 0.17 (circumferential) 2.56 ± 0.28 (axial)	90/10 Outer-layer with 50/50 Inner-layer PLLA/PHD: 233.17 ± 34.62 (circumferential) 142.14 ± 23.87 (axial)	PLLA: 13.85 ± 3.82; 90/10 PLLA/PHD: 6.30 ± 0.75 50/50 PLLA/PHD: 5.35 ± 0.98 PHS: 0.56 ± 0.27; 90/10 Outer-layer 50/50, Inner-layer PLLA/PHD: 6.24 ± 1.69 (circumferential)	Suture retention and burst pressure was dependent on thickness	(170)

Given the increasing complexity of organ-on-a-chips and 3D printed structures, validation of the model to mimic *in vivo* conditions, such as cell phenotype and remodeling, are needed. Therefore, advanced imaging techniques, computational modeling, and the integration of genomics provide a means to further assess and validate engineered vascular models. Advanced imaging systems with enhanced penetration depth, such as optical coherence tomography (OCT) and photoacoustic tomography (PAT), would permit visualization of the 3D structure and geometrical changes within the model. The use of more mature imaging modalities provides a means to non-invasively probe cell-cell and cell-matrix interactions when cultured within organ-on-a-chip devices and 3D printed models. In addition, emerging approaches also focus on the development of computational tools to model fluid dynamics, oxygen diffusion, cellular proliferation, remodeling, and viability within 3D models. This permits researchers to examine, assess, and optimize models prior to fabrication as well as correlate anticipated results to *in vivo* observations. Furthermore, whole genome transcriptomic approaches can be applied to validate the cell behavior responses and to understand mechanistic pathways. (171)

In summary, the prospects of these emerging technologies are promising. The relationship between design, manufacturing, and assessment are closely related and present a never-ending, repeated cycle. Therefore, this process can be enhanced with bioengineering, material science, medicine, imaging, and genomic collaborations. Bringing these fields together will improve the success of these platforms to predict physiology and responses to drugs, toxins and chemicals on a human patient level. (172) (**Figure 1-5**) As more

progress is made in this direction, organs-on-a-chip and 3D bioprinting technologies are expected to add new knowledge to vascular disease pathophysiology and predict therapeutic responses at disease- and patient-specific levels, which is currently not possible with animal models, thus directly impacting the entire healthcare system.

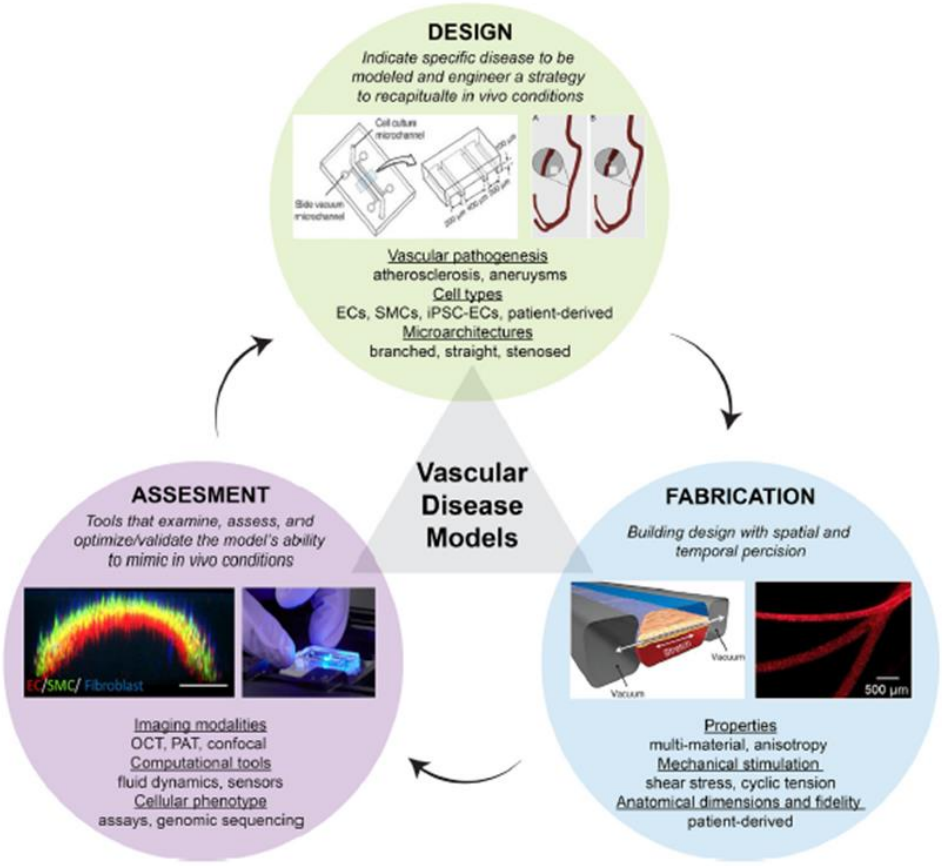

Figure 1- 5 The continuing cycle of model designs, fabrication techniques, and assessments/validations provides an engineered platform to mimic and test vascular physiology, functionalities, and response to drugs and toxins. Adapted and reproduced with permission from (173) © 2013 Nature Protocols (78) © 2017 American Chemical Society (109) © 2017 AIP Publishing (174)© 2015 Nature (164) © 2018 American Chemical Society

2. NANOENGINEERED EXTRACELLULAR MATRIX BIOINKS FOR 3D BIOPRINTED MULTICELLULAR BLOOD VESSELS

Bioprinting is an emerging additive manufacturing technique to fabricate three-dimensional (3D) constructs for human disease modeling applications. However, current bioinks lack sufficient biocompatibility, printability, and structural stability needed to translate this technology to preclinical and clinal trials. Here, we introduce a new class of nanoengineered, hydrogel-based bioinks that can be printed into 3D, anatomically accurate, multicellular blood vessels that recapitulate both the physical and chemical microenvironments native to human vasculature. This bioink demonstrates high printability and capacity to protect encapsulated cells against high shear forces within the extrusion process, regardless of the cell encapsulation densities utilized. Bioprinted cells maintain a healthy phenotype and remain viable for nearly one-month post-fabrication. Leveraging these properties, the nanoengineered bioink is printed into 3D cylindrical blood vessels, consisting of living co-culture between endothelial cells and vascular smooth muscle cells, providing the opportunity to model vascular function and pathophysiology. Upon cytokine stimulation and blood exposure, this bioprinted vessel is able to recapitulate a thromboinflammatory response as observed *in vivo*. Therefore, this bioprinted vessel provides a potential tool to investigate vascular disease pathophysiology and assess therapeutics, toxins, or other chemicals in preclinical trials.

2.1 Introduction

Three dimensional (3D) bioprinting, a subclass of fused deposition modeling or extrusion-based printing, is capable of producing heterogeneous, tissue-shaped constructs in a layer-by-layer fashion with embedded cells, demonstrating enormous promise to recapitulate the native, multi-cellular vascular anatomy. 3D bioprinting has achieved pivotal milestones, including the fabrication of perfusable vascular constructs (175-177), patterned tissues (178, 179), and implantable devices (180, 181). However, 3D bioprinted models that mimic vascular pathophysiology have not yet been demonstrated due to our inability to support long-term co-culture, perfuse blood, and measure critically relevant functional outcomes. This is mostly attributed to the lack of a bioink with high printability, modular mechanical properties, and the ability to both localize and deposit a high density of living cells into 3D architectures. Specifically, hydrogels for direct extrusion are not mechanically resilient for high-fidelity 3D bioprinting. For example, uncrosslinked hydrogels (precursor solutions) are often too fluidic for high-fidelity extrusion of anatomically accurate structures, while crosslinked hydrogels are too brittle to yield through a needle without fracturing. (125) In addition, current bioinks are not able to maintain construct integrity and fidelity while sustaining a high cell viability and phenotypic maintenance. Taken together, limitations of current bioinks restrict the potential to fabricate anatomically accurate, multilayered tissues with the innate ability to replicate human pathophysiological functions.

Here, we address past limitations by introducing a nanoengineered bioink that is bioprinted into 3D models of blood vessels. This approach offers improved spatio-temporal resolution on a macro-structure as well as a tissue- and cell-level micro-structure (i.e. cellular composition, extracellular matrix organization, and physiological communication), achieving what is currently not possible with currently available bioinks. (182) Specifically, we demonstrate that endothelial cells (EC) and vascular smooth muscle cells (VSMC) can be co-cultured into cylindrical vessels utilizing a 3D bioprinting approach. (**Figure 2-1**) To achieve this, we developed a high viscosity colloidal bioink, termed nanoengineered extracellular matrix (nECM), composed of gelatin methacryloyl (GelMA), poly(ethylene glycol) diacrylate (PEGDA), and two-dimensional nanoclay (also known as nanosilicates). This nECM bioink is reinforced by clay-clay and polymer-clay interactions, permitting extrusion of high-fidelity scaffolds that can subsequently be crosslinked *via* ultraviolet (UV) light. The designed nECM bioink enables for the fabrication of free-standing vessels of varying lumen size to accurately reflect upon diverse human vessel geometries. (183-185) Subsequently, we show that this nECM bioink can be used to engineer a 3D vascular model that can accurately predict human thromboinflammation upon cytokine insult. This data lays the foundation for this model to be applied in preclinical settings within vascular medicine, including drug discovery as well as the analysis of various chemicals and toxins.

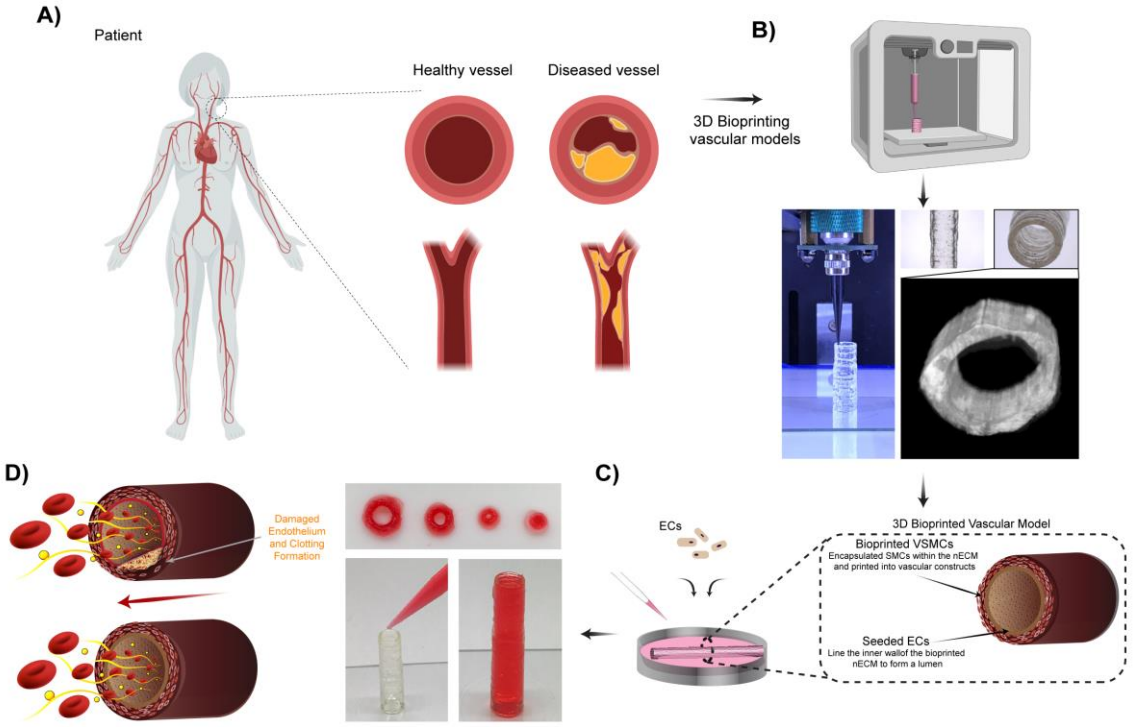

Figure 2- 1 Schematic of the fabrication process to construct 3D vascular models. A) 3D bioprinting can be used to replicate structure and pathophysiological function of healthy and diseased blood vessel. B) Nanoengineered bioinks are developed and characterized with encapsulated vascular smooth muscle cells (VSMCs) for 3D bioprinting of vascular constructs. C) 3D printed scaffolds can be subsequently crosslinked *via* UV light and seeded with endothelial cells (ECs) to form a confluent monolayer, mimicking the intimal layer or lumen of human vessels. D) This fabrication technique permits for the construction of a 3D bioprinted vascular model.

2.2 Experimental Section

2.2.1 Materials and Synthesis

Nanosilicate (Laponite XLG; nSi), acquired from BYK Additive and Instruments, was stored under vacuum to prevent particle interaction with water. Poly(ethylene glycol) diacrylate (PEGDA), with a molecular weight of 0.7, 3.4, 8, or 10 kilodaltons (kDa or

grams per mole (kg/mol)), was purchased from Polysciences Incorporated. Porcine gelatin (Type A, 300 Bloom), methacrylic anhydride, and Irgacure 2959 (2-Hydroxy-4'-(2-hydroxyethoxy)-2-methylpropiophenone) were purchased from Sigma Aldrich. Gelatin methacryloyl (GelMA, 80% methacrylated) was synthetized using procedures previously reported. (113) In short, 10 g of porcine gelatin was dissolved into 100 mL of 1X phosphate buffered saline (PBS). The solution was heated on a stir plate for 1 hour at 65 ˚C to obtain a transparent, homogeneous solution. Following dissolution, 8 mL of methacrylic anhydride was slowly added dropwise over several minutes and allowed to react for 3 hours. To stop the reaction, 400 mL of 1X PBS, heated to 40 ˚C was added to the system and held stable for 15 min. The synthesized solution was then put under dialysis for 7 days, using cellulose membrane dialysis tubing (VWR, 14,000 Da) in 18 MΩ water. The deionized water was changed twice daily, followed by lyophilization.

2.2.2 Bioink Fabrication

Desired volumes of GelMA and PEGDA were dissolved into heated deionized water (40 ˚C) under constant mixing on a stir plate. Once a transparent solution was obtained (~5 min.), 0.03% w/v Irgacure 2959 was added and stirred for an additional 3 min. Nanosilicates were slowly incorporated into the hydrogel precursor solution and mixed until a change in viscosity was observed (~5 min). Bioink formulations were stored overnight at 40 ˚C before use. Subsequent crosslinking of bioink formulations was obtained *via* exposure to UV light at 7 mW/cm^2 for 60 seconds (s). UV duration was determined through assessment of cellular spreading of encapsulated VSMCs after 1 and

7 days of culture when exposed to 7 mW/cm^2 of UV light for 20, 40, 60, or 120 s. (**Figure A-1**)

2.2.3 Physiological Stability

Equilibrium water uptake was calculated by soaking crosslinked hydrogels in water and basal media (RPMI media, ThermoFisher Scientific) for 24-hours in the incubator (37˚C; 5% CO_2; n = 4). The mass of the hydrogel as prepared (T = 0 h) was compared to the mass of the hydrogel after swelling (T = 24 h) and recorded as Q_o (**Equation 2-1**). Water uptake was collected for combinations of GelMA (5, 7.5, and 10 wt.%) and PEG(10k)DA (0, 1, 2.5, and 5 wt.%) as well as GelMA + PEG(10k)DA with altering amounts of nanosilicates (7.5 wt.% GelMA + 2.5 wt.% PEG(10k)DA + 1 – 5 wt.%, nanosilicates ranging in increments of 1 wt.%). This was also collected for different molecular weights of PEGDA (700, 3,400, 8,000, and 10,000 g/mol) in the finalized nECM bioink ratios to understand the range of mechanical properties produced through slight modifications in the hydrogels crosslinking density.

$$Q_o = M_i / M_f \qquad \textbf{(Equation 2-1)}$$

2.2.4 Uniaxial Compression

An ADMET MTEST Quattro eXpert 7600 Single Column Testing System equipped with a 25 lb. load cell was used for uniaxial compression testing. Utilizing a biopsy punch,

hydrogels were casted into 2-mm thick sheets and stamped into 7-mm diameter samples (n = 4). Each sample's diameter and height were measured with a digital caliper and variations of measurements were incorporated into modulus calculations. Unconstrained samples were compressed 20% of the measured height and returned to starting position at a strain rate of 1 mm / min. Raw data for cyclic compression was processed using Excel to calculate the compressive modulus as the slope of the linear region of the data (0 to 20% strain). Compression data was collected for combinations of GelMA (5, 7.5, and 10 wt.%) and PEG(10k)DA (0, 1, 2.5, and 5 wt.%) as well as GelMA, PEG(10k)DA, and varying amounts of nanosilicates (7.5 wt.% GelMA + 2.5 wt.% PEG(10k)DA + 1 – 5 wt.% nanosilicates ranging in increments of 1 wt.%). In addition, compression was also performed on a combination of GelMA (7.5 wt.%), PEGDA (2.5 wt.%), and nanosilicates (4 wt.%) utilizing various molecular weights of PEGDA (700 Da, 3.4 kDa, 8 kDa, and 10 kDa).

2.2.5 Rheological Characterization

Rheological experimentation was performed using a stress-controlled Discovery Hybrid Rheometer 2 (DHR-2, TA Instruments) with a 40-mm diameter, parallel plate geometry attached. The geometry was equilibrated to 37 ˚C and a gap height of 0.25 mm in combination with a solvent trap was used for all experiments. Rotational shear-rate sweeps were performed between 10^{-2} and 10^{4} (s^{-1}) to determine the power-law region and shear behavior. Power-law parameters n (flow behavior index) and K (consistency index) were

calculated utilizing the TRIOS software (TA instruments) and verified using excel. Rotational time sweeps were executed at three consecutive shear rates (s^{-1}): 3.02 (60 s), 23,000 (5 s), and 0.01 (120 s) to characterize the shear recoverability of precursor solutions. Oscillatory stress sweeps were performed between 10^{-1} and 10^{3} (Pa) with a frequency of 1 Hz. Both storage and loss moduli were monitored to measure the material's yield stress. Ultraviolet (UV) crosslinking kinetics were characterized utilizing an oscillatory time sweep with a stress of 1 Pa and frequency of 1 Hz. After 30 s, samples were exposed to UV light (7 mW/cm^2) and the storage modulus observed.

2.2.6 Numerical Modeling

A 3D model of the extruder was fabricated utilizing Solidworks 2018 and imported into ANSYS Spaceclaim (ANSYS 19.2) in order to initiate the computational simulation. Upon importing, a 3D mesh was rendered with 3D linear elements. In whole, the model was formatted as a steady laminar problem. Specifically, material properties were inputted such that the viscosity profile of the bioink followed the power law model. The inlet boundary condition was specified as 4.97×10^{-6} m/s, based off of the volumetric flow rate in which the bioink is printed. All walls within the system were assumed to have no-slip boundary conditions. As the ink was extruded onto the printing bed, the outlet boundary condition was established as 0 Pa (gauge pressure). The problem was then solved for continuity, mass balance, momentum balance and energy balance to model the bioink flow patterns through the 3D extruder**.**

2.2.7 3D Print Fidelity

All printed shapes were designed in Solidworks, exported into STL files, loaded and modified in Slic3r, and exported into G-code instructions for the printer. All printed constructs were programmed to have a layer height of 200 µm and a speed of 0.20 mm/s. When necessary, 4 µL/mL of food coloring was added to aid in visualization of printed constructs. All precursors were stored and printed at 40 ˚C utilizing a 400-µm diameter gauge and an I3 RepRap Printer. To characterize the nECM's bridging ability, a device was fabricated to assess the bioink's ability to deposit over a gap and support itself without any underlying materials. Two metal plates were angled and screwed into a stationary bottom plate, allowing for a varied gap along the x-axis. A rectangular shape of varying infill densities (5 and 10 % infill to ensure visualization of gap distance) was printed over the varied gap distances. In addition, to characterize the fidelity ratio, 2 cm x 2 cm squares were printed at various infill densities (n=3; 0, 5, 10, 20, 30, 40, 50, 60, 70, and 80%) programmed in Slic3r. Infill areas were calculated in ImageJ, utilizing a raster technique to produce an overall average per sample. The print fidelity ratio was quantified as the ratio of the programmed or theoretical void area (A_T) to the actual void area of the print (A_A). (**Equation 2-2**)

$$Fidelity\ Ratio = \frac{A_A}{A_T} \qquad \textbf{(Equation 2-2)}$$

If the fidelity ratio is less than one, voids are smaller than the theoretical area. This is common for hydrogels due to variables such as over-extrusion, pooling, extrudate swell, and/or low print velocities. On the contrary, if the fidelity ratio is greater than 1, the area printed is larger than the theoretical, programmed void, translating to conditions such as air bubbles in the extruder, clogging, dragging, and/or an accelerated printing velocity. Ideally, the fidelity ratio should be equivalent to one, meaning the printed void is equivalent to the theoretical void. The results obtained support the hypothesis that as the infill density is increased, errors are compounding, leading to a logarithmic decease in the fidelity ratio. (**Figure 2-2E**) Due to the nature of this work directed at modeling vasculature, the geometries constructed consist of hollow channels with no infill density. Thus, the printing parameters defined yield an optimal fidelity ratio (~ 1) for the scaffolds being constructed.

2.2.8 *In Vitro* Cell Studies

To evaluate the nECM's ability to maintain vascular cell viability, phenotype, and metabolic activity, human umbilical vein endothelial cells (ECs; Lonza CC-2517) and human umbilical artery smooth muscle cells (VSMCs; Lonza CC-2579) were seeded on 4-mm diameter samples (used between 3 and 10 passages and seeded at a density of 200,000 cells per gel/well). ECs were cultured in EGM-2 medium supplemented with bullet kits (Lonza CC-3156 and CC-4176) and VSMCs in SmGM-2 medium

supplemented with bullet kits (Lonza CC-3181 and CC-4149) in the incubator (37˚C; 5% CO_2; n = 4 per time point and per assay) for 1, 3, and 7 days. Viability was analyzed through a Live-Dead assay. Specifically, cells were stained with a solution of ethidium homodimer (4 µL/mL; Abcam) and calcein AM (2 µL/mL; Abcam) in PBS for 30 minutes, and subsequently rinsed with PBS two times. This was demonstrated for both cell types, demonstrating a high viability (> 80%) as well as an increase in proliferation over days 1, 3, and 7 for all bioink combinations and constituents (GelMA, GelMA + PEGDA, and GelMA + PEGDA with various nanosilicate concentrations – 1 – 4 wt. % nanosilicates). (**Figure A-2**) To assure viable cells were maintaining their proper phenotype on the nECM, cell-specific antibodies were utilized for staining, explicitly vascular endothelial-cadherin (VE-cadherin monoclonal antibody; Invitrogen 36-1900) for ECs and α-smooth muscle actin (α -SMA monoclonal antibody; Invitrogen MA1-26017) for VSMCs. In detail, hydrogels were rinsed with PBS and fixed with 4% paraformaldehyde overnight for each time point. When staining, cell membrane was permeabilized using 0.1 % Triton X-100 in a PBS-bovine serum albumin (BSA) solution (3% BSA) for non-specific antibody binding for 20 minutes. Once permeabilized, gels were rinsed with PBS, exposed to 1:100 ratio of primary antibody to PBS-BSA solution (rabbit anti-VE cadherin polyclonal antibody, ECs; rabbit anti-α SMA polyclonal antibody; 37˚C for 1 hour), washed with PBS, incubated in the same PBS:BSA buffer with 1:500 ratio of secondary antibody to PBS-BSA (goat anti-rabbit conjugated with Alexa Fluor® 568; ; 37˚C for 45 minutes), and rinsed again with PBS. After antibody staining, gels were exposed to 1:2,000 Hoechst® dye solution to stain for cell nuclei (37˚C for 10 minutes). All imaging

was conducted on a Zeiss Axio Observer Z1 Microscope. Images were randomly taken on the surface of 4 replicates, processed in ImageJ, and one representative image presented. In addition to immunohistochemical staining, real-time quantitative reverse transcription polymerase chain reaction (RTq-PCR) was performed ($n \geq 3$). To begin with, cells were seeded on tissue culture polystyrene (TCPS) controls or on bioink samples in non-adherent 6-well plates. After 7 days of culture, cells were trypsinized (3 min. at 37˚C) to remove cells from the gels and pelleted by centrifugation. RNA was isolated and collected *via* a Zymo Research Quick-RNA Miniprep Extraction Kit following the manufacturer's protocol. Initial quality of nucleic material was evaluated using a NanoDrop One/One Microvolume UV-Vis spectrophotometer (ThermoFisher Scientific), assessing the 260/280 absorbance ratios (around 2.0). (**Figure A-3**) Following RNA isolation, cDNA was synthesized *via* SuperScript III Reverse Transcriptase (Thermo Fisher), following manufacturer's protocol. All primers (GAPDH; EC: vascular endothelial cadherin - VE-cadherin, von Willebrand Factor - vWF, and endothelial nitric oxide synthase 3 – eNOS; VSMCs: α-smooth muscle actin – ACTA2, calponin 1 – CNN1, and transgelin – TAGLN) were purchased from Bio-Rad. SYBR Green reagent was then used for amplification quantification using an Applied Biosystems QuantStudio 12K Flex. Expression and fold-change values were calculated from fluorescence and normalization to GAPDH values as well as to TCPS controls utilizing Excel [$\log_2$(TCPS controls/nECM gels)]. Metabolic activity was assessed utilizing an AlamarBlue assay on seeded ECs, seeded VSMCs, encapsulated VSMCs, and printed VSMCs on or within the nECM to ensure metabolic activity of cells was maintained (BioRad). AlamarBlue assays were performed on days 1,

7, 14, 21, and 30. All seeded samples were normalized to TCPS metabolic activity, while encapsulated VSMCs samples were normalized to the metabolic activity of nECM seeded VSMCs and printed VSMCs metabolic activity was normalized to the metabolic activity of nECM encapsulated VSMCs.

2.2.9 3D Bioprinted Vascular Model

All 3D bioprinting was conducted inside of a biosafety cabinet. Specifically, all parts of the printer (i.e. extruder, printer body, needle gauge) was sprayed with ethanol and put under UV sterilization overnight to ensure a sterile environment for 3D bioprinting of VSMCs. To visualize the distribution of encapsulated VSMCs within the nECM bioink, cells were incubated with 5 µM CellTracker Green (Invitrogen) in 1X PBS for 30 minutes prior to passaging, utilizing the manufacturer's protocol. Cells were then trypsinized, pelleted, distributed into 5 µL of media, then added and carefully stirred into the nECM bioink using a small spatula. The bioink was then loaded into the extruder and printed into hollow cylinders with a two-layer perimeter (5 mm tall, 10 mm diameter, ~ 1 mm wall thickness). After printing, constructs were crosslinked with UV-light and placed into well with the scaffold laying on its side. After 24-hours of VSMC encapsulation, one T75 flask of ECs were exposed to 5 µM CellTracker Red (Invitrogen) in 1X PBS for 30 minutes prior to passaging. ECs were then passaged, seeded on the bottom half of the printed inner channel, and cultured in 50:50 SmGM-2 to EGM-2 media for 6 hours. The 50:50 EC:VSMC media ratio utilized was determined through assessment of cellular metabolic activity on days 1, 3, and 7. (**Figure A-4**) After 6 hours, constructs were flipped 180˚ along

the z-axis and EC seeding repeated on the other half of the hollow construct (T75-flask of ECs stained with CellTracker Red seeded within the hollow channel). VSMCs and ECs were cultured for 3 days and images were randomly taken on 5 replicates utilizing a Zeiss LSM 780 NLO Multiphoton Microscope after 48 hours of culture in 50:50 EC:VSMC medium. Images were processed in ImageJ, presenting one representative image.

2.2.10 Validation of 3D Bioprinted Vascular Model

To validate the use of the nECM 3D bioprinted vascular model, clotting experiments were performed and analyzed with clinically relevant techniques, utilizing protocols previously established. (134, 186) First, nECM and nECM constituents were prepared, crosslinked, punched into 6 mm dimeter biopsies, and placed into 96 well plates (n = 5). Samples were then exposed to coagulation-activated blood (10 µL of 0.1 M calcium chloride ($CaCl_2$) and 100 µL of bovine blood containing sodium citrate) at 37℃ for a pre-defined duration of time (varying between 1 and 7 min.; increments of 1 min.). After the specified duration of time, any uncoagulated supernatant was removed and the sample washed three times with 1X PBS, leaving any clotted blood. This process was repeated on endothelialized nECM constructs cultured for 7 days as well as endothelialized constructs with damaged barrier function. Samples containing ECs with were exposed to human tumor necrosis factor alpha (TNF-α, Sigma - T6674; 5 ng/mL and 10 ng/mL in EGM-2 medium) for 18-hours to disrupt barrier function. After TNF-α treatment, samples were washed two times with 1X PBS and exposed to coagulation-activated blood, as described above. Clotting experiments were also performed on encapsulated VSMCs in the nECM bioink with and

without TNF-α stimulation using the same protocol established for ECs. EC-VSMC co-culture was also performed and clotting assessed after 7 days of culture in 50:50 EC:SMC medium. Samples were then imaged with a Zeiss SteRIO Discovery v8 stereomicroscope and the percent of clotting coverage quantified in ImageJ through characterization of the grey value. Explicitly, clotting of the TCPS control after 7 minutes of activated blood exposure demonstrated full clotting coverage of the well plate surface. This surface was imaged and the grey value calculated on ImageJ. Subsequently, the grey value for all other variables before and after 7 minutes of clotting was calculated in ImageJ. Utilizing **Equation 2-3**, the percentage of clotting coverage was calculated from these results:

$$Clotting\ Coverage = \left(\frac{|Clotted\ Grey\ Value - Sample\ Grey\ Value|}{Sample\ Grey\ Value\ before\ clotting}\right) \times 100 \qquad \textbf{(Equation 2-3)}$$

Utilizing Optical Coherence Tomography (OCT), 3D printed nECM constructs with and without lumen formation were fabricated utilizing the same technique previously described (n = 3). After 7 days of EC culture, for those with lumen formation, samples were washed with 1X PBS and exposed to coagulation-activated blood at 37℃ for 7 minutes. After 7 minutes, samples were carefully washed three times with 1X PBS and imaged with a benchtop OCT system. Image reconstruction and 3D rendering were performed using MATLAB and percent obstruction calculated by measuring the pre- and post-stenosed inner diameters. Lastly, cytokine markers were assessed by collecting media effluents after 7 days of the respective culture (EC monoculture, stimulated EC

monoculture, VSMC monoculture, stimulated VSMC monoculture, EC-VSMC co-culture, and stimulated EC-VSMC co-culture). Effluents were analyzed for specific cytokines using MILLIPLEX® MAP Human cytokine/chemokine magnetic bead panel kit containing the beads tagged with specific antibodies against the target cytokines and performed using the manufacturer's protocol.

2.2.11 Statistical Analysis

All results are expressed as the mean ± deviation ($n = 3 – 5$). Statistical analysis of all quantitative data was performed *via* one-way ANOVA with posthoc Tukey analysis using GraphPad Prism (v 6.01). Statistical significance is demonstrated as * = $p < 0.05$, ** = $p < 0.01$, *** = $p < 0.001$, and **** = $p < 0.0001$.

2.3 Designing and Characterizing nECM Bioink

For extrusion-based additive manufacturing techniques, precursor solutions must flow through a needle and maintain a deposited shape to fabricate programmed geometries that accurately recapitulate the human anatomy. Shear-thinning precursors, also referred to as pseudoplastic or thixotropic, possess non-Newtonian behavior where the solution demonstrates a high viscosity at low-shear rates and linearly decreases upon the external application of a force. (187-189) This behavior is vital for 3D printing applications as it depicts the ability of a bioink to be extruded through the printing gauge (low-viscosity at high shear), but maintain its deposited shape on the printer bed (high-viscosity at low-shear). The incorporation of nanosilicates to polymeric precursor solutions, such as

GelMA-PEGDA, serves as a rheological modifier due to the particle's ability to control interactions in a concentration-dependent manner. (190-193) Nanosilicates ($Na^{+}_{0.7}[(Si_8Mg_{55}Li_{0.3})O_{20}(OH)_4]^{-0.7}$; nSi) are a two-dimensional, trioctahedral, smectite clay nanoparticles (20-50 nm diameter; 1 – 2 nm thickness) with a dual charge distribution (negative surface charge on the particle's face, due to the presence of oxygen, and a positive edge charge, due to cleaved Mg^{2+} and Li^{2+} in aqueous environments). This anisotropic charge distribution facilitates interactions between the edge of one nanoparticle and the face of another (formation of a "house-of-cards" structure). Upon the applications of a shear-force, this "house-of-cards" structure is easily disrupted and rapidly reformed upon removal of external forces, motivating its use as a rheological additive. (194, 195) Aside from particle-particle interactions, nanosilicate-polymer interactions also occur through hydrogen bonding, ionic interactions, and electrostatic interactions. (191, 192, 196) For example, charged groups present on polymer backbones, such as GelMA, may interact with the opposite surface/edge charge of the nanosilicate *via* electrostatic interactions. (197, 198) Additionally, the hydrogen's from the ethylene carbons of PEGDA chains have also been shown to absorb and desorb onto the nanosilicate surface. (199-203) Thus, the unique interactions between nanosilicate particles, nanosilicate-GelMA, and nanosilicate-PEGDA make this combination an ideal nanocomposite to reinforce hydrogel networks and provide rheological substance to the nano-colloidal precursor solutions for 3D printing applications. To derive and optimize an ideal bioink composition for 3D bioprinting, the interactions between individual constituents and their components were investigated.

2.3.1 GelMA and PEGDA Composite Formulation

3D printing provides a means to construct intricate geometries, commonly observed in the vascular system, with high precision and fidelity. However, due to hydrogel's increased susceptibility to absorb more than 80% of its dry weight in water, geometrical accuracy and mechanical stability can be diminished. (204, 205) To design a bioink with limited dimensional and mechanical modifications, we evaluated the fluid-uptake and compressive moduli of GelMA and GelMA-PEGDA composites. GelMA concentrations ranged between 5 and 10 wt.% (increments of 2.5 wt.%), whereas the addition of PEGDA to the matrix ranged between 1 and 5 wt.% (increments of 1 wt.%). Results obtained suggest that the addition of PEGDA, as well as an increase in PEGDA concentration, increased the overall fluid-uptake within the network. (**Figure 2-2A**) However, as the GelMA content was increased, the opposite relationship was presented. Specifically, ratios containing 5 wt.% GelMA demonstrated an overall larger fluid-uptake compared to ratios containing 10 wt.% GelMA. This is hypothesized to be due to an increase in polymeric density, leading to more polymer-polymer entanglements to reinforce and prevent fluid infiltration in the network. Furthermore, water-swollen hydrogels demonstrated a decreased fluid-uptake compared to those swollen in media. This is hypothesized to be due to the inclusion of salts within the media attributing to the measured mass.

Although fluid-uptake can be a direct measure of geometric deviations, the compressive moduli of GelMA and GelMA-PEGDA composites were also collected to assess the overall impact these deviations have on the intended scaffold properties. The compressive moduli of the hydrogels were evaluated immediately after crosslinking (T = 0) and post-swelling in medium for 24 hours (T = 24). (**Figure 2-2B**) When comparing times points, swollen networks maintained a lower modulus compared to samples tested immediately after crosslinking. This is hypothesized to be due to an increase in fluid-uptake, causing chain disentanglements and network expansion, thus requiring less mechanical strain to compress the swollen network due to an increase in chain mobility. Furthermore, as the overall polymeric mass (overall wt.%) increased, the compressive moduli of the network increased as well, correlating to fluid-uptake results. Specifically, as the polymeric mass increased, the fluid-uptake decreased due to additional, stronger interactions reinforcing the polymeric networks.

The consequences of fluid uptake are also illustrated through the characterization of GelMA-PEGDA degradation. (**Figure 2-2C**) As the concentration of collagenase (unity per milliliter; U/mL) was increased, the degradation kinetics also increased. In addition, the presence of 5 wt.% PEGDA forms a stable PEG network, which does not degrade enzymatically, thus no mass loss was observed. Furthermore, the addition of 2.5 and 1 wt. % PEGDA increases the swelling of the overall construct, causing increased adsorption of

the enzymatic solution. We hypothesize that this increases the penetration of collagenase, increasing the degradation profile compared to GelMA controls.

Collectively from these results, 7.5 wt.% GelMA and 2.5 wt.% PEGDA demonstrated a relatively low fluid-uptake and no significant difference between pre- and post-swelling compressive moduli. In addition, the high concentrations of GelMA within this ratio is hypothesized to support improved cell viability and phenotypic maintenance of vascular cells for future studies. The addition of 2.5 wt.% PEGDA, compared to other concentrations tested, supported the network's stability and enables future mechanical modulation while still allowing for enhanced tissue remodeling. Therefore, the ratio of 7.5 wt.% GelMA and 2.5 wt.% PEGDA was considered optimal and used in all future studies.

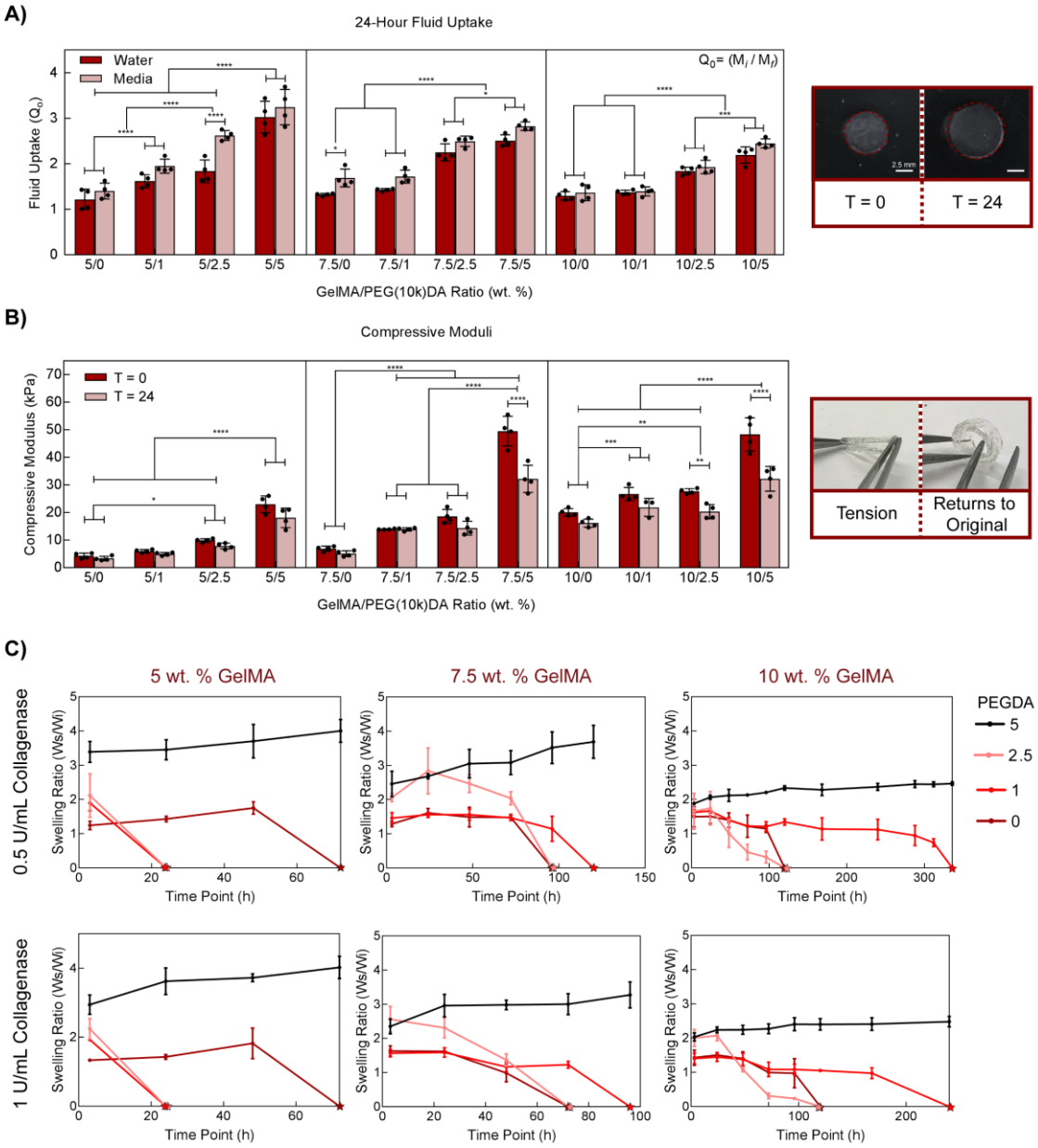

Figure 2- 2 GelMA and PEGDA ratio determination. A) Fluid-uptake of GelMA-PEGDA composite hydrogels in medium and water. Photographs on the right depict the diminished geometrical accuracy over a 24-hour period. B) Compressive moduli were determined immediately after hydrogel fabrication (T = 0) and after 24 hours swelling in medium (T = 24). C) Degradation kinetics were also monitored through mass loss at various concentrations of collagenase.

2.3.2 Nanocomposite Ratio Formulation

To determine the optimum nanosilicate concentration for this nanocolloidal bioink, fluid-uptake and compressive moduli were performed for various concentrations of nanosilicates. (**Figure 2-3A**) At high concentrations (> 2 wt.% nanosilicates), nanosilicates swollen in medium are able to form an internal "house-of-cards" structure that limits liquid absorption into the polymeric network. On the contrary, when nanocomposites are swollen in water, sodium ions dissociate from the surface of the nanosilicates, increasing fluid-uptake. This is hypothesized to be due to the influence of monovalent and divalent cations on the internal nanosilicates structure. Explicitly, in water nanosilicates have a predominately negative charge. However, once the nanocomposite is subjected to a solution containing ions or proteins, such as medium, nanosilicate flocculation near the gel-solution interface occurs, driven by the formation of an electron double layer and electrostatic interactions. Overall, the formed double layer behaves as a protective shield, preventing significant fluid-uptake and therefore geometrical alterations. Separately, the addition of nanosilicates to GelMA-PEGDA also significantly increased the overall compressive moduli compared to composites in the absence of nanosilicates. However, similar to the trend presented in GelMA-PEGDA composites, as the concentration of nanosilicates, or the overall weight percent in the matrix is increased, the compressive moduli continued to increase in a concentration-dependent manner. (**Figure 2-3A**)

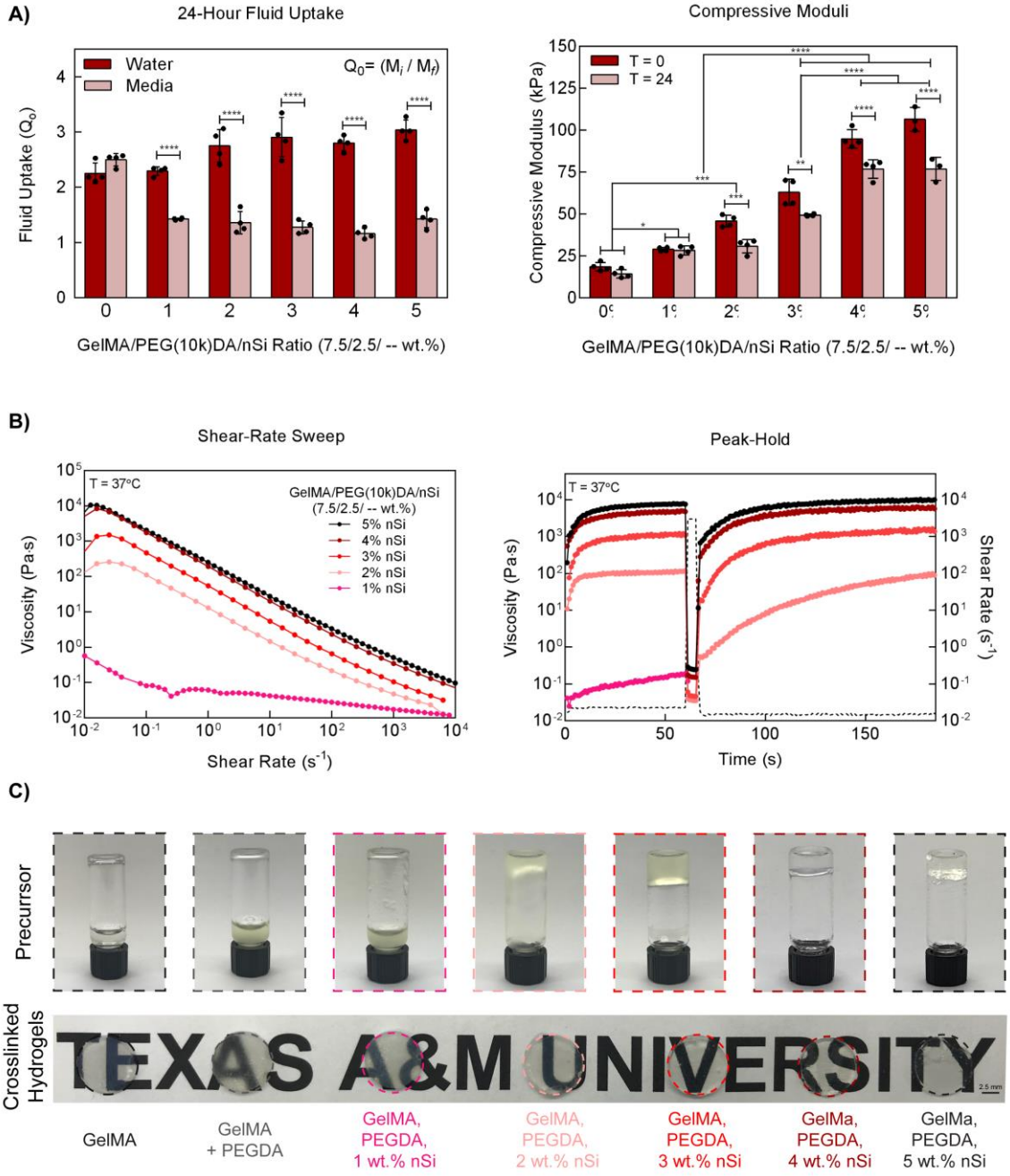

Figure 2- 3 Ratio determination for nanosilicates. A) In order to determine the optimum nanosilicate concentration, fluid-uptake and compressive moduli were performed for various concentrations of nanosilicates. B) Rheological analysis, specifically shear-rate sweeps and peak-hold analysis, of nanosilicate precursor solutions illustrated a concentration-dependent trend. C) Inverted vials display the ability of different ratios to resist gravitational pull, correlating to precursor viscosities. Upon crosslinking, particle, polymer, and polymer-particle interactions can be visualized through hydrogel transparency over the words "Texas A&M University."

Although governing geometrical variations are vitally important to maintain intended, programmed geometries, the ability of a material to be extruded through a needle and maintain a deposited shape licenses a precursor solution to be used as an ink for 3D bioprinting. Thus, the incorporation of nanosilicates to precursors, such as GelMA-PEGDA, can serve as a rheological modifier due to the particle's ability to control interactions and order in a concentration-dependent manner.(190-193) Specifically, the addition of nanosilicates to GelMA-PEGDA composites results in precursor solutions ranging from low viscosity to highly ordered colloidal gels. (191) To evaluate which concentration of nanosilicates is optimal for 3D printing, shear-rate sweep and peak-hold analyses were performed. (**Figure 2-3B**)

Shear-thinning precursors possess non-Newtonian behavior where the solution demonstrates a high viscosity at low-shear rates and linearly decreases upon the external application of a force. (187-189) Shear-thinning materials are vital for 3D printing applications as it depicts the ability of an ink to be extruded through the printing gauge (low-viscosity at high shear), but maintain its deposited shape on the printer bed (high-viscosity at low-shear). To characterize the ability of the nanocomposite to shear-thin, rotational shear-rate sweeps were conducted on GelMA-PEGDA composites with the incorporation of nanosilicates (1 – 5 wt.%). All ratios presented a shear-thinning behavior, with an overall increase in the low-shear viscosity as the particle concentration increased.

For example, the addition of 2 wt.% nanosilicates to GelMA-PEGDA presented a low-shear viscosity around 10^2, whereas 5 wt.% nanosilicates presented a low-shear viscosity around 10^4. This is hypothesized to be due to a more densely packed "house-of-cards" (edge-to-face orientation) structure with increasing concentration of nanosilicates. (190, 192, 206, 207)

Although precursors must first exhibit shear-thinning (transition from a high-viscous gel to a low-viscosity fluid), inks must also rapidly rebuild their internal structure and recovery into a gel state once withdrawn from the printing gauge. This recovery is essential to localize deposited filaments and limit lateral spreading or pooling on the printer bed. To assess this recoverability, peak-hold analysis was performed, observing a material's change in viscosity with a change in shear rate. Overall, the incorporation of nanosilicates greater than or equal to 2 wt.% portrayed a rapid decrease in viscosity upon the application of a high shear rate (2985 s^{-1}), described by the easy disruption of nanosilicate electrostatic interactions. Alleviating the high shear-stress, the nanocomposites were able to return back to a high viscosity. However, with increasing concentrations of nanosilicates, the time required for full recovery is decreased. Specifically, the ratio containing 2 wt.% nanosilicates required more time to recover close to its pre-sheared viscosity compared to 5 wt.%. This is hypothesized to be due to an incomplete disruption of the internal "house-of-cards" structure. Furthermore, solutions containing higher nanosilicate concentrations (> 3 wt.%) have larger areas of polymer-clay interactions and thus recover at faster rates

due to rapid agglomeration. In contrast, the composite with 1 wt.% nanosilicates did not exhibit any recoverability due to the lack of an internal structure. This is hypothesized to be due to no "house-of-cards" structure formation, leading to a Newtonian fluid that is not able to recover.

To visualize the rheological implications of nanosilicates ratios within the GelMA-PEGDA composite, samples were prepared in vials, allowed to exfoliate for 24-hours (form internal structure), and inverted. (**Figure 2-3C**) Once positioned upside-down, GelMA, GelMA-PEGDA, and GelMA-PEGDA-1 wt.% nanosilicates fell to the cap, demonstrating a lack of an internal structure and viscosity upon minimal forces, such as gravitational pull. The GelMA-PEGDA composite with 2 wt.% nanosilicates remained at the bottom of the inverted vial, however started to drip down the sides of the vial. Ratios containing $\geq$ 3 wt.% nanosilicates remained entirely at the bottom of the inverted vial, demonstrating the precursors' high viscosity. In addition, to depict the interactions between particles and nanosilicate-polymeric constituents, crosslinked hydrogels were placed over the words "Texas A&M University," portraying the gels transparency. The GelMA and GelMA-PEGDA composite was slightly opaque and difficult to see through, supporting a more crystalline structure. Upon the addition of nanosilicates (1 – 5 wt.%), the gels become more transparent, representing a more amorphous structure.

Taken together, these results indicate a needed balance between limited geometrical modifications (fluid-uptake), capacity to shear-thin, and rapid recoverability for extrusion-based 3D printing techniques. Specific to scaffold geometry, fluid-uptake of scaffolds is restricted upon the incorporation of nanosilicates, therefore limiting loss of construct accuracy post-printing. However, it is important to note the change in compressive moduli with increasing nanosilicate concentrations. Due to the limited fluid-uptake being insignificant across all ratios, rheological findings took prominence. In the shear-rate sweep, 1 wt.% nanosilicates did not exhibit a strong shear-thinning profile or any recoverability, thus wt.% is not suitable for 3D printing. When assessing the peak-hold analysis, 2 and 3 wt.% nanosilicates did not portray a fast recovery time compared to higher ratios. Such a profile would translate to lateral filament spreading and geometrical compromises. For ease of precursor manipulation during the printing process, 4 wt.% nanosilicates was considered optimal. Therefore, a ratio of 7.5 wt.% GelMA, 2.5 wt.% PEGDA, and 4 wt.% nanosilicates, was considered an optimal bioink for 3D bioprinting. When combined, this ratio is referred to as the nanoengineered extracellular matrix (nECM) bioink, symbolizing a synthetic alternative to the ECM embedded SMCs within the medial layer of human vessels.

2.3.3 PEGDA Molecular Weight Determination

Vascular stiffness has been shown to directly alter cell phenotype and cytoskeletal architectures. (208, 209) Given the composition of the nECM, mechanical properties of

the matrix can be modified without changing chemical constituents. More precisely, the molecular weight of PEGDA can be modulated, altering the matrix's mesh size and therefore constructing a stiffer network. To determine the molecular weight of PEGDA to utilize within the nECM bioink, various molecular weights were analyzed, specifically characterizing a molecular weight of 700 g/mol, 3,400 g/mol, 8,000 g/mol, and 10,000 g/mol within the nECM bioink formulation. (**Figure 2-4**)

The elastic moduli and swelling ratios quantified for PEGDA molecular weights suggest unique interactions between polymeric constituents and nanosilicates. (**Figure 2-4A**) It was first hypothesized with an increase in PEGDA molecular weight, the nECM bioink would demonstrate a decrease in the compressive moduli. However, this was not supported by the data collected. Explicitly, a molecular weight of 8,000 g/mol increased the matrix elasticity compared to lower molecular weights (700 and 3,400 g/mol). Previous literature has reported possible polymeric bridging of nanosilicates, storing accumulated strain that is then released as elastic recovery. (125, 210-212) Moreover, the swelling ratio conducted in water demonstrated an increasing trend as the molecular weight was increased. This supports an increasing mesh size with an increasing molecular weight, permitting more water to infiltrate the hydrogel network. This is further supported by the illustrations to the right of the graph, depicting changes in hydrogel diameter as the PEGDA molecular weight is altered. However, when measured in medium, electrostatic interactions from the nanosilicates limit network swelling. This is shown by the lack of a

significant difference in measured ratios as well as the absence of geometrical changes in hydrogel geometries as the molecular weight is modified.

Additionally, the rheological profiles for each molecular weight was characterized to ensure shear thinning and recoverable characteristics. (**Figure 2-4B**) All molecular weights demonstrated a shear-thinning, thixotropic behavior. Nevertheless, as the molecular weight was increased, the zero-rate viscosity and consistency index increased. This is hypothesized to be due to increased chain entanglements with higher molecular weights and the difficulty to untangle these interactions upon the application of low-shear. Furthermore, the thixotropic behavior of the nanoengineered network decreased with decreasing PEGDA molecular weight. Compared to the pre-sheared region, the lowest molecular weight assessed (700 g/mol) was not able to recover to the original pre-sheared viscosity. Yet, the observed recoverability did increase as the molecular weight of the PEGDA was increased.

From these results, an optimal molecular weight of 10,000 kDa was chosen and utilized in the nECM bioink for all future studies due to its superior low-shear viscosity and recovery characteristics permitting for high-fidelity printing.

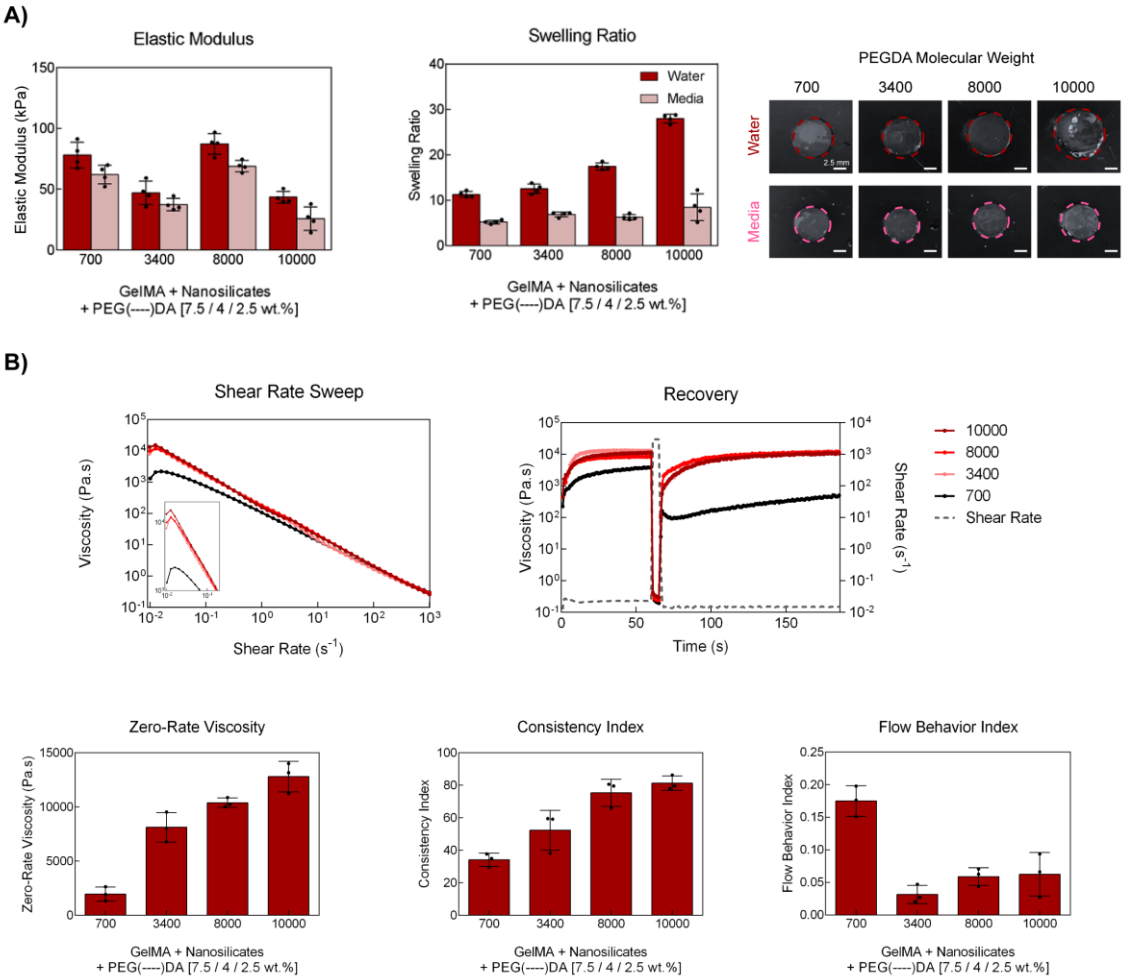

Figure 2- 4 PEGDA ratio determination. A) the molecular weight decreased, hydrogels exhibited a stiffer network and a decrease in the fluid-uptake. B) All molecular weights demonstrated a shear thinning behavior ($n < 1$) and recoverable characteristics.

2.4 Designing Bioinks with High Printability and Print Fidelity

Bioinks for 3D bioprinting must flow through a needle (printability) and maintain a deposited shape (print fidelity) to fabricate constructs with complex geometries. In order to demonstrate and decipher the origin of shear-thinning behavior within the nECM bioink, shear rate sweeps were performed. (**Figure 2-5A**) The GelMA and PEGDA

profiles demonstrated similar behavior, portraying constant viscosity (~ 0.02 Pa•s), independent of the shear-rate being applied. Alternatively, the nanosilicates and nECM composite demonstrated comparable shear-thinning behavior, supporting our theory that nanosilicates are the origin of thixotropic behavior within the bioink. Explicitly, as the shear-rate is increased, the viscosity linearly decreases due to breaking of the nanosilicates particle-particle interactions into smaller fragments that freely move within a fluidized carrier. (213) The generalized Power-Law Model was utilized (p = 0.9) to characterize interactions (polymer, polymer-nanosilicate, and nanosilicate- nanosilicate) and the degree of shear-thinning exhibited by the precursor solutions. (**Equation 2-4**) Particle interactions are reflected through quantification of the consistency index (K) or the viscosity at a shear rate of 1 s^{-1}. Upon fitting the rheological profiles to the power-law equation, an increase in K was observed upon the addition of nanosilicate. This is hypothesized to be due to a close-packed house-of-cards structure, where repulsion forces are balanced with attractive forces, thus resulting in an overall increase in viscosity. The degree of shear-thinning is illustrated through the flow behavior index (n). Specifically, when n = 1, the solution is Newtonian, n < 1 shear-thinning, and n > 1 shear thickening. GelMA (n = 1.04) and PEGDA (n = 1.05) presented Newtonian behavior at 37°C. Upon the addition of nanosilicate, there was a significant decrease in n, suggesting nanosilicates (n = 0.05) is the foundation of shear-thinning behavior within the nECM (n = 0.16). With increasing shear-rate, nanosilicates begin to orient parallel to the direction of flow due to an imbalance between van der Waals and electrostatic forces, thus decreasing the value of n. (212) It is suggested that due to the parallel orientation of nanosilicates during flow, the

charged particles repel each other, therefore gliding over each other to produce a shear thinning fluid.

$$\tau = K\dot{\gamma}^n$$ (**Equation 2-4**)

The effect of addition of nanosilicates to the nECM constituents was also monitored utilizing stress sweeps to determine the yield stress. Storage (G') and loss moduli (G") were assessed at different shear stresses and the cross-over points (yield stress) are represented by the dashed line. All Newtonian fluids demonstrated a consistent storage and loss modulus. However, upon the addition of nanosilicates to GelMA, PEGDA, and their combination, a significant increase to the storage and loss moduli at stresses below 1 Pa was observed. In addition, upon the incorporation of nanosilicates, a yield stress was able to be delineated, illustrating the material is able to flow upon the application of a stress greater than or equal to 102 Pa.

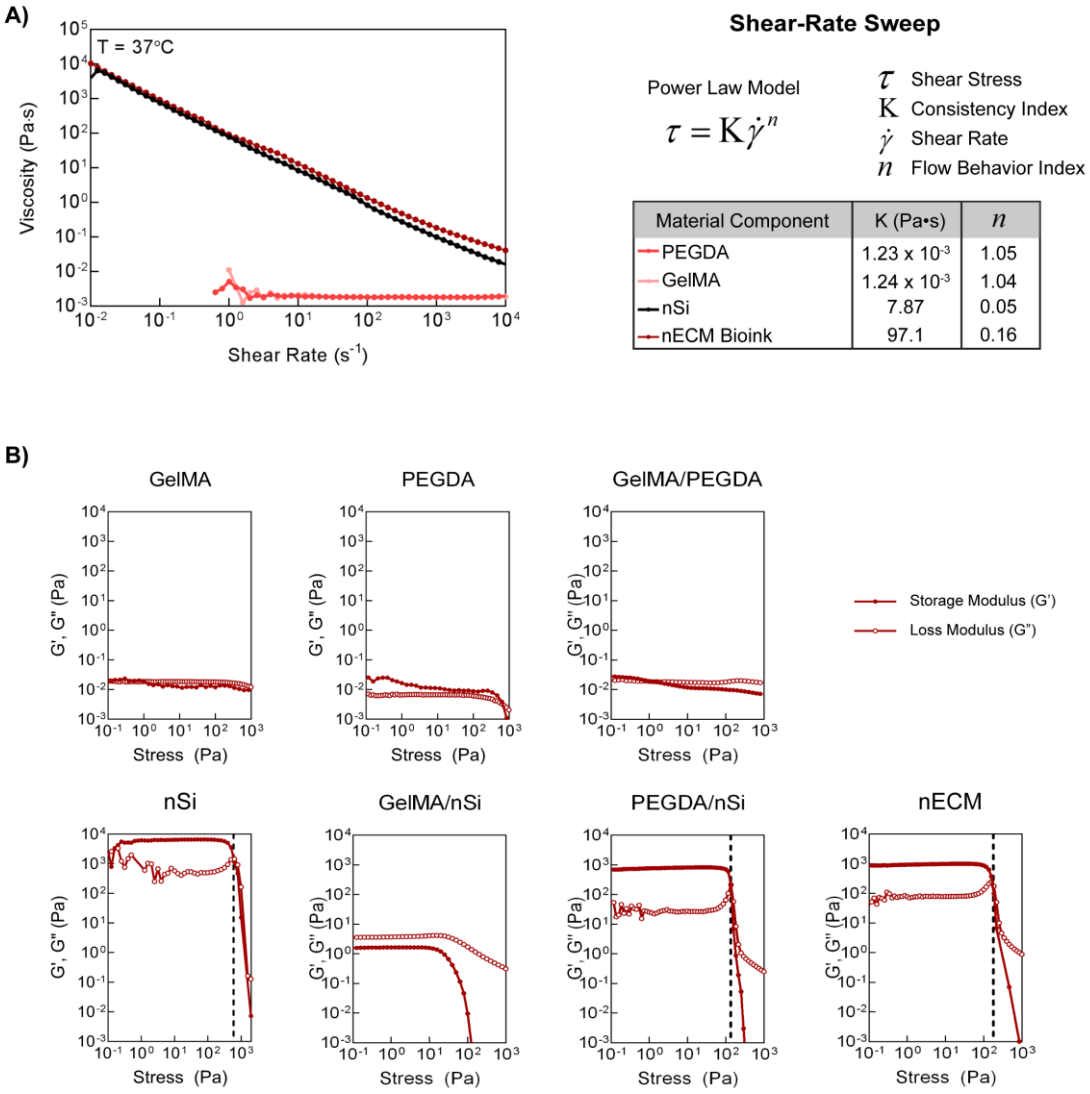

Figure 2- 5 nECM bioink rheological characterization. A) A shear-rate sweep of GelMA, PEGDA, nSi, and nECM bioink precursor solutions was performed to characterize the type of fluid the materials exhibited. When modeling the fluids with the Power-Law equation, the consistency index increases and the flow behavior index decreases upon the addition of nSi. However, GelMA and PEGDA demonstrated a flow behavior index around 1, demonstrating Newtonian-like behavior. B) The effect of nanosilicates addition to the nECM constituents was monitored utilizing stress sweeps to determine the yield stress.

To assess for recoverability, we have designed a peak-hold analysis to monitor the change in viscosity of bioink as it transitions through different stages in the printing process. **(Figure 2-6A)** To do this, constants defined from the Power-Law Model were applied as an input within the Rabinowitsch equation (**Equation 2-5**), where *Q* is the volumetric flow rate and *R* is the radius to which the material is confined (i.e. extruder, needle gauge, printer bed), and *n* is the flow behavior index (defined in Equation 2-4). Bioinks were first exposed to a low-shear rate (3.02 s^{-1}), resembling the shear being within the extruder. After one minute, samples were exposed to high-shear rates (23,000 s^{-1}) for 10 s, depicting the needle gauge, followed by a low-shear rate (0.01 s^{-1}) for 2 minutes, representing the shear experienced on the printer-bed after deposition. The results support the Newtonian nature of GelMA and PEGDA, limiting their use for 3D printing. However, the shear-thinning behavior exhibited upon the addition of nanosilicates to GelMA-PEGDA composites allows for rapid rebuilding of the internal structure within the bioink, permitting for shape retention of the extrudate on the printing bed.

$$\dot{\gamma} = \frac{3n+1}{4n} + \frac{4Q}{\pi R^3} \qquad \textbf{(Equation 2-5)}$$

These shear-thinning and recoverable properties exhibited by the nECM bioink are hypothesized to shield encapsulated cells from damaging shear stresses during extrusion. (203, 214, 215) Utilizing the Power-Law Model constants, ANSYS fluidic modeling was used to predict the wall shear stress within different regions of the extruder (barrel,

connector, and needle gauge). (**Figure 2-6B**) The velocity profile at the printing gauge exhibits a plug-like flow, demonstrating material extrusion first from the center of the gauge and subsequently outwards. It is hypothesized that this velocity profile provides protection to encapsulated cells, shielding them from damaging shear stresses. To validate these results, stress-sweeps were performed to calculate the stress required to cause yielding of the material through the extruder. (**Figure 2-6C**) The results obtained confirm the ANSYS model recapitulates the stresses exposed to the nECM during the printing process. Specifically, the stresses exhibited in the ANSYS model (4208 Pa) exceeded those measured in the stress sweeps (178 Pa), demonstrating at these regions of the extruder, the material yields through the gauge and is deposited. In addition, the stress-sweeps performed demonstrates the addition of nanosilicates increases the yield stress needed for extrusion. (**Figure 2-5B**) For example, the Newtonian nature of the GelMA, PEGDA, and GelMA-PEGDA solutions causes negligible yield stresses, limiting control over the extruded volume. However, solutions with nanosilicates exhibit higher yield stresses, thus providing more control over the volume being deposited and therefore improving print fidelity of bioink.

The flow behavior described above demonstrates the ability of the bioink to be extruded, however to fabricate intricate geometries, such as a blood vessel, bioinks must be able to support deposition of subsequent layers without compromising the shape. Thus, bioinks must be able to bridge over gaps without support material present. When printing GelMA,

PEGDA, and GelMA-PEGDA across a gap of varying lengths, the material pools along the surface, demonstrating the lack of any shape retention. However, upon addition of nanosilicates, the nECM bioink is able to bridge a gap up to 5 mm in distance, illustrating the potential of the nECM to print complex. (**Figure 2-6D**)

Although self-support is essential to produce anatomically accurate vasculature, bridging needs to be taken into consideration along with line fidelity and infill densities. Currently, print fidelity is most commonly characterized through straight-lines, comparing the measured thickness of the line with the needle gauge diameter and printing parameters.(131, 216, 217) However, physiological structures do not exist in straight geometries, consequently multiple parameters, such as bridging, line deposition, and infill densities should be holistically characterized together. This can be accounted for through fidelity ratio quantification, defined as the ratio of the programmed or theoretical void area (A_T) to the actual void area of the print (A_A) (see method section for details). The results show high print fidelity ratio ($A_A/A_T > 0.8$) for low infill densities, which is utilized to print hollow geometries, such as vascular models. (**Figure 2-6E**) With an increased infill density, the print fidelity ratio decreases.

Post-printing, the nECM bioink is cross-linked *via* exposure to UV light, locking the structure into the deposited shape through covalent bonds between the acrylate groups on the PEGDA and GelMA. To verify nanosilicates do not impede this bonding and that

printing stresses do not disrupt the polymer's chemical structures, a time sweep was performed, measuring the storage modulus upon UV exposure after 30 s. (**Figure 2-6F**) All materials containing GelMA, PEGDA, or their combination exhibited an increase in the storage modulus after exposure to UV light. This increase corresponds to a rise in the material's elastic response, therefore supporting the occurrence of crosslinking. However, as expected, nanosilicates independently did not illustrate any change in the storage modulus, translating to no crosslinking. Thus, nanosilicates can be extruded and printed into complex shapes, but cannot be fixed into a stable construct that can be manipulated. However, when combined in the nECM, nanosilicates provide necessary rheological properties to deposit bioinks into complex geometries, while subsequent crosslinking of GelMA and PEGDA provide mechanical stability under physiological conditions. (**Figure 2-6G**) Overall, this nECM bioink permits direct extrusion of mechanically resilient, shear-thinning, and recoverable bioinks for the deposition of high-fidelity constructs.

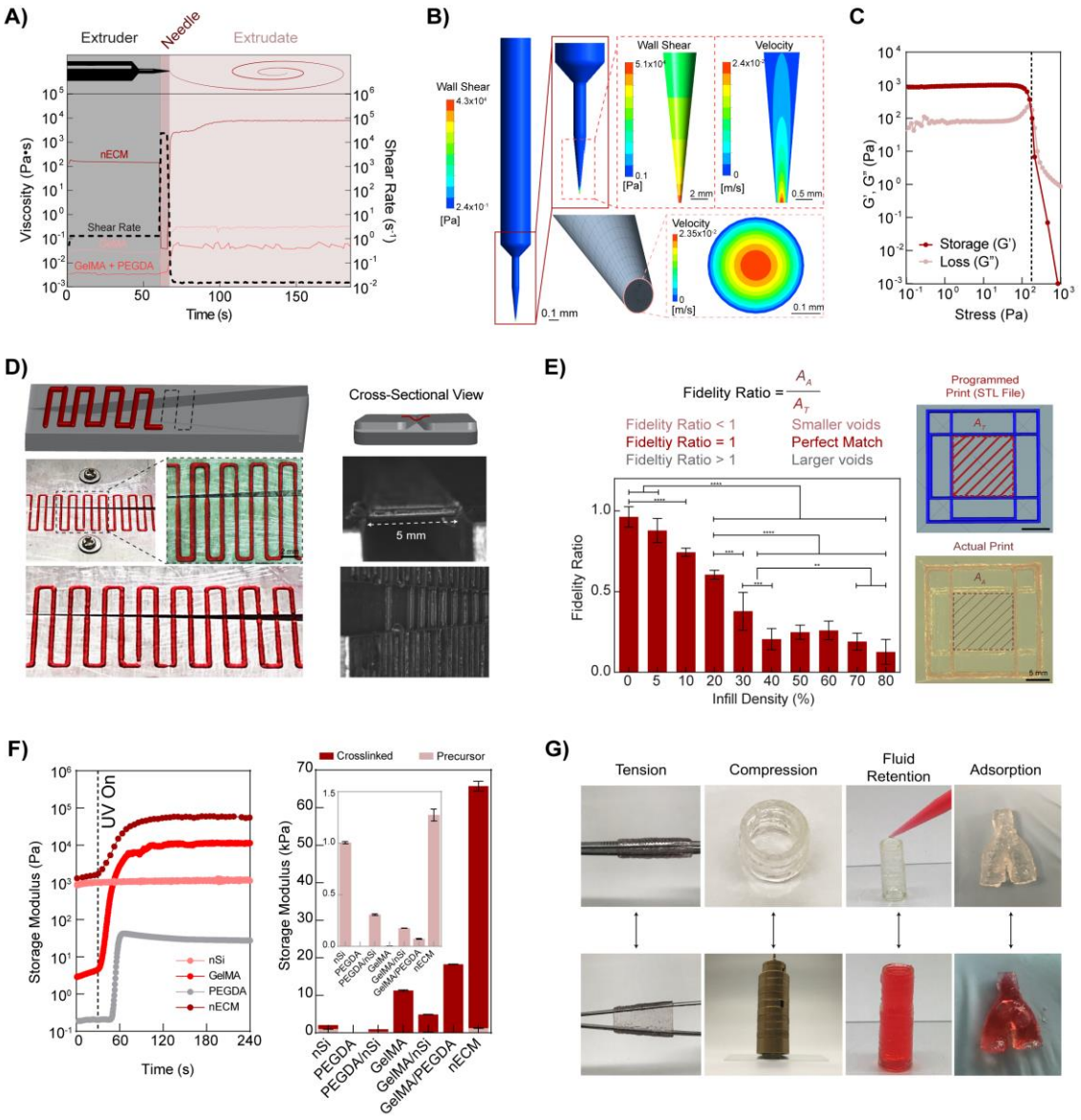

Figure 2- 6 Rheological and biophysical characterization of nECM bioink. A) Utilizing the flow-behavior index and consistency index, shear-rates are defined for specific locations within the printing process, represented by the dotted line corresponding to the right y-axis. When applied to GelMA and GelMA/PEGDA, the viscosity (left y-axis) remains below 1 Pa·s. However, when applied to the nECM, the bioink remains viscous when in the extruder, while rapid decreases when flowing through the needle gauge, permitting for extrusion. Post-extrusion, the extrudate rapidly recovers a high viscosity, permitting for shape-retention when deposited onto the printing bed. B) Rheological modeling of the nECM behavior throughout the printing process demonstrates a plug like flow, with the wall shear stress highest at the walls. C) A stress sweep validates the rheological modeling presented in B. D) The nECM is able to bridge a gap, up to a length of 5 mm, without any supporting structures, demonstrating the bioinks ability to support itself. E) Fidelity ratio is dependent on the infill density of printed lattice networks. Vascular assemblies, containing no

infill density due to their hollow nature, present a fidelity ratio ~1 (ideal match) and thus supports enhanced reliability of the optimized nECM formulation to construct programmed scaffolds. F) Time-sweep with exposure to UV light after 30 seconds demonstrates that the addition of nanosilicates does not impede covalent crosslinking of polymer precursor solutions post-printing and significantly increases the storage of the storage modulus compared to the bioinks constituents. G) Manipulations of printed structures after curing *via* tension, compression, fluid retention, and adsorption validate the mechanical integrity of the printed nECM constructs.

2.5 Bioprinting nECM Conserves the Phenotype of Vascular Endothelial Cells and Smooth Muscle Cells

Introducing cells within the bioink can alter interactions between bioink components, affecting both the rheological properties and extrusion process. (**Figure 2-7A**) To ensure that the encapsulation of VSMCs within the nECM bioink does not affect printing parameters and construct fidelity, different densities of VSMCs (0.5-10 million/mL) were incorporated into the nECM bioink and the rheological characteristics assessed. (**Figure 2-7B**) Interestingly, as the cell density was increased, the consistence index (K) decreased correspondingly. This is hypothesized to be due to the disruption of polymer-polymer and polymer-nanosilicates interactions due to the presence of cells. However, even though a decrease in K was observed, all densities maintained a shear-thinning, thixotropic behavior ($n < 1$); thus all densities can be used for 3D bioprinting applications. Utilizing a cell density of 2.5 million VSMCs per milliliter, cells maintained a high viability post-extrusion as well as demonstrated an increase in cell spreading and elongation between days 1, 3, and 7. (**Figure 2-7C**)

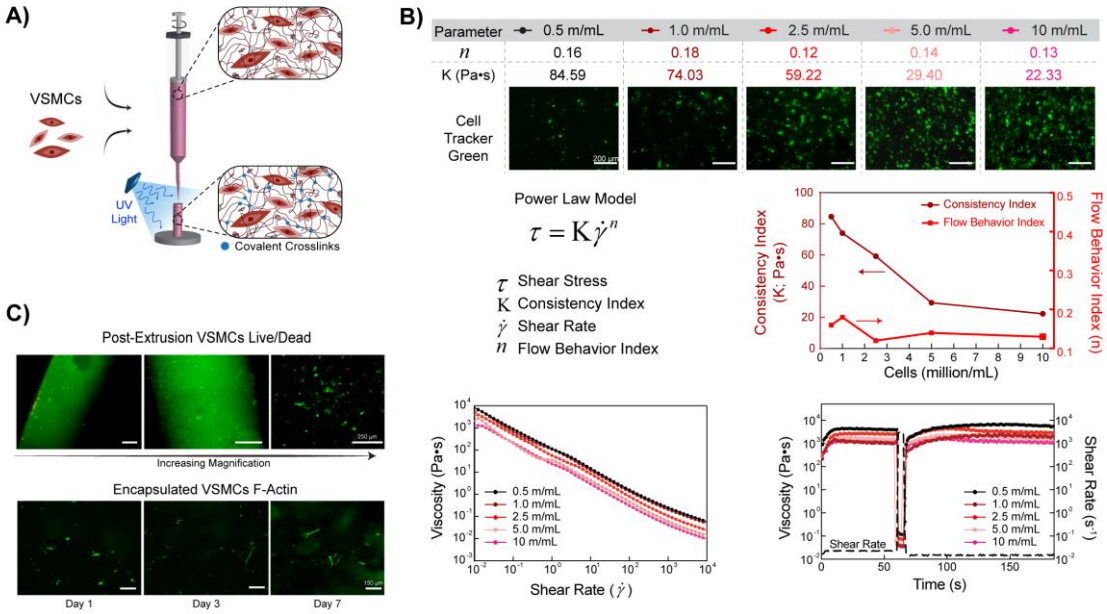

Figure 2- 7 3D Bioprinting using nECM bioink. A) Schematic illustrating VSMC encapsulation and extrusion for 3D bioprinting. B) All cell densities encapsulated within the nECM maintained a high low-shear viscosity, shear thinning profile (flow behavior index < 1), and recoverability optimal for 3D bioprinting. However, as the encapsulation density was increased, the consistency index decreased in a logarithmic manner. C) Directly after extrusion, VSMCs maintained a high cell viability, illustrating an increase in magnification from left to right (top row). After crosslinking the nECM, encapsulated VSMCs demonstrate an increase in spreading and elongation between days 1, 3, and 7 (bottom row).

Aside from cells affecting material interactions, cells are sensitive and can be affected by a multitude of environmental factors, such as material constituents and shear forces within the 3D bioprinting process, that can have a major impact on cellular viability and phenotypic maintenance. To assess these variables, ECs and VSMCs were monitored for 30 days, demonstrating long-term maintenance of metabolic activity, independent of the fabrication technique being used (i.e. seeding, encapsulating, printing). (**Figure 2-8A**) Relative to day 1, we observed an increase in metabolic activity, demonstrating vascular cell proliferation when interacting with the nECM bioink. This was further confirmed

through live cell analysis of the VSMCs on days 1, 7, and 30 (**Figure 2-8B**). In addition, cell viability and phenotypic maintenance (ECs: vascular endothelial-cadherin, VE-cadherin; VSMCs: α - smooth muscle actin, α - SMA) were assessed on days 1, 3, and 7. (**Figure 2-8C** and **2-8D**) Both cell types demonstrated a high viability (> 80%) as well as an increase in proliferation over time. Phenotypic maintenance was also validated using quantitative real-time polymerase chain reaction (qRT-PCR), demonstrating no significant difference in cell-specific markers (ECs: VE-cadherin, vWF, and eNOS; VSMCs: ACTA2, CNN1, and TAGLN) between nECM bioink and TCPS controls. Therefore, the nECM bioink is able to maintain construct integrity and deposition fidelity upon cell encapsulation, independent of the cell density being used, as well as support improved biocompatibility (i.e. cellular viability and phenotypic maintenance).

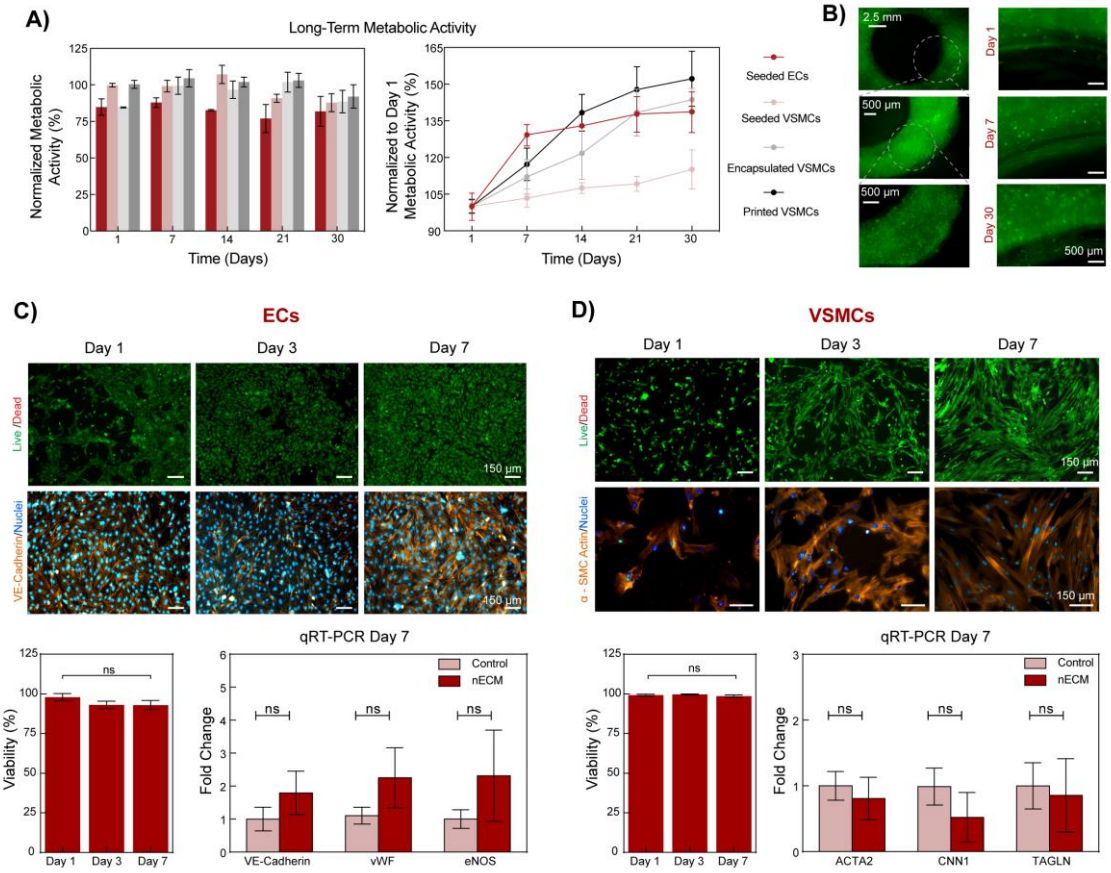

Figure 2- 8 Vascular cell metabolic activity, viability and phenotypic maintenance of vascular cells. A) Long-term metabolic activity was maintained up to 30 days when normalized to a TCPS control. Normalizing to Day 1, demonstrated an increase in metabolic activity independent of the fabrication technique being used, correlating to cellular proliferation. B) Cells imaged *via* cell tracker show increase in proliferation between days 1 and 30. C) ECs and D) VSMCs demonstrate a high viability (> 80 %) and increase in cell number from Day 1 to Day 7. In addition, both C) ECs and D) SMCs maintain a healthy phenotype as illustrated in immunohistochemistry staining on days 1, 3, and 7 as well as verified with qRT-PCR on day 7, showing no significant difference when compared to tissue culture polystyrene controls.

2.6 3D Bioprinting Anatomically Sized Vascular Structures

Current vascular models are not able to accurately recapitulate human vascular anatomy, thus much needed localization and interactions between EC-VSMC communication observed in native-like microenvironment is needed. Utilizing a 3D bioprinting approach

with our nECM bioink, VSMCs can be extruded into cylindrical constructs, localizing VSMCs within the nECM bioink to form a living medial layer. Next, ECs can then be seeded on the extruded geometry, forming a confluent monolayer that recapitulates the vascular lumen. Both cells were combined and localization of seeded ECs and VSMCs embedded within the nECM were verified to establish a co-culture model. (**Figure 2-9A**)

To recapitulate the intima and tunica media layers of human vasculature, both cells were combined and localized through seeding of ECs and encapsulation of VSMCs within the nECM, establishing a co-culture model. (**Figure 2-9A**) *En Face* is currently a technique used to characterize and image harvested vascular conduits *in vivo*. (218, 219) Specifically, conduits are cut into two independent specimen that are laid flat between two glass slides for further analysis. Employing this technique to our 3D bioprinted vascular model, VSMCs (green) are shown to be evenly distributed throughout the nECM in 3D (dispersed along the z-axis), while ECs (red) are shown to make a confluent, 2D monolayer on the nEMC (localized on the x, y- plane) (**Figure 2-9B**) This data illustrates the ability of our nECM bioink to fabricate constructs with living EC and VSMC co-culture, providing a tool to create anatomically accurate architectures innate to human blood vessels.

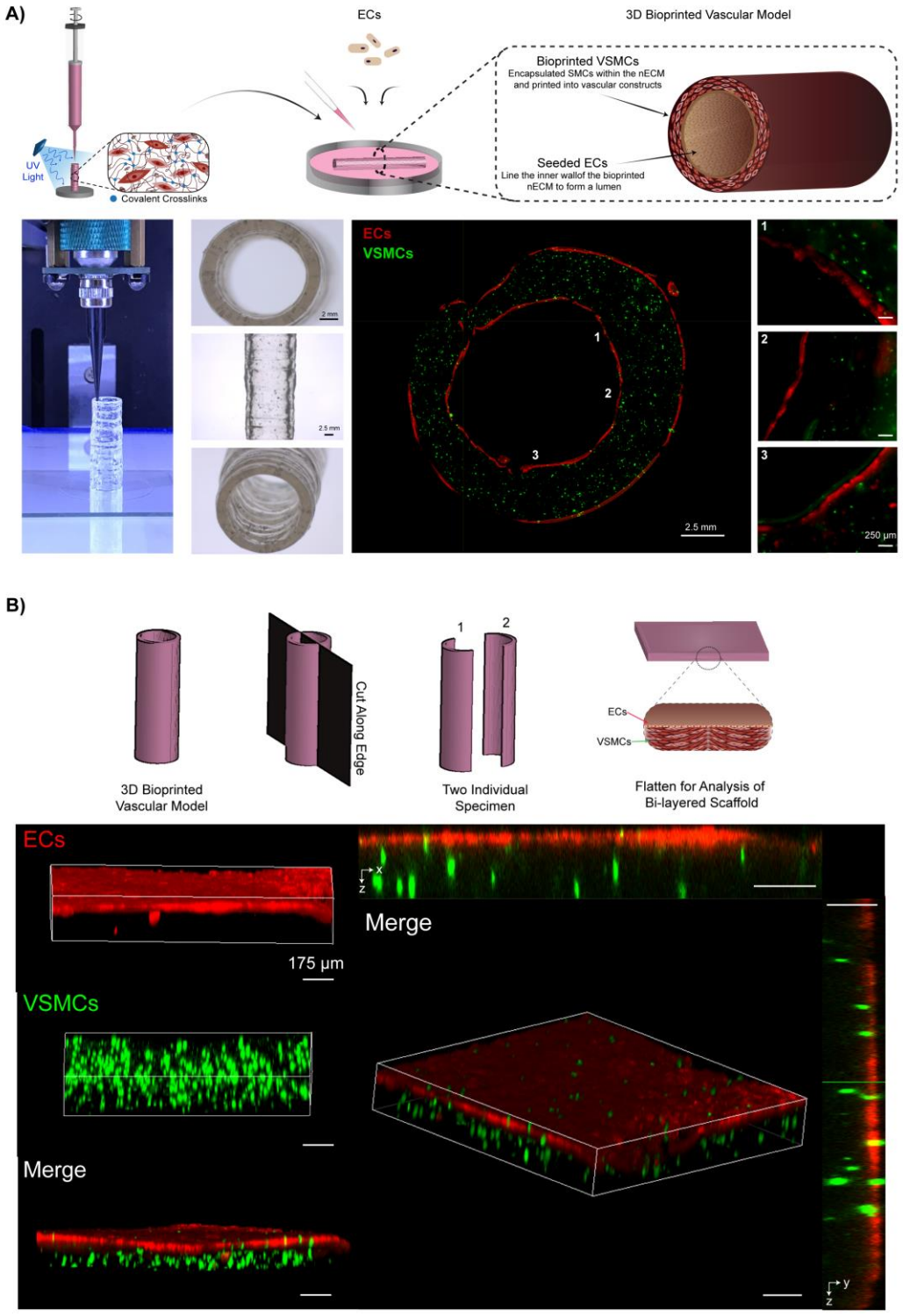

Figure 2- 9 3D bioprinted vascular model. A) Depiction of the method used to fabricate the 3D bioprinted vascular model with EC and VSMC co-culture. Staining with different colors of cell

tracker, EC-VSMC co-culture is depicted with spatial-temporal control to recapitulate the structure of native human vasculature. B) Schematic illustrating the *En Face* characterization technique, including cutting the model into two independent samples for cell localization verification. Staining with cell tracker, ECs are shown to be localized on the top surface (x,y-plane) and VSMCs localized in 3D (z-plane).

2.7 3D Bioprinted Blood Vessels Mimic Thromboinflammatory Outcomes

Next, we set out to determine if this 3D bioprinted vessel is able to recapitulate the geometry and obstruction observed in native human vessels. To achieve this, utilizing optical coherence tomography (OCT), we imaged a left anterior descending artery and compared it to a fabricated 3D bioprinted vessel with no endothelium present. (**Figure 2-10A**) After clotting overnight, no significant difference was observed in percent obstruction between the human artery and our 3D bioprinted model. Furthermore, we also wanted to assess whether the fabricated model is able to accurately mimic vascular thromboinflammatory responses upon endothelium activation through cytokine-induced injury. To do this, we stimulated 3D bioprinted vessels with TNF-α and hypothesized that, like *in vivo* or in other physio-mimetic *in vitro* models (220, 221), we would observe disruption in barrier function and blood clotting in a dose-dependent manner. (**Figure 2-10B**) Utilizing OCT, untreated bioprinted vessels perfused with blood, revealed no obstruction of the vessel, mimicking a healthy vascular lumen (0.07 ± 0.02 % obstruction**,** **Figure 2-10B**). On the contrary, when no endothelium was formed and blood was perfused through only the nECM (red), significant clotting (yellow) was observed, demonstrating 32 ± 8 % obstruction. Given the difference in refractive index between the nECM and clotted blood, clot formation can further be validated by the average intensity

differences presented before and after clotting. Specifically, before clotting, no significant difference was reflected in the average intensity between the two groups. However, after clotting, a significant difference in average intensity was observed and directly correlated to the presence of blood. Explicitly, higher intensities are presented with no endothelium (25 ± 2 a.u) and lower intensities with a confluent endothelium (16 ± 3 a.u), when compared to the baseline average intensity of the nECM itself (10 ± 1 a.u).

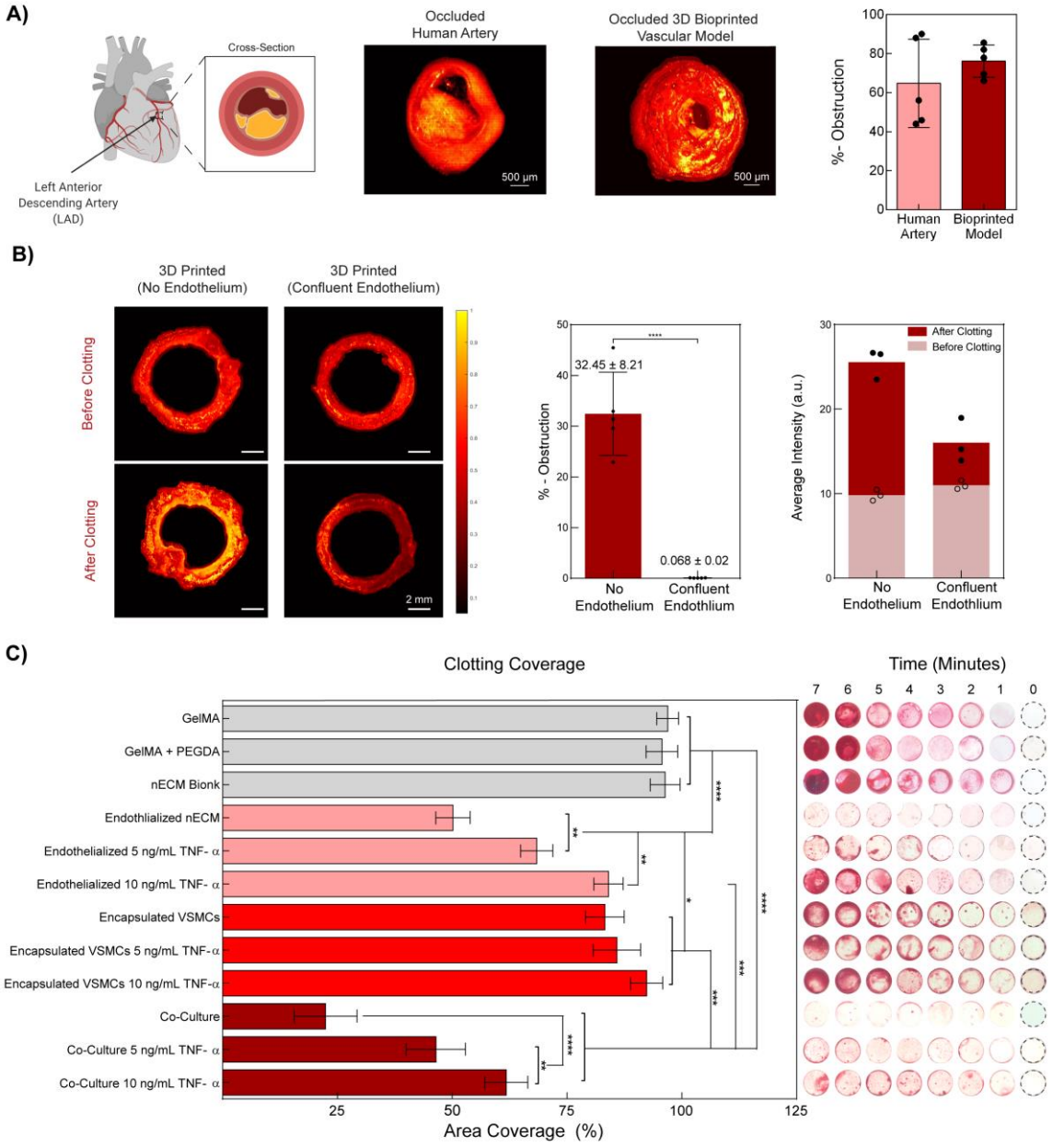

Figure 2- 10 Functional validation of 3D bioprinted vascular model. A) Optical Coherence Tomography (OCT) is used to determine obstruction of the lumen following blood perfusion, demonstrating the formation of diseased model. Comparing a clotted human left anterior descending artery to the occluded bioprinted vascular model (no endothelium), similar geometries are achieved and no significant difference in obstruction is observed after 12 hours of clotting. B) OCT of a 3D printed (no endothelium) and 3D printed (confluent endothelium) was performed in pre- and post-stenosed models. When no endothelium was present, a significant amount of clotting is depicted, increasing the percent obstruction as compared to when a confluent endothelium is present. Comparing the average intensities between groups demonstrated a significant increase, further supporting clotting formation. C) To exemplify dose-dependent sensitivity, static clotting

experiments were performed. With no lumen formation (GelMA, GelMA+PEGDA, nECM, Encapsulted VSMCs, Encapsulted VSMCs with 5 ng/mL TNF-α, and Encapsulted VSMCs with 10 ng/mL TNF-α), there was a significant increase in area coverage after 7 minutes. However upon the addition of ECs, the area coverage significantly decreases and demonstrates a dose-dependent effect on percent area coverage with TNF-α stimulation.

Subsequently, additional experimentation revealed that after 7 minutes of blood exposure, high clotting coverage was observed for GelMA (97 ± 2 %), GelMA/PEGDA (96 ± 3.5 %), and the nECM (96 ± 3 %). (**Figure 2-10C**) However, the presence of a confluent EC layer resulted in a significant reduction in clotting coverage (50 ± 4 %). When ECs cultured on the nECM were treated with 5 and 10 ng/mL of TNF-α for 18 hours, a dose-dependent trend was observed. Explicitly, ECs treated with 5 ng/mL exhibited regions of disrupted barrier function, causing an increase in clotting and therefore percent coverage (68 ± 3.5 %). When ECs are treated with a higher dose of TNF-α (10 ng/mL), the barrier function is further compromised compared to the 5 ng/mL dosage. Correspondingly, this leads to further clotting as measured through percent coverage (84 ± 3 %). Next, clotting coverage of encapsulated VSMCs in the absence of an endothelium was evaluated. A high clotting coverage was observed in encapsulated VSMCs after 7 minutes of blood exposure, irrespective of the TNF-α dosage delivered. (VSMCs: 83 ± 4 %; VSMCs with 5 ng/mL TNF- α: 86 ± 5 %; VSMCs with 10 ng/mL of TNF- α: 92 ± 4%) This is hypothesized to due to the absence of a confluent lumen, correlating to similar to results observed on GelMA, GelMA + PEGDA, and nECM bioink controls. Nonetheless, upon the incorporation of lumenal ECs on encapsulated VSMCs, fabricating a co-culture model, a significantly altered clotting phenomena was observed. Specifically, a significant

reduction in clotting coverage was observed upon co-culturing ECs and VSMCs compared to relative individual cultures (22 ± 7%), suggesting cellular cross-talk and communication within the 3D printed model. It is hypothesized that EC-VSMC communication modifies EC expression of inflammatory markers and potentially alters cellular phenotype. (222, 223) For example, it has been shown that in the presence of VSMCs, ECs adhere slower and present a less thrombotic phenotype. (224-226) Inclusively, this demonstrates the ability of this 3D bioprinted vascular model to recapitulate responses of vascular activation and blood perfusion, which has currently only been demonstrated in animal models or microfluidic organ-on-chips, but not in 3D printed vessel of a large cylindrical anatomy.

To further assess for EC-VSMC communication, we compared a stimulated 3D bioprinted model (10 ng/mL TNF-α) to a control, healthy EC-VSMC co-culture model, specifically assessing for EC barrier disruption (**Figure 2-11A, B**). EC monoculture demonstrated exposure of the underlying nECM bioink, as depicted by white arrows in the figure. This exposure is further increased upon TNF-α stimulation. This observation supports the hypothesis that stimulation disrupts the EC barrier function, leading to the increased clotting coverage previously observed. However, upon co-culturing VSMCs and ECs within the vascular model, ECs form a confluent monolayer on the nECM surface with tight VE-cadherin junction formed. Upon stimulating this co-culture model with TNF-α, VE-cadherin staining is decreased, however the confluent EC monolayer is conserved and inhibit exposure of the underlying nECM bioink to blood. Furthermore, ECs without stimulation in both mono- and co-culture systems did not demonstrate any form of

alignment, however upon exposure to 10 ng/mL of TNF-α, an increase in cellular alignment was observed along the 30 – 60˚ direction. We hypothesize this observation to be due to the endothelium attempting to recover from the inflamed response. In addition, ECs mono-culture demonstrated an increase in inflammatory markers, specifically interleukin-8 (IL-8), interleukin-6 (IL-6), interleukin-1β (IL-1β), and monocyte chemoattractant protein-1 (MCP-1) (**Figure 2-11C**). 3D bioprinted VSMCs cultured independently significantly decreased the inflammatory response in comparison to EC monoculture. This decrease in inflammatory markers was also observed in co-culturing of VSMCs and ECs together, supporting previous results of VSMCs promoting a less thrombotic EC phenotype.(224, 225, 227) In addition, the presence of VSMCs also significantly increased the expression of vascular endothelial growth factor (VEGF). This increase is hypothesized to promote re-endothelialization of the exposed surface.(228)

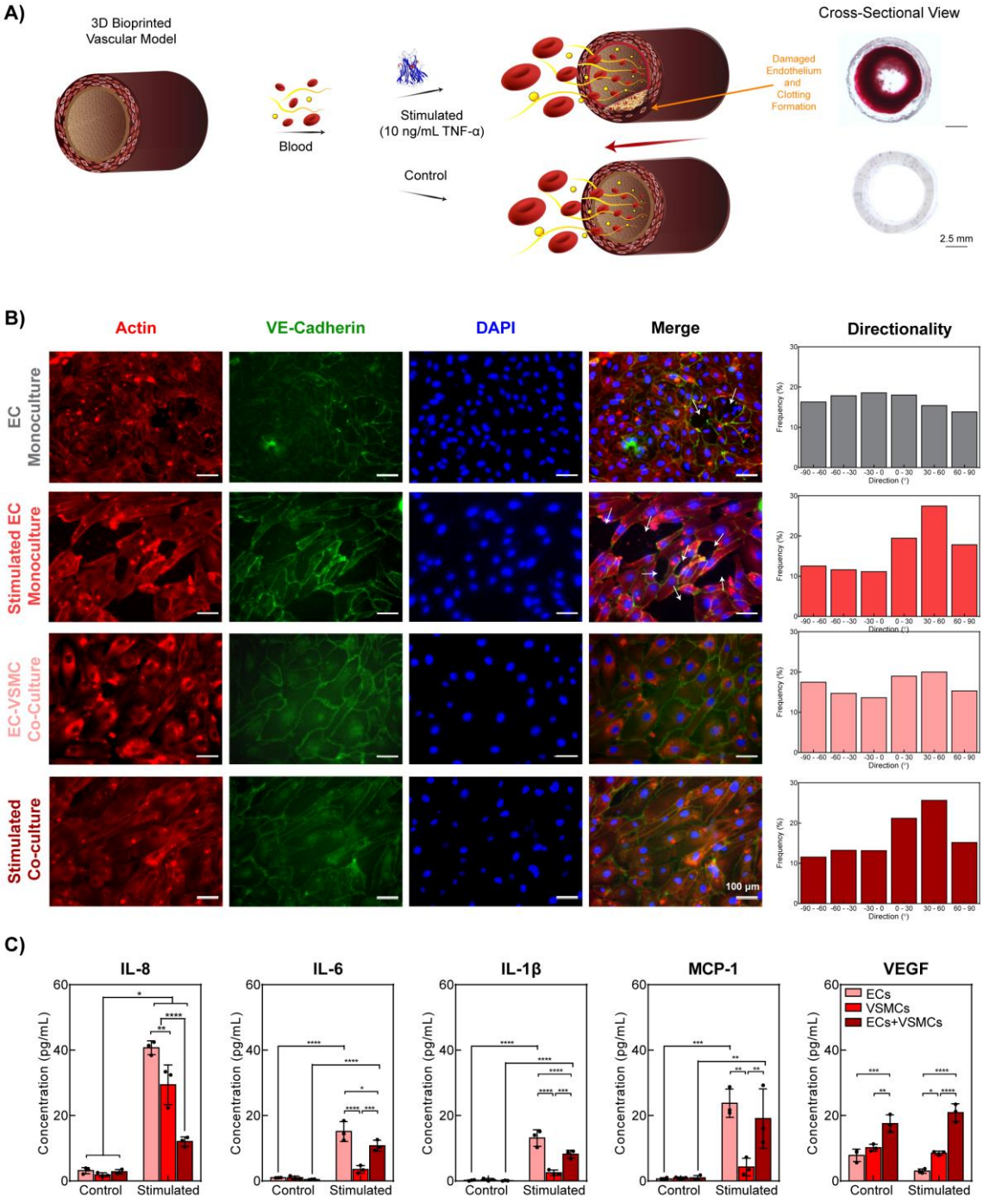

Figure 2-11 Vascular cell communication. A) Schematic demonstrating clotting formation with a TNF-α stimulated endothelium. TNF-α disrupts EC barrier function, initiating clotting. B) EC monoculture demonstrates exposure of the underlying matrix (white arrows), yet the area of exposed nECM bioink is increased upon TNF-α stimulation. Upon co-culture, a healthy, confluent monolayer is formed with VE-Cadherin junctions connecting the ECs. Upon stimulation, VE-Cadherin is decreased, however a confluent monolayer of ECs is still present. Upon stimulation,

ECs tend to align, demonstrating an increased alignment along 30 – 60˚ direction. C) Co-Culturing of ECs and VSMCs modified EC expression, resulting in a reduction of inflammatory markers IL-8, IL-6, IL-1β , and MCP-1 as well as increases VEGF expression, motivating a more atheroprotective phenotype.

2.8 Conclusion

In summary, we report a 3D bioprinted nECM for the fabrication of a blood vessel that offers improved mechanical properties, print fidelity, long-term co-culture of vascular ECs and VSMCs, response to cytokine-induced injury, and increased clotting in a dose dependent manner. Overall, this engineered vascular model confirms the unique ability of 3D bioprinting of the developed nECM to fabricate anatomically accurate structures that can recapitulate human *in vivo* conditions. Fundamentally, this work will be an invaluable tool to evaluate vascular diseases pathophysiology and assess interventions to accelerate therapeutic development.

3. FUTURE RECOMMENDATIONS

Despite the growing clinical burden of cardiovascular disease, drug advancements have become stagnated over the past 20 years, experiencing the strongest reduction of 4.57%. (229) The decrease in cardiovascular therapeutic development is attributed to the lack of efficiency when converting promising remedies into approved and marketed interventions, specifically due to the discrepancy between *in vitro* and *in vivo* studies. (230) Thus, there is a strong need for renovating current methodologies to minimize this gap and improve upon the translatability between *in vitro* and *in vivo* techniques to accurately reflect upon human pathophysiology.

Advancements within tissue engineering, specifically material development and additive manufacturing techniques, have provided innovative solutions to replicate vasculature, with the innate ability to grow and remodel *in vitro* for the use of vascular grafting applications. (215, 231-235) 3D bioprinting, a subclass of fused deposition modeling or extrusion printing, is capable of producing heterogeneous, tissue-shaped constructs in a layer-by-layer fashion with embedded cells, demonstrating enormous promise to recapitulate the native, multi-cellular vascular anatomy. In our studies, a nECM bioink was fabricated and characterized to understand and translate material-material as well as material-cell interactions for bioprinting applications. The designed nECM bioink enabled construction of a vascular platform to investigate human pathophysiology, specifically

vascular thromboinflammation due to cytokine injury. While the studies presented provide strong evidence for the use of this bioink and fabrication technique to serve as a modeling platform, the present work also demonstrates future opportunities to further investigate and recapitulate vascular anatomy and pathophysiology.

One challenge in the design of vascular models is the diversity and abundance of cell types involved, such as ECs, VSMCs, fibroblasts, monocytes, and blood cells. While we examined ECs and VSMCs to mimic the intima and tunica media layers, fabricating a tri-layered tissue with fibroblasts to recapitulate the adventitia layer would provide a more accurate representation of the vascular anatomy and therefore would demonstrate a more cohesive understanding of cellular cross-talk upon cytokine injury. Explicitly, the inclusion of an adventitia layer would more accurately portray native human physiology and aid in the regulation of a healthy phenotype (regulation, extravasation, or intravasation). (7, 8) In addition to including a third layer, variations in polymeric molecular weight (PEGDA) and ratios will potentially influence the mechanical properties of the vascular model, providing a potential platform to investigate vascular aging.

Bridging fields, such as engineering disciplines and biology, enables a holistic and broader understanding of critical aspects of vascular disease development and progression. While, most 3D printing research in the field of biomedical engineering only extends to live/dead or metabolic activity assays, we performed a more extensive analysis, demonstrating an in-depth characterization and assessment of our system to better serve as a model platform.

Future work could further incorporate other biological and bioinformatics techniques, such as RNA-sequencing, proteomics, and metabolomics. Incorporation of such methods would provide a more comprehensive and cohesive picture of the fabricated system. By assessing multiple levels of molecular mechanisms, we can better understand and predict vascular cell communication and cross-talk to define specific target genes and aid in the design of next-generation therapeutic interventions.

Emerging physiological accuracy and therefore complexity motivates the need to expand polymeric bioinks and fabrication techniques to more accurately reflect upon the human anatomy. Current systems, such as extrusion-based printing and micro-physiological organ-on-a-chip techniques, are widely studied for disease modeling applications. However, future endeavors should aim to more accurately portray the human anatomy and therefore pathophysiology. For example, micro-physiological organ-on-a-chip systems should incorporate more complex material designs and fabrication techniques rather than bulk PDMS or PDMS porous membranes to better resemble the native human ECM. In addition, 3D bioprinting should examine sacrificial printing techniques or multi-material printing techniques to fabricate more complex, anatomically-accurate geometries.

4. CONCLUSION

Through this work, we have demonstrated the ability to combine 3D printing methods, advanced material design, multifaceted imaging techniques, and standard biological procedures to design an improved vascular disease model. In particular, we have (a) introduced a novel material design to engineer a high viscosity, shear-thinning, and recoverable bioink to enable printing of 3D architectures, (b) demonstrated the ability to construct programmable, multi-cellular architectures to model complex biological events, such as thromboinflammation, and (c) established a new platform to recapitulate and assess human vascular structure, anatomy, and pathophysiology.

First, we characterized the fundamental interactions of bioink constituents (GelMA, PEGDA, nanosilciates) and their combinations to derive and optimize an ideal composition for 3D bioprinting. The addition of nanosilicates to GelMA + PEGDA composites yields a shear-thinning and recoverable precursor solution in a concentration-dependent manner. With the optimal nECM bioink formulation deduced, printing integrity was thoroughly characterized to fabricate anatomically accurate vascular constructs that can be manipulated post-extrusion.

Subsequently, *in vitro* cytocompatibility of ECs and VSMCs with the designed nECM was determined, demonstrating long-term maintenance of metabolic activity, viability, and

phenotype of vascular cells. Furthermore, the rheological behavior of bioinks was conserved upon the encapsulation of VSMCs, regardless of the cell encapsulation density used. This flow profile protects cells from high shear forces during the bioprinting process and enables localization of cell types with high print fidelity, mimicking the vessel's macro- and micro-architectures. Overall, the nECM bioink is able to construct vessels with spatial-temporal control by bioprinting VSMC and seeding ECs, enabling fabrication of a multicellular vascular model.

Lastly, we validated the 3D bioprinted model's ability to recapitulate native vascular phenomena. This was illustrated by stimulating ECs with TNF-α, disrupting EC barrier function and thus inducing clotting formation. Applying standard clinical techniques, Optical Coherence Tomography (OCT) was used to gain a microstructural understanding of plaques formed within the printed lumen. Furthermore, TNF-α stimulation did not demonstrate any effect on VSMC. However, upon co-culture between both ECs and VSMCs, a significant reduction of clotting was observed, thus suggesting EC-SMC communication within the modeling system to prompt a thrombo-protective phenotype.

Taken together, the designed, fabricated, and assessed vascular model serves as a potential tool to investigate vascular disease pathophysiology. These works present significant advances in understanding nanocolloidal composite interactions and their use as a bioink. In particular, examination of bioink flow properties in combination with print fidelity characterization is essential to precisely deposit the printing extrudate and support itself

into a 3D construct. Precursor flow behavior and printing parameters govern the overall quality of the fabricated 3D scaffold; thus, establishing a cohesive understanding of these variables governs the precision and translatability of the extrudate to form intended geometries. Nevertheless, bioinks are defined as materials or carriers to deliver cells, yet still fulfill the rheological requirements of traditional inks.(236) Cells vary in size, charge, and surface markers, depending on the cell type and source. Thus, introducing cells, such as VSMCs, can have an overall effect on polymeric interactions within the bioink, affecting both the rheological properties and extrusion process as well. Accordingly, characterization methods performed to understand flow and printing properties should be extended to the combination of cells and materials, recognizing the consequences of cell encapsulation on the bioink's rheological profile and platform fidelity.

Fundamentally, these works demonstrate the use of 3D bioprinting to engineer and fabricate 3D vascular models and investigate biological processes (e.g. tissue development, regeneration, and disease progression) as well as assess the safety/efficacy of biochemical agents (e.g. therapeutic development).

REFERENCES

1. Mozaffarian D, *et al.* (2015) Heart Disease and Stroke Statistics—2015 Update. *A Report From the American Heart Association* 131(4):e29-e322.
2. Wolf F, Vogt F, Schmitz-Rode T, Jockenhoevel S, & Mela P (2016) Bioengineered vascular constructs as living models for in vitro cardiovascular research. *Drug Discovery Today* 21(9):1446-1455.
3. Kinza Islam SBT, Rasha Nasser, Deborah L Gater, Tanthe E Pearson, N Christoforoul, and Jeremy CM Teo (2016) Co-culture Methods Used to Model Atherosclerosis In Vitro Using Endothelial, Smooth Muscle and Monocyte Cells. *SM Journal of Biomedical Engineering* 2(1).
4. Huang AH, *et al.* (2016) Biaxial Stretch Improves Elastic Fiber Maturation, Collagen Arrangement, and Mechanical Properties in Engineered Arteries. *Tissue Engineering Part C: Methods* 22(6):524-533.
5. Claes E, *et al.* (2010) Mechanical properties of human coronary arteries. *2010 Annual International Conference of the IEEE Engineering in Medicine and Biology*, pp 3792-3795.
6. Karimi A, Navidbakhsh M, Shojaei A, & Faghihi S (2013) Measurement of the uniaxial mechanical properties of healthy and atherosclerotic human coronary arteries. *Materials Science and Engineering: C* 33(5):2550-2554.

7. Gutterman DD (1999) Adventitia-dependent influences on vascular function. *American Journal of Physiology - Heart and Circulatory Physiology* 277(4):H1265-H1272.

8. Segal SS (1994) Cell-to-cell communication coordinates blood flow control. *Hypertension* 23(6 Pt 2):1113-1120.

9. Anonymous (2007) *Pathophysiology of Heart Disease: A collaborative Project of Medical Students and Faculty* (Lippincott Williams & Wilkins, Baltimore, MD) Fourth Ed.

10. Hansson GK (2005) Inflammation, Atherosclerosis, and Coronary Artery Disease. *New England Journal of Medicine* 352(16):1685-1695.

11. Hotamisligil GS (2010) Endoplasmic reticulum stress and atherosclerosis. *Nat Med* 16(4):396-399.

12. Weber C & Noels H (2011) Atherosclerosis: current pathogenesis and therapeutic options. *Nat Med* 17(11):1410-1422.

13. Wagenseil JE & Mecham RP (2009) Vascular Extracellular Matrix and Arterial Mechanics. *Physiological reviews* 89(3):957-989.

14. Ryan AJ, Brougham CM, Garciarena CD, Kerrigan SW, & O'Brien FJ (2016) Towards 3D in vitro models for the study of cardiovascular tissues and disease. *Drug Discovery Today* 21(9):1437-1445.

15. Rosenson RS, *et al.* (2017) HDL and atherosclerotic cardiovascular disease: genetic insights into complex biology. *Nature Reviews Cardiology* 15:9.

16. Rye K-A & Barter PJ (2014) Regulation of High-Density Lipoprotein Metabolism. *Circulation Research* 114(1):143-156.

17. Truskey GA (2010) Endothelial Cell Vascular Smooth Muscle Cell Co-Culture Assay For High Throughput Screening Assays For Discovery of Anti-Angiogenesis Agents and Other Therapeutic Molecules. *International journal of high throughput screening* 2010(1):171-181.

18. Persidis A (1999) Cardiovascular disease drug discovery. *Nature Biotechnology* 17:930.

19. Gromo G, Mann J, & Fitzgerald JD (2014) Cardiovascular Drug Discovery: A Perspective from a Research-Based Pharmaceutical Company. *Cold Spring Harbor Perspectives in Medicine* 4(6).

20. Hampton T (2017) How Useful Are Mouse Models for Understanding Human Atherosclerosis? *Review Examines the Available Evidence* 135(18):1757-1758.

21. von Scheidt M, *et al.* (2017) Applications and Limitations of Mouse Models for Understanding Human Atherosclerosis. *Cell Metabolism* 25(2):248-261.

22. Liao J, Huang W, & Liu G (2017) Animal models of coronary heart disease. *Journal of Biomedical Research* 31(1):3-10.

23. Getz GS & Reardon CA (2012) Animal Models of Atherosclerosis. *Arteriosclerosis, Thrombosis, and Vascular Biology* 32(5):1104-1115.

24. Davies PF (2009) Hemodynamic shear stress and the endothelium in cardiovascular pathophysiology. *Nat Clin Pract Cardiovasc Med* 6(1):16-26.

25. Emini Veseli B, *et al.* (2017) Animal models of atherosclerosis. *European Journal of Pharmacology* 816:3-13.

26. Hasenfuss G (1998) Animal models of human cardiovascular disease, heart failure and hypertrophy. *Cardiovascular Research* 39(1):60-76.

27. Russell JC & Proctor SD (2006) Small animal models of cardiovascular disease: tools for the study of the roles of metabolic syndrome, dyslipidemia, and atherosclerosis. *Cardiovascular Pathology* 15(6):318-330.

28. Hansen BC & Bodkin NL (1993) Primary Prevention of Diabetes Mellitus by Prevention of Obesity in Monkeys. *Diabetes* 42(12):1809-1814.

29. Hansen BC (1999) The Metabolic Syndrome X. *Annals of the New York Academy of Sciences* 892(1):1-24.

30. Meyvantsson I & Beebe DJ (2008) Cell Culture Models in Microfluidic Systems. *Annual Review of Analytical Chemistry* 1(1):423-449.

31. Farcas MA, Rouleau L, Fraser R, & Leask RL (2009) The development of 3-D, in vitro, endothelial culture models for the study of coronary artery disease. *BioMedical Engineering OnLine* 8(1):30.

32. Rouleau L, Copland IB, Tardif J-C, Mongrain R, & Leask RL (2010) Neutrophil Adhesion on Endothelial Cells in a Novel Asymmetric Stenosis Model: Effect of Wall Shear Stress Gradients. *Annals of Biomedical Engineering* 38(9):2791-2804.

33. Rouleau L, Rossi J, & Leask RL (2010) The Response of Human Aortic Endothelial Cells in a Stenotic Hemodynamic Environment: Effect of Duration,

Magnitude, and Spatial Gradients in Wall Shear Stress. *Journal of Biomechanical Engineering* 132(7):071015-071015-071011.

34. Rouleau L, Farcas M, Tardif J-C, Mongrain R, & Leask RL (2010) Endothelial Cell Morphologic Response to Asymmetric Stenosis Hemodynamics: Effects of Spatial Wall Shear Stress Gradients. *Journal of Biomechanical Engineering* 132(8):081013-081013-081010.

35. Young EWK, Watson MWL, Srigunapalan S, Wheeler AR, & Simmons CA (2010) Technique for Real-Time Measurements of Endothelial Permeability in a Microfluidic Membrane Chip Using Laser-Induced Fluorescence Detection. *Analytical Chemistry* 82(3):808-816.

36. Kolhar P, *et al.* (2013) Using shape effects to target antibody-coated nanoparticles to lung and brain endothelium. *Proceedings of the National Academy of Sciences* 110(26):10753-10758.

37. Korin N, *et al.* (2012) Shear-Activated Nanotherapeutics for Drug Targeting to Obstructed Blood Vessels. *Science* 337(6095):738-742.

38. Lamberti G, *et al.* (2013) Adhesive interaction of functionalized particles and endothelium in idealized microvascular networks. *Microvascular Research* 89:107-114.

39. Doshi N, *et al.* (2010) Flow and adhesion of drug carriers in blood vessels depend on their shape: A study using model synthetic microvascular networks. *Journal of Controlled Release* 146(2):196-200.

40. Cines DB, *et al.* (1998) Endothelial Cells in Physiology and in the Pathophysiology of Vascular Disorders. *Blood* 91(10):3527-3561.

41. Jeong Ai K, *et al.* (2005) Brain Endothelial Hemostasis Regulation by Pericytes. *Journal of Cerebral Blood Flow & Metabolism* 26(2):209-217.

42. Grant DS, *et al.* (1989) Two different laminin domains mediate the differentiation of human endothelial cells into capillary-like structures in vitro. *Cell* 58(5):933-943.

43. Morin O, Patry P, & Lafleur L (1984) Heterogeneity of endothelial cells of adult rat liver as resolved by sedimentation velocity and flow cytometry. *Journal of Cellular Physiology* 119(3):327-334.

44. Sankar S, *et al.* (1996) Modulation of transforming growth factor beta receptor levels on microvascular endothelial cells during in vitro angiogenesis. *Journal of Clinical Investigation* 97(6):1436-1446.

45. Cockerill GW, Rye K-A, Gamble JR, Vadas MA, & Barter PJ (1995) High-Density Lipoproteins Inhibit Cytokine-Induced Expression of Endothelial Cell Adhesion Molecules. *Arteriosclerosis, Thrombosis, and Vascular Biology* 15(11):1987-1994.

46. Owman C & Hardebo JE (1988) Functional Heterogeneity of the Cerebrovascular Endothelium. *Brain, Behavior and Evolution* 32(2):65-75.

47. Thornhill MH & Haskard DO (1990) IL-4 regulates endothelial cell activation by IL-1, tumor necrosis factor, or IFN-gamma. *The Journal of Immunology* 145(3):865-872.

48. Fillinger MF, Sampson LN, Cronenwett JL, Powell RJ, & Wagner RJ (1997) Coculture of Endothelial Cells and Smooth Muscle Cells in Bilayer and Conditioned Media Models. *Journal of Surgical Research* 67(2):169-178.

49. Owens GK, Kumar MS, & Wamhoff BR (2004) Molecular regulation of vascular smooth muscle cell differentiation in development and disease. *Physiol Rev* 84.

50. Beamish JA, He P, Kottke-Marchant K, & Marchant RE (2010) Molecular Regulation of Contractile Smooth Muscle Cell Phenotype: Implications for Vascular Tissue Engineering. *Tissue Engineering Part B: Reviews* 16(5):467-491.

51. Steucke KE, Tracy PV, Hald ES, Hall JL, & Alford PW (2015) Vascular smooth muscle cell functional contractility depends on extracellular mechanical properties. *Journal of Biomechanics* 48(12):3044-3051.

52. Fernandez CE, *et al.* (2016) Human Vascular Microphysiological System for in vitro Drug Screening. *Scientific Reports* 6:21579.

53. Powell RJ, Cronenwett JL, Fillinger MF, & Wagner RJ (1994) Effect of endothelial cells and transforming growth factor-ß1 on cultured vascular smooth muscle cell growth patterns. *Journal of Vascular Surgery* 20(5):787-794.

54. Nackman GB, Bech FR, Fillinger MF, Wagner RJ, & Cronenwett JL (1996) Endothelial cells modulate smooth muscle cell morphology by inhibition of transforming growth factor-beta1 activation. *Surgery* 120(2):418-426.

55. Merrilees MJ & Scott L (1981) Interaction of aortic endothelial and smooth muscle cells in culture Effect on glycosaminoglycan levels. *Atherosclerosis* 39(2):147-161.

56. Skardal A, Shupe T, & Atala A (2016) Organoid-on-a-chip and body-on-a-chip systems for drug screening and disease modeling. *Drug Discovery Today* 21(9):1399-1411.

57. Bacabac RG, *et al.* (Dynamic shear stress in parallel-plate flow chambers. *Journal of Biomechanics* 38(1):159-167.

58. Bancroft GN, Sikavitsas VI, & Mikos AG (2003) Technical Note: Design of a Flow Perfusion Bioreactor System for Bone Tissue-Engineering Applications. *Tissue Engineering* 9(3):549-554.

59. Higgins JM, Eddington DT, Bhatia SN, & Mahadevan L (2007) Sickle cell vasoocclusion and rescue in a microfluidic device. *Proceedings of the National Academy of Sciences* 104(51):20496-20500.

60. Barabino G, McIntire L, Eskin S, Sears D, & Udden M (1987) Endothelial cell interactions with sickle cell, sickle trait, mechanically injured, and normal erythrocytes under controlled flow. *Blood* 70(1):152-157.

61. Nash G, Johnson C, & Meiselman H (1988) Rheologic impairment of sickle RBCs induced by repetitive cycles of deoxygenation-reoxygenation. *Blood* 72(2):539-545.

62. Young EWK & Simmons CA (2010) Macro- and microscale fluid flow systems for endothelial cell biology. *Lab on a Chip* 10(2):143-160.

63. Young EWK & Beebe DJ (2010) Fundamentals of microfluidic cell culture in controlled microenvironments. *Chemical Society Reviews* 39(3):1036-1048.

64. Griffith LG & Swartz MA (2006) Capturing complex 3D tissue physiology in vitro. *Nature Reviews Molecular Cell Biology* 7:211.

65. Schaff UY, *et al.* (2007) Vascular mimetics based on microfluidics for imaging the leukocyte-endothelial inflammatory response. *Lab on a Chip* 7(4):448-456.

66. Ingber DE (2003) Tensegrity I. Cell structure and hierarchical systems biology. *Journal of Cell Science* 116(7):1157-1173.

67. Ingber DE (2003) Tensegrity II. How structural networks influence cellular information processing networks. *Journal of Cell Science* 116(8):1397-1408.

68. Yasotharan S, Pinto S, Sled JG, Bolz S-S, & Gunther A (2015) Artery-on-a-chip platform for automated, multimodal assessment of cerebral blood vessel structure and function. *Lab on a Chip* 15(12):2660-2669.

69. Ribas J, *et al.* (2016) Cardiovascular Organ-on-a-Chip Platforms for Drug Discovery and Development. *Applied In Vitro Toxicology* 2(2):82-96.

70. Jain A, *et al.* (2016) Assessment of whole blood thrombosis in a microfluidic device lined by fixed human endothelium. *Biomedical Microdevices* 18:73.

71. Jain A & Munn LL (2011) Biomimetic postcapillary expansions for enhancing rare blood cell separation on a microfluidic chip. *Lab on a Chip* 11(17):2941-2947.

72. Jain A, *et al.* (2016) A shear gradient-activated microfluidic device for automated monitoring of whole blood haemostasis and platelet function. *Nature Communications* 7:10176.

73. Benam KH, *et al.* (2015) Engineered In Vitro Disease Models. *Annual Review of Pathology: Mechanisms of Disease* 10(1):195-262.

74. Bertassoni LE, *et al.* (2014) Hydrogel bioprinted microchannel networks for vascularization of tissue engineering constructs. *Lab on a Chip* 14(13):2202-2211.

75. Westein E, *et al.* (2013) Atherosclerotic geometries exacerbate pathological thrombus formation poststenosis in a von Willebrand factor-dependent manner. *Proceedings of the National Academy of Sciences* 110(4):1357-1362.

76. Qiu Y, *et al.* (2018) Microvasculature-on-a-chip for the long-term study of endothelial barrier dysfunction and microvascular obstruction in disease. *Nature Biomedical Engineering* 2(6):453-463.

77. Alimperti S, *et al.* (2017) Three-dimensional biomimetic vascular model reveals a RhoA, Rac1, and N-cadherin balance in mural cell–endothelial cell-regulated barrier function. *Proceedings of the National Academy of Sciences* 114(33):8758-8763.

78. Costa PF, *et al.* (2017) Mimicking arterial thrombosis in a 3D-printed microfluidic in vitro vascular model based on computed tomography angiography data. *Lab on a Chip* 17(16):2785-2792.

79. Gunther A, *et al.* (2010) A microfluidic platform for probing small artery structure and function. *Lab on a Chip* 10(18):2341-2349.

80. Jain A, *et al.* (A primary human lung alveolus-on-a-chip model of intravascular thrombosis for assessment of therapeutics. *Clinical Pharmacology & Therapeutics*:n/a-n/a.

81. Janna CN, *et al.* (2018) Automated fabrication of photopatterned gelatin hydrogels for organ-on-chips applications. *Biofabrication* 10(2):025004.

82. van Engeland NCA, *et al.* (2018) A biomimetic microfluidic model to study signalling between endothelial and vascular smooth muscle cells under hemodynamic conditions. *Lab on a Chip* 18(11):1607-1620.

83. Zhang YS, *et al.* (2016) Bioprinted thrombosis-on-a-chip. *Lab on a Chip* 16(21):4097-4105.

84. Barrile R, *et al.* (2018) Organ-on-Chip Recapitulates Thrombosis Induced by an anti-CD154 Monoclonal Antibody: Translational Potential of Advanced Microengineered Systems. *Clinical Pharmacology & Therapeutics*.

85. Alimperti S, *et al.* (2017) Three-dimensional biomimetic vascular model reveals a RhoA, Rac1, and N-cadherin balance in mural cell–endothelial cell-regulated barrier function. *Proceedings of the National Academy of Sciences*.

86. Thomas A, Daniel Ou-Yang H, Lowe-Krentz L, Muzykantov VR, & Liu Y (2016) Biomimetic channel modeling local vascular dynamics of pro-inflammatory endothelial changes. *Biomicrofluidics* 10(1):014101.

87. Park JY, *et al.* (2011) Monitoring the status of T-cell activation in a microfluidic system. *Analyst* 136(13):2831-2836.

88. Kim S, Lee H, Chung M, & Jeon NL (2013) Engineering of functional, perfusable 3D microvascular networks on a chip. *Lab on a Chip* 13(8):1489-1500.

89. Fredrickson CK & Fan ZH (2004) Macro-to-micro interfaces for microfluidic devices. *Lab on a Chip* 4(6):526-533.

90. Whitesides GM (2006) The origins and the future of microfluidics. *Nature* 442:368.

91. Muthard RW & Diamond SL (2013) Side view thrombosis microfluidic device with controllable wall shear rate and transthrombus pressure gradient. *Lab on a Chip* 13(10):1883-1891.

92. Chueh B-h, *et al.* (2007) Leakage-Free Bonding of Porous Membranes into Layered Microfluidic Array Systems. *Analytical Chemistry* 79(9):3504-3508.

93. Shery Huang YY, Zhang D, & Liu Y (2017) Bioprinting of three-dimensional culture models and organ-on-a-chip systems. *MRS Bulletin* 42(8):593-599.

94. Wang X, *et al.* (2016) Engineering anastomosis between living capillary networks and endothelial cell-lined microfluidic channels. *Lab on a Chip* 16(2):282-290.

95. Memic A, *et al.* (2017) Bioprinting technologies for disease modeling. *Biotechnology Letters* 39(9):1279-1290.

96. F2792-12A AS (2013) Standard Terminology for additive manufacturing technologies. *ASTM International*.

97. Zhao X, *et al.* (2015) 3D patterned substrates for bioartificial blood vessels – The effect of hydrogels on aligned cells on a biomaterial surface. *Acta Biomaterialia* 26:159-168.

98. Irvine S & Venkatraman S (2016) Bioprinting and Differentiation of Stem Cells. *Molecules* 21(9):1188.

99. Bobak M, Guanglei X, Simon D, & James KM (2015) Current progress in 3D printing for cardiovascular tissue engineering. *Biomedical Materials* 10(3):034002.

100. Vukicevic M, Mosadegh B, Min JK, & Little SH (2017) Cardiac 3D Printing and its Future Directions. *JACC: Cardiovascular Imaging* 10(2):171-184.

101. Swati G, *et al.* (2016) Clinical Application and Multidisciplinary Assessment of Three Dimensional Printing in Double Outlet Right Ventricle With Remote Ventricular Septal Defect. *World Journal for Pediatric and Congenital Heart Surgery* 7(3):344-350.

102. Niklason LE, *et al.* (1999) Functional Arteries Grown in Vitro. *Science* 284(5413):489-493.

103. Laflamme K, *et al.* (2005) Tissue-Engineered Human Vascular Media With a Functional Endothelin System. *Circulation* 111(4):459-464.

104. Laflamme K, *et al.* (2006) Adventitia contribution in vascular tone: insights from adventitia-derived cells in a tissue-engineered human blood vessel. *The FASEB Journal* 20(8):1245-1247.

105. Diebolt M, *et al.* (2007) Polyphenols modulate calcium-independent mechanisms in human arterial tissue-engineered vascular media. *Journal of Vascular Surgery* 46(4):764-772.

106. Diebolt M, Germain L, Auger FA, & Andriantsitohaina R (2005) Mechanism of potentiation by polyphenols of contraction in human vein-engineered media. *American Journal of Physiology-Heart and Circulatory Physiology* 288(6):H2918-H2924.

107. Pricci M, *et al.* (2009) Applications of Human Tissue-Engineered Blood Vessel Models to Study the Effects of Shed Membrane Microparticles from T-Lymphocytes on Vascular Function. *Tissue Engineering Part A* 15(1):137-145.

108. K. MA, *et al.* (Microfluidics-Enabled Multimaterial Maskless Stereolithographic Bioprinting. *Advanced Materials* 0(0):1800242.

109. Massa S, *et al.* (2017) Bioprinted 3D vascularized tissue model for drug toxicity analysis. *Biomicrofluidics* 11(4):044109.

110. Kang H-W, *et al.* (2016) A 3D bioprinting system to produce human-scale tissue constructs with structural integrity. *Nat Biotech* 34(3):312-319.

111. Xiong G, Kolli K, Soohoo HA, & Min JK (2015) Abstract 19898: In-vitro Assessment of Coronary Hemodynamics in 3D Printed Patient-specific Geometry. *Circulation* 132(Suppl 3):A19898-A19898.

112. Kolli KK, Min JK, Ha S, Soohoo H, & Xiong G (2016) Effect of Varying Hemodynamic and Vascular Conditions on Fractional Flow Reserve: An In Vitro Study. *Journal of the American Heart Association* 5(7).

113. Chimene D, *et al.* (2018) Nanoengineered Ionic-Covalent Entanglement (NICE) Bioinks for 3D Bioprinting. *ACS Appl Mater Interfaces* 10(12):9957-9968.

114. Wang Z, Lee SJ, Cheng H-J, Yoo JJ, & Atala A (2018) 3D bioprinted functional and contractile cardiac tissue constructs. *Acta Biomaterialia*.

115. Ajay T, *et al.* (2018) Contact guidance for cardiac tissue engineering using 3D bioprinted gelatin patterned hydrogel. *Biofabrication* 10(2):025003.

116. Fukunishi T, *et al.* (2017) Preclinical study of patient-specific cell-free nanofiber tissue-engineered vascular grafts using 3-dimensional printing in a sheep model. *The Journal of Thoracic and Cardiovascular Surgery* 153(4):924-932.

117. Hockaday LA, *et al.* (2012) Rapid 3D printing of anatomically accurate and mechanically heterogeneous aortic valve hydrogel scaffolds. *Biofabrication* 4(3):035005.

118. Gao Q, *et al.* (2017) 3D Bioprinting of Vessel-like Structures with Multilevel Fluidic Channels. *ACS Biomaterials Science & Engineering* 3(3):399-408.

119. Kolesky DB, Homan KA, Skylar-Scott MA, & Lewis JA (2016) Three-dimensional bioprinting of thick vascularized tissues. *Proceedings of the National Academy of Sciences* 113(12):3179-3184.

120. Ouyang L, Highley CB, Rodell CB, Sun W, & Burdick JA (2016) 3D Printing of Shear-Thinning Hyaluronic Acid Hydrogels with Secondary Cross-Linking. *ACS Biomaterials Science & Engineering* 2(10):1743-1751.

121. Itoh M, *et al.* (2015) Scaffold-Free Tubular Tissues Created by a Bio-3D Printer Undergo Remodeling and Endothelialization when Implanted in Rat Aortae. *PLOS ONE* 10(9):e0136681.

122. Iwasaki K, *et al.* (2008) Bioengineered Three-Layered Robust and Elastic Artery Using Hemodynamically-Equivalent Pulsatile Bioreactor. *Circulation* 118(14 suppl 1):S52-S57.

123. Tsai KJ, *et al.* (2017) Biomimetic heterogenous elastic tissue development. *npj Regenerative Medicine* 2(1):16.

124. Carrow JK, Kerativitayanan P, Jaiswal MK, Lokhande G, & Gaharwar AK (2015) Chapter 13 - Polymers for Bioprinting A2 - Atala, Anthony. *Essentials of 3D Biofabrication and Translation*, ed Yoo JJ (Academic Press, Boston), pp 229-248.

125. Peak CW, Stein J, Gold KA, & Gaharwar AK (2017) Nanoengineered Colloidal Inks for 3D Bioprinting. *Langmuir*.

126. Xiaoxiao H, Richard B, & Russell H (2016) Engineering design of artificial vascular junctions for 3D printing. *Biofabrication* 8(2):025018.

127. Shin SR, *et al.* (2013) Carbon-Nanotube-Embedded Hydrogel Sheets for Engineering Cardiac Constructs and Bioactuators. *ACS Nano* 7(3):2369-2380.

128. Izadifar M, Chapman D, Babyn P, Chen X, & Kelly ME (2017) UV-Assisted 3D Bioprinting of Nanoreinforced Hybrid Cardiac Patch for Myocardial Tissue Engineering. *Tissue Engineering Part C: Methods* 24(2):74-88.

129. Paul A, *et al.* (2014) Injectable Graphene Oxide/Hydrogel-Based Angiogenic Gene Delivery System for Vasculogenesis and Cardiac Repair. *ACS Nano* 8(8):8050-8062.

130. Navaei A, *et al.* (2016) Gold nanorod-incorporated gelatin-based conductive hydrogels for engineering cardiac tissue constructs. *Acta Biomaterialia* 41:133-146.

131. Wilson SA, Cross LM, Peak CW, & Gaharwar AK (2017) Shear-Thinning and Thermo-Reversible Nanoengineered Inks for 3D Bioprinting. *ACS Applied Materials & Interfaces* 9(50):43449-43458.

132. Chimene D, Alge DL, & Gaharwar AK (2015) Two-dimensional nanomaterials for biomedical applications: emerging trends and future prospects. *Advanced materials* 27(45):7261-7284.

133. Cross LM, Shah K, Palani S, Peak CW, & Gaharwar AK (2017) Gradient nanocomposite hydrogels for interface tissue engineering. *Nanomedicine: Nanotechnology, Biology and Medicine*.

134. Lokhande G, *et al.* (2018) Nanoengineered injectable hydrogels for wound healing application. *Acta biomaterialia*.

135. Murphy SV & Atala A (2014) 3D bioprinting of tissues and organs. *Nature Biotechnology* 32:773.

136. C. SB, *et al.* (2018) Hemostatic and Absorbent PolyHIPE–Kaolin Composites for 3D Printable Wound Dressing Materials. *Macromolecular Bioscience* 18(5):1700414.

137. A. SN, S. DP, & M. CHE (2016) Emulsion Inks for 3D Printing of High Porosity Materials. *Macromolecular Rapid Communications* 37(16):1369-1374.

138. Ding H & Chang R (2018) Printability Study of Bioprinted Tubular Structures Using Liquid Hydrogel Precursors in a Support Bath. *Applied Sciences* 8(3):403.

139. Jin Y, Chai W, & Huang Y (2017) Printability study of hydrogel solution extrusion in nanoclay yield-stress bath during printing-then-gelation biofabrication. *Materials Science and Engineering: C* 80:313-325.

140. Jin Y, Compaan A, Chai W, & Huang Y (2017) Functional Nanoclay Suspension for Printing-Then-Solidification of Liquid Materials. *ACS Applied Materials & Interfaces* 9(23):20057-20066.

141. Rocca M, Fragasso A, Liu W, Heinrich MA, & Zhang YS (Embedded Multimaterial Extrusion Bioprinting. *SLAS TECHNOLOGY: Translating Life Sciences Innovation* 0(0):2472630317742071.

142. Chimene D, Lennox KK, Kaunas RR, & Gaharwar AK (2016) Advanced Bioinks for 3D Printing: A Materials Science Perspective. *Annals of Biomedical Engineering* 44(6):2090-2102.

143. Jang J, *et al.* (2017) 3D printed complex tissue construct using stem cell-laden decellularized extracellular matrix bioinks for cardiac repair. *Biomaterials* 112:264-274.

144. Weining B, Christopher PJ, & Nenad B (2014) Controlling the structural and functional anisotropy of engineered cardiac tissues. *Biofabrication* 6(2):024109.

145. Wang MO, *et al.* (2015) Evaluating 3D Printed Biomaterials as Scaffolds for Vascularized Bone Tissue Engineering. *Advanced materials (Deerfield Beach, Fla.)* 27(1):138-144.

146. Cooper SL, Peppas NA, Hoffman AS, & Ratner BD (1982) *Biomaterials: Interfacial Phenomena and Applications* (AMERICAN CHEMICAL SOCIETY) p 564.

147. Daniel R, *et al.* (Tissue Engineering at the Blood-Contacting Surface: A Review of Challenges and Strategies in Vascular Graft Development. *Advanced Healthcare Materials* 0(0):1701461.

148. Sandip S, M. SK, George H, & M. SA (2007) Addressing thrombogenicity in vascular graft construction. *Journal of Biomedical Materials Research Part B: Applied Biomaterials* 82B(1):100-108.

149. Hulander M, *et al.* (2013) Gradients in surface nanotopography used to study platelet adhesion and activation. *Colloids and Surfaces B: Biointerfaces* 110:261-269.

150. F. HJ & O. ER (1981) Effects of roughness on the thrombogenicity of a plastic. *Journal of Biomedical Materials Research* 15(1):1-7.

151. Milleret V, Hefti T, Hall H, Vogel V, & Eberli D (2012) Influence of the fiber diameter and surface roughness of electrospun vascular grafts on blood activation. *Acta Biomaterialia* 8(12):4349-4356.

152. Kee MF, Myers DR, Sakurai Y, Lam WA, & Qiu Y (2015) Platelet Mechanosensing of Collagen Matrices. *PLOS ONE* 10(4):e0126624.

153. Qiu Y, *et al.* (2014) Platelet mechanosensing of substrate stiffness during clot formation mediates adhesion, spreading, and activation. *Proceedings of the National Academy of Sciences* 111(40):14430-14435.

154. Qiu Y, Ciciliano J, Myers DR, Tran R, & Lam WA (2015) Platelets and physics: How platelets "feel" and respond to their mechanical microenvironment. *Blood Reviews* 29(6):377-386.

155. Daamen WF, Veerkamp JH, van Hest JCM, & van Kuppevelt TH (2007) Elastin as a biomaterial for tissue engineering. *Biomaterials* 28(30):4378-4398.

156. Kumar VA, *et al.* (2013) Acellular vascular grafts generated from collagen and elastin analogs. *Acta Biomaterialia* 9(9):8067-8074.

157. Anna G, *et al.* (1995) Heparin release from thermosensitive polymer coatings: in vivo studies. *Journal of Biomedical Materials Research* 29(7):811-821.

158. Yali L, G. NK, & T. KE (2005) Controlled release of heparin from polypyrrole-poly(vinyl alcohol) assembly by electrical stimulation. *Journal of Biomedical Materials Research Part A* 73A(2):171-181.

159. Kharaziha M, Memic A, Akbari M, Brafman DA, & Nikkhah M (2016) Nano-Enabled Approaches for Stem Cell-Based Cardiac Tissue Engineering. *Advanced Healthcare Materials* 5(13):1533-1553.

160. Thavandiran N, Nunes SS, Xiao Y, & Radisic M (2013) Topological and electrical control of cardiac differentiation and assembly. *Stem Cell Research & Therapy* 4(1):14.

161. Kolesky DB, *et al.* (2014) 3D Bioprinting of Vascularized, Heterogeneous Cell-Laden Tissue Constructs. *Advanced Materials* 26(19):3124-3130.

162. Wu W, *et al.* (2010) Direct-write assembly of biomimetic microvascular networks for efficient fluid transport. *Soft Matter* 6(4):739-742.

163. Willie W, Adam D, & A. LJ (2011) Omnidirectional Printing of 3D Microvascular Networks. *Advanced Materials* 23(24):H178-H183.

164. Ouyang L, Burdick JA, & Sun W (2018) Facile Biofabrication of Heterogeneous Multilayer Tubular Hydrogels by Fast Diffusion-Induced Gelation. *ACS Applied Materials & Interfaces* 10(15):12424-12430.

165. Holzapfel GA, Sommer G, Gasser CT, & Regitnig P (2005) Determination of layer-specific mechanical properties of human coronary arteries with nonatherosclerotic intimal thickening and related constitutive modeling. *American Journal of Physiology - Heart and Circulatory Physiology* 289(5):H2048-H2058.

166. Armentano RL, *et al.* (1991) Assessment of elastin and collagen contribution to aortic elasticity in conscious dogs. *American Journal of Physiology-Heart and Circulatory Physiology* 260(6):H1870-H1877.

167. Jang S-H, Park Y-L, & Yin H (2016) Influence of Coalescence on the Anisotropic Mechanical and Electrical Properties of Nickel Powder/Polydimethylsiloxane Composites. *Materials* 9(4):239.

168. Palchesko RN, Zhang L, Sun Y, & Feinberg AW (2012) Development of Polydimethylsiloxane Substrates with Tunable Elastic Modulus to Study Cell Mechanobiology in Muscle and Nerve. *PLOS ONE* 7(12):e51499.

169. Carrillo F, *et al.* (2011) Nanoindentation of polydimethylsiloxane elastomers: Effect of crosslinking, work of adhesion, and fluid environment on elastic modulus. *Journal of Materials Research* 20(10):2820-2830.

170. Montini-Ballarin F, *et al.* (2016) Mechanical behavior of bilayered small-diameter nanofibrous structures as biomimetic vascular grafts. *Journal of the Mechanical Behavior of Biomedical Materials* 60:220-233.

171. Carrow JK, *et al.* (2018) Widespread changes in transcriptome profile of human mesenchymal stem cells induced by two-dimensional nanosilicates. *Proceedings of the National Academy of Sciences* 115(17):E3905-E3913.

172. Makris EA, Gomoll AH, Malizos KN, Hu JC, & Athanasiou KA (2014) Repair and tissue engineering techniques for articular cartilage. *Nature Reviews Rheumatology* 11:21.

173. Huh D, *et al.* (2013) Microfabrication of human organs-on-chips. *Nature Protocols* 8:2135.

174. Reardon S (2015) 'Organs-on-chips' go mainstream. *Nature* 523.

175. Jia W, *et al.* (2016) Direct 3D bioprinting of perfusable vascular constructs using a blend bioink. *Biomaterials* 106:58-68.

176. Zhu W, *et al.* (2017) Direct 3D bioprinting of prevascularized tissue constructs with complex microarchitecture. *Biomaterials* 124:106-115.

177. Skylar-Scott MA, *et al.* (2019) Biomanufacturing of organ-specific tissues with high cellular density and embedded vascular channels. *Sci Adv* 5(9):eaaw2459.

178. Cooper GM, *et al.* (2009) Inkjet-Based Biopatterning of Bone Morphogenetic Protein-2 to Spatially Control Calvarial Bone Formation. *Tissue Engineering Part A* 16(5):1749-1759.

179. Fedorovich NE, De Wijn JR, Verbout AJ, Alblas J, & Dhert WJA (2008) Three-Dimensional Fiber Deposition of Cell-Laden, Viable, Patterned Constructs for Bone Tissue Printing. *Tissue Engineering Part A* 14(1):127-133.

180. Derby B (2012) Printing and Prototyping of Tissues and Scaffolds. *Science* 338(6109):921-926.

181. Duan B, Hockaday LA, Kang KH, & Butcher JT (2013) 3D Bioprinting of heterogeneous aortic valve conduits with alginate/gelatin hydrogels. *Journal of Biomedical Materials Research Part A* 101A(5):1255-1264.

182. Moroni L, *et al.* (2018) Biofabrication strategies for 3D in vitro models and regenerative medicine. *Nature Reviews Materials* 3(5):21-37.

183. Hansen F, Mangell P, Sonesson B, & Länne T (1995) Diameter and compliance in the human common carotid artery — variations with age and sex. *Ultrasound in Medicine & Biology* 21(1):1-9.

184. Konig G, *et al.* (2009) Mechanical properties of completely autologous human tissue engineered blood vessels compared to human saphenous vein and mammary artery. *Biomaterials* 30(8):1542-1550.

185. Schöneberg J, *et al.* (2018) Engineering biofunctional in vitro vessel models using a multilayer bioprinting technique. *Scientific Reports* 8(1):10430.

186. Gaharwar AK, *et al.* (2014) Shear-Thinning Nanocomposite Hydrogels for the Treatment of Hemorrhage. *ACS Nano* 8(10):9833-9842.

187. Escudier MP, Gouldson IW, & Jones DM (1995) Flow of Shear-Thinning Fluids in a Concentric Annulus. *Experiments in Fluids* 18(4):225-238.

188. Pilavtepe M, Recktenwald SM, Schuhmann R, Emmerich K, & Willenbacher N (2018) Macro- and microscale structure formation and aging in different arrested states of Laponite dispersions. *Journal of Rheology* 62(2):593-605.

189. Sears NA, *et al.* (2019) Hydrocolloid Inks for 3D Printing of Porous Hydrogels. *Adv Mater Technol-Us* 4(2):1800343.

190. Mourchid A, Delville A, Lambard J, Lecolier E, & Levitz P (1995) Phase-Diagram of Colloidal Dispersions of Anisotropic Charged-Particles - Equilibrium Properties, Structure, and Rheology of Laponite Suspensions. *Langmuir* 11(6):1942-1950.

191. Ruzicka B & Zaccarelli E (2011) A fresh look at the Laponite phase diagram. *Soft Matter* 7(4):1268.

192. Thompson DW & Butterworth JT (1992) The Nature of Laponite and Its Aqueous Dispersions. *J Colloid Interf Sci* 151(1):236-243.

193. Mongondry P, Tassin JF, & Nicolai T (2005) Revised state diagram of Laponite dispersions. *J Colloid Interface Sci* 283(2):397-405.

194. Wang Q, *et al.* (2010) High-water-content mouldable hydrogels by mixing clay and a dendritic molecular binder. *Nature* 463(7279):339-343.

195. Anonymous (2014) Laponite Performance Additives. in *Technical Information B-RI 21* (BYK Additives & Instruments, Germany).

196. Ruzicka B, Zulian L, & Ruocco G (2007) Ageing dynamics in Laponite dispersions at various salt concentrations. *Philos Mag* 87(3-5):449-458.

197. Pawar N & Bohidar HB (2009) Surface selective binding of nanoclay particles to polyampholyte protein chains. *J Chem Phys* 131(4):045103.

198. Gaharwar AK, *et al.* (2012) Physically crosslinked nanocomposites from silicate-crosslinked PEO: mechanical properties and osteogenic differentiation of human mesenchymal stem cells. *Macromol Biosci* 12(6):779-793.

199. Suman K & Joshi YM (2018) Microstructure and Soft Glassy Dynamics of an Aqueous Laponite Dispersion. *Langmuir* 34(44):13079-13103.

200. Mourchid A, Delville A, & Levitz P (1995) Sol–gel transition of colloidal suspensions of anisotropic particles of laponite. *Faraday Discuss.* 101:275-285.

201. Nelson A & Cosgrove T (2004) Dynamic light scattering studies of poly(ethylene oxide) adsorbed on Laponite: layer conformation and its effect on particle stability. *Langmuir* 20(24):10382-10388.

202. Lorthioir C, Khalil M, Wintgens V, & Amiel C (2012) Segmental motions of poly(ethylene glycol) chains adsorbed on Laponite platelets in clay-based hydrogels: a NMR investigation. *Langmuir* 28(20):7859-7871.

203. Peak CW, Stein J, Gold KA, & Gaharwar AK (2018) Nanoengineered Colloidal Inks for 3D Bioprinting. *Langmuir* 34(3):917-925.

204. Browning MB, Cereceres SN, Luong PT, & Cosgriff-Hernandez EM (2014) Determination of the in vivo degradation mechanism of PEGDA hydrogels.n/a-n/a.

205. Holback H, Yeo Y, & Park K (2011) 1 - Hydrogel swelling behavior and its biomedical applications. *Biomedical Hydrogels*, ed Rimmer S (Woodhead Publishing), pp 3-24.

206. Kurokawa A, Vidal V, Kurita K, Divoux T, & Manneville S (2015) Avalanche-like fluidization of a non-Brownian particle gel. 11(46):9026-9037.

207. Dijkstra M, Hansen JP, & Madden PA (1995) Gelation of a Clay Colloid Suspension. 75(11):2236-2239.

208. Ye GJC, Nesmith AP, & Parker KK (2014) The role of mechanotransduction on vascular smooth muscle myocytes cytoskeleton and contractile function. *Anatomical record (Hoboken, N.J. : 2007)* 297(9):1758-1769.

209. Mitchell GF (2008) Effects of central arterial aging on the structure and function of the peripheral vasculature: implications for end-organ damage. *Journal of Applied Physiology* 105(5):1652-1660.

210. McFarlane NL, Wagner NJ, Kaler EW, & Lynch ML (2010) Poly(ethylene oxide) (PEO) and Poly(vinyl pyrolidone) (PVP) Induce Different Changes in the Colloid Stability of Nanoparticles. *Langmuir* 26(17):13823-13830.

211. Schmidt G, Nakatani AI, Butler PD, & Han CC (2002) Small-Angle Neutron Scattering from Viscoelastic Polymer−Clay Solutions. *Macromolecules* 35(12):4725-4732.

212. Schmidt G, Nakatani AI, & Han CC (2002) Rheology and flow-birefringence from viscoelastic polymer-clay solutions. *Rheologica Acta* 41(1-2):45-54.

213. Gibaud T, Barentin C, Taberlet N, & Manneville S (2009) Shear-induced fragmentation of laponite suspensions. *Soft Matter* 5(16):3026-3037.

214. Marquardt LM & Heilshorn SC (2016) Design of Injectable Materials to Improve Stem Cell Transplantation. *Curr Stem Cell Rep* 2(3):207-220.

215. Howell DW, Peak CW, Bayless KJ, & Gaharwar AK (2018) 2D Nanosilicates Loaded with Proangiogenic Factors Stimulate Endothelial Sprouting. *Adv Biosyst* 2(7):1800092.

216. Sears NA, Dhavalikar PS, & Cosgriff-Hernandez EM (2016) Emulsion Inks for 3D Printing of High Porosity Materials. 37(16):1369-1374.

217. Kyle S, Jessop ZM, Al-Sabah A, & Whitaker IS (2017) ‘Printability' of Candidate Biomaterials for Extrusion Based 3D Printing: State-of-the-Art. 6(16):1700264.

218. Jelev L & Surchev L (2008) A novel simple technique for en face endothelial observations using water-soluble media -'thinned-wall' preparations. *J Anat* 212(2):192-197.

219. Ko KA, Fujiwara K, Krishnan S, & Abe JI (2017) En Face Preparation of Mouse Blood Vessels. *J Vis Exp* (123):e55460.

220. Jain A, *et al.* (2016) Assessment of whole blood thrombosis in a microfluidic device lined by fixed human endothelium. *Biomed Microdevices* 18(4):73.

221. Mathur T, *et al.* (2019) Organ-on-chips made of blood: endothelial progenitor cells from blood reconstitute vascular thromboinflammation in vessel-chips. *Lab on a Chip* 19(15):2500-2511.

222. Wang YH, *et al.* (2009) Vascular smooth muscle cells promote endothelial cell adhesion via microtubule dynamics and activation of paxillin and the extracellular signal-regulated kinase (ERK) pathway in a co-culture system. *Eur J Cell Biol* 88(11):701-709.

223. Xu S, He Y, Vokurkova M, & Touyz RM (2009) Endothelial cells negatively modulate reactive oxygen species generation in vascular smooth muscle cells: role of thioredoxin. *Hypertension* 54(2):427-433.

224. Wallace CS, Strike SA, & Truskey GA (2007) Smooth muscle cell rigidity and extracellular matrix organization influence endothelial cell spreading and adhesion formation in coculture. *Am J Physiol Heart Circ Physiol* 293(3):H1978-1986.

225. Imberti B, Seliktar D, Nerem RM, & Remuzzi A (2002) The response of endothelial cells to fluid shear stress using a co-culture model of the arterial wall. *Endothelium* 9(1):11-23.

226. Balcells M, *et al.* (2010) Smooth muscle cells orchestrate the endothelial cell response to flow and injury. *Circulation* 121(20):2192-2199.

227. Wallace CS & Truskey GA (2010) Direct-contact co-culture between smooth muscle and endothelial cells inhibits TNF-alpha-mediated endothelial cell activation. *Am J Physiol Heart Circ Physiol* 299(2):H338-346.

228. Dulak J, *et al.* (2000) Nitric Oxide Induces the Synthesis of Vascular Endothelial Growth Factor by Rat Vascular Smooth Muscle Cells. *Arteriosclerosis, Thrombosis, and Vascular Biology* 20(3):659-666.

229. Fordyce CB, *et al.* (2015) Cardiovascular Drug Development. 65(15):1567-1582.

230. Vanderburgh J, Sterling JA, & Guelcher SA (2017) 3D Printing of Tissue Engineered Constructs for In Vitro Modeling of Disease Progression and Drug Screening. *Annals of Biomedical Engineering* 45(1):164-179.

231. Elomaa L & Yang YP (2016) Additive manufacturing of vascular grafts and vascularized tissue constructs.

232. Browning MB, *et al.* (2012) Multilayer vascular grafts based on collagen-mimetic proteins. 8(3):1010-1021.

233. Mitchell SL & Niklason LE (2003) Requirements for growing tissue-engineered vascular grafts. 12(2):59-64.

234. Nakayama Y, Furukoshi M, Terazawa T, & Iwai R (2018) Development of long in vivo tissue-engineered “Biotube” vascular grafts. *Biomaterials* 185:232-239.

235. Wang R, *et al.* (2019) Freestanding hierarchical vascular structures engineered from ice. *Biomaterials* 192:334-345.

236. Groll J, *et al.* (2018) A definition of bioinks and their distinction from biomaterial inks. *Biofabrication* 11(1):013001.

APPENDIX A

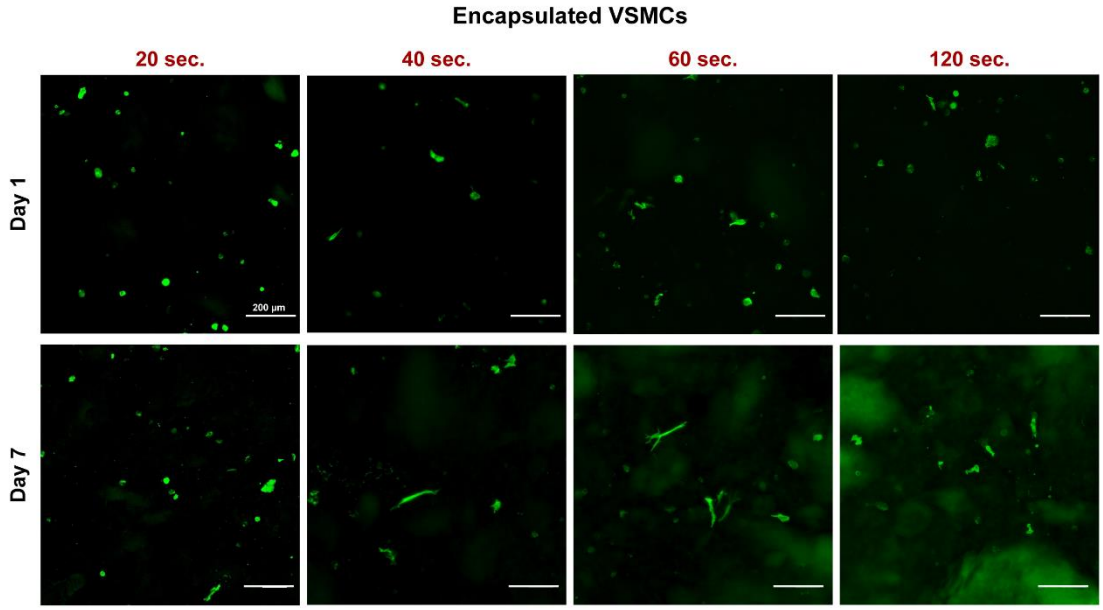

Figure A- 1 UV duration for encapsulated VSMCs. VSMCs were encapsulated in the nECM bioink (7.5 wt.% GelMA, 2.5 wt.% PEGDA, and 4 wt.% nSi) and exposed to UV light (7 mW/cm^2) for varied times (20, 40, 60 and 120 sec.). At Day 1 and Day 7, cells were stained for F-Actin to illustrate cellular spreading. For all experiments, a time of 60 sec. was utilized to obtain a homogenously crosslinked hydrogel that was able to elucidate cellular spreading after 7 days.

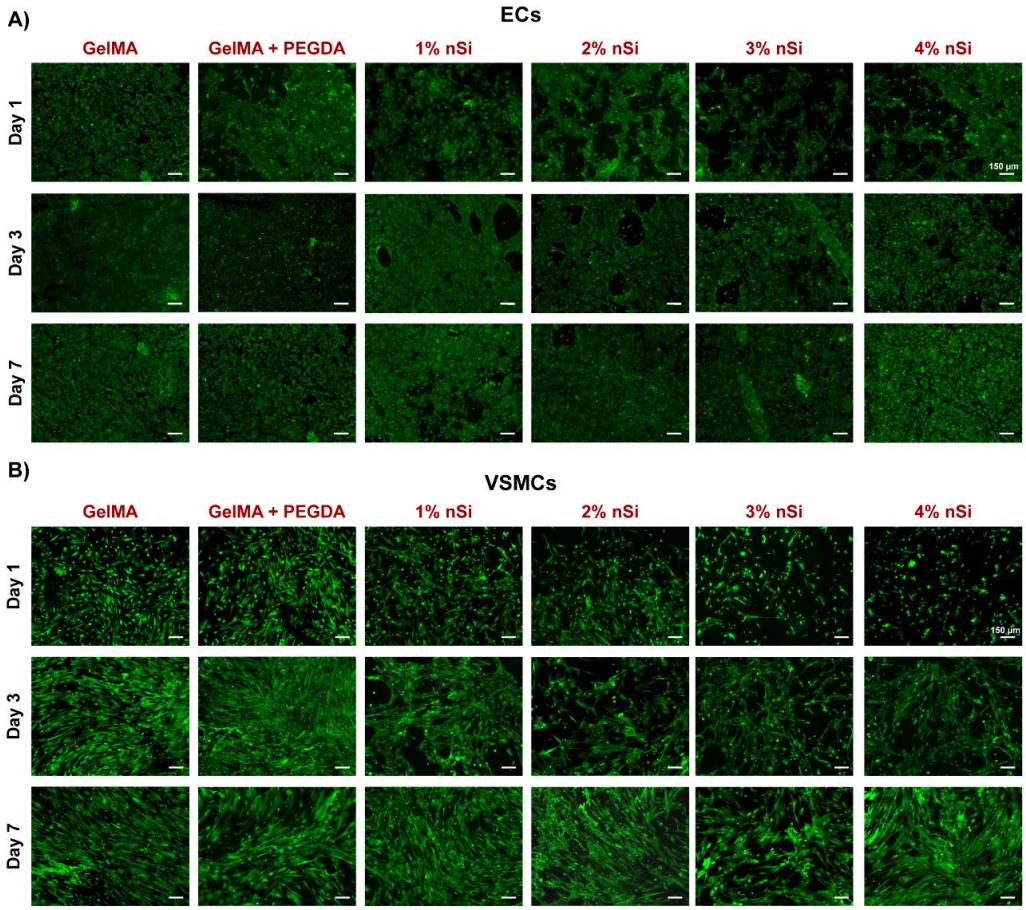

Figure A- 2 Live/Dead Bioink Constituents. Live/Dead assays were conducted on GelMA, GelMA + PEGDA, and GelMA + PEGDA with 1, 2, 3, or 4 wt.% nanosilicates to illustrate the viability of A) ECs and B) VSMCs. For all ECs and VSMCs, a high cell viability (>80 %) was demonstrated across all time points. In addition, an increase in viable cells was illustrated from days 1, 3, and 7, correlating to cellular proliferation.

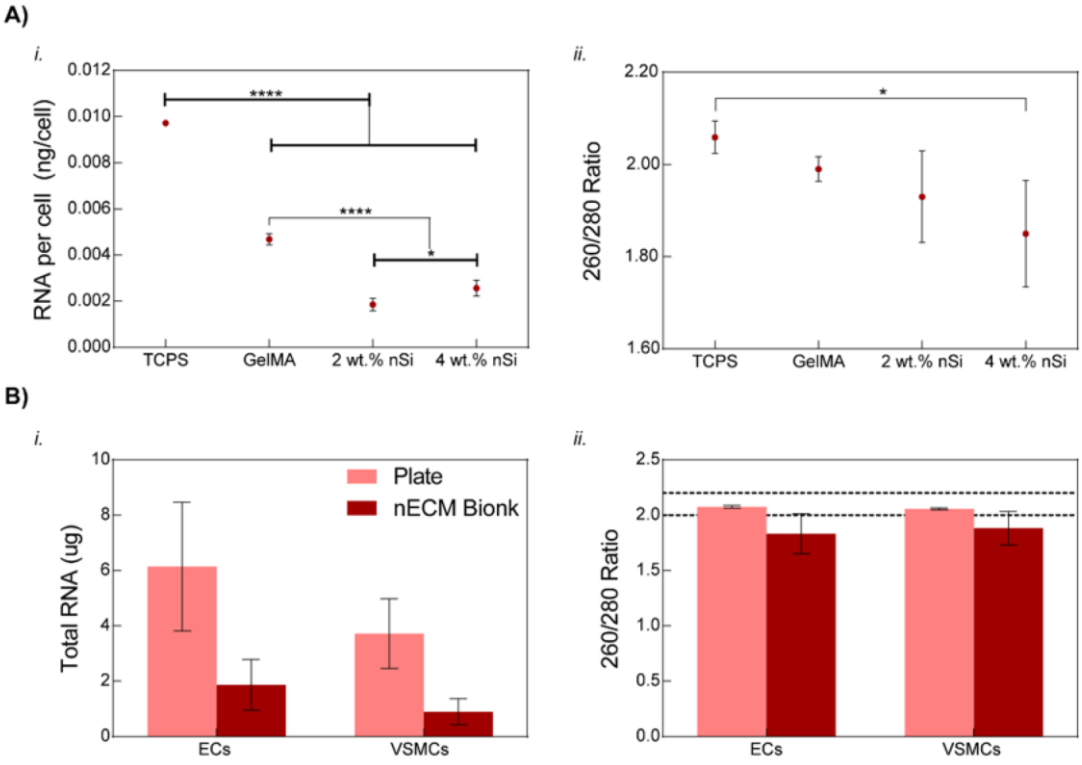

Figure A- 3 RNA Extraction. A) RNA was extracted from seeded ECs after 3 days. *i.* Prior to RNA extraction, the number of cells were determined and the amount of RNA (ng) per cell determined. When seeding on a hydrogel, there is a significant reduction in RNA collected per cell compared to TCPS controls. In addition, upon the addition of nSi, a significant reduction of RNA collected per cell is observed as the concentration of nanosilicate is increased as well as when compared to GelMA controls. *ii.* RNA purity was assessed by investigating the 260:280 ratio. Upon the addition of nSi, a larger standard deviation was observed as well as a reduction in RNA purity as the concentration of nanosilicate was increased. B) *i.* Total amount of RNA collected (µg) for PCR experiments conducted. TCPS controls, or plate, presented a significant increase in total amount of RNA collected compared to RNA extracted from nECM bioink. *ii.* RNA-purity for samples extracted for PCR did not demonstrate a significant different in between TCPS or plate controls and nECM bioink.

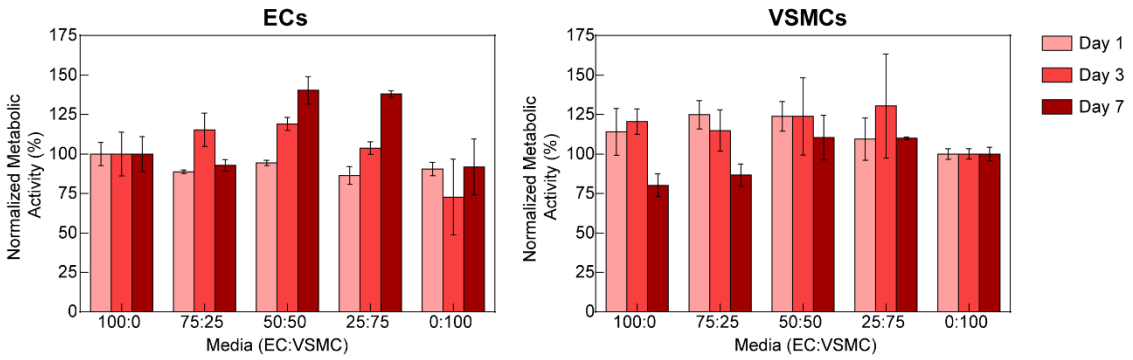

Figure A- 4 Determining EC-VSMC Media Ratios. The normalized metabolic activity of EC and VSCMs on days 1, 3, and 7 when cultured on TCPS under various ratios of EC and VSMC medium (100:0, 75:25, 50:50, 25:75, 0:100 EC:VSMC media For all co-culture conducted, a ratio of 50:50 EC:SMC media was used due to preservation of VSMC metabolic activity across all time points assessed in addition to an increase in metabolic activity over time for ECs.